

UNIVERSITÄT WIEN

# Molecular Lithography - A Quantum Optical Approach

Diplomarbeit  
zur Erlangung des akademischen Grades  
*Magister rerum naturalium*

verfasst von

**Stefan Truppe**

Unter Anleitung von  
**Prof. Dr. Markus Arndt**

Fakultät für Physik

Juni 2009

*Nothing exists except atoms and empty space. Everything else is opinion*

Democritus

# Abstract

Quantum mechanics is the most precise theory ever developed and acts as a driving force for technological progress and wealth. It transcends established philosophical concepts of reality and functions as a rich source for revolutionary scientific research. And yet it remains counter intuitive.

In particular, the wave particle duality is a cornerstone of quantum physics and lies in the heart of our modern physical world view. It has remained subject of fiery debates until present times. A suitable tool that demonstrates the fundamental concepts of the wave nature of massive particles in a beautiful way can be seen in matter-wave interferometry. This concept has now been significantly extended by combining the field of molecular quantum optics with nanotechnological methods. Namely, the imprinting of nanometer-scale interference patterns onto silicon surfaces. The use of a scanning tunneling microscope to evaluate the recorded interference with single atom resolution, elucidates the quantum wave-nature of massive particles in its most distinct form.

Large and internally complex carbon fullerenes leave the source as single, localized particles and are revealed as individual molecules deposited on a surface, but structured in a way that they have to be described by a delocalized quantum wave during their propagation through an interferometer. Apart from this fundamental approach, the use of quantum interference to deposit nanostructures composed of single, complex molecules onto silicon surfaces offers unique possibilities for novel technological applications. Thus, we trespass the mere demonstration of fundamental quantum effects to approach a novel technological application of matter-wave interferometry.

Innovative improvements regarding the existing vacuum apparatus and alignment of the interferometer, coupled with crucial knowledge gained concerning the imaging with atomic resolution and exceptional, novel inventions dealing with the velocity selection of a molecular beam and accurate tip positioning, make it possible to present the first image of a quantum interferogram of large molecules directly visualized with single atom resolution.

# Kurzfassung

Die Quantenmechanik kann als das präziseste physikalische Modell angesehen werden, das je entwickelt wurde. Sie fungiert als Triebkraft für technologischen Fortschritt und Wohlstand. Sie überschreitet etablierte philosophische Konzepte der Realität und dient als reiche Quelle für revolutionäres, wissenschaftliches Denken. Und trotzdem ist sie mit unseren klassischen Vorstellungen nicht vereinbar.

Der Welle-Teilchen Dualismus im Besonderen ist ein Meilenstein der Quantenphysik und nimmt einen zentralen Platz in unserem modernen physikalischen Weltbild ein. Seit jeher ist er Gegenstand hitziger Debatten. Materiewellen-Interferometrie stellt sich als geeignetes Werkzeug heraus, die fundamentalen Konzepte der Wellennatur von massiven Teilchen elegant darzustellen. Diese Methode wurde nun entscheidend durch die Kombination der molekularen Quantenoptik mit nanotechnologischen Verfahren erweitert: Das molekulare Interferenzmuster wird lithographisch auf eine Siliziumoberfläche geprägt. Die Verwendung eines Rastertunnelmikroskops ermöglicht hierdurch die Auswertung der aufgenommenen Interferenz mit atomarer Auflösung. Die quantenphysikalische Wellennatur massiver Teilchen erscheint so in einem völlig neuen Licht.

Während des Experiments verlassen große Kohlenstoff-Fullerene mit komplexer innerer Struktur als einzelne, lokalisierte Teilchen die Quelle und werden als solche auch auf der Oberfläche deponiert. Doch ihre Anordnung lässt auf ein Verhalten während des Durchgangs im Interferometer schließen, das als quantenphysikalische, räumlich ausgedehnte Welle interpretiert wird. Zusätzlich zur Demonstration dieser fundamentalen Quanteneffekte eröffnen sich einzigartige Möglichkeiten für neue technologische Anwendungen der Materiewellen-Interferometrie.

Innovative Verbesserungen in Bezug auf den bestehenden Vakuumapparat und die Justage des Interferometers haben genauso zu einem erfolgreichen Experiment beigetragen, wie das wertvolle Wissen und die Erfahrungen, die durch die Arbeit mit einem Rastertunnelmikroskop gesammelt werden konnten. Darüber hinaus wurden neuartige Methoden zur Geschwindigkeitsselektion eines molekularen Strahles und zur Positionierung der Tunnelspitze entwickelt. So wird in dieser Arbeit erstmalig ein topographisches Abbild molekularer Interferenz mit atomarer Auflösung präsentiert.

# Contents

<b>Abstract</b>	<b>ii</b>
<b>Kurzfassung</b>	<b>iii</b>
<b>1 Introduction &amp; Motivation</b>	<b>1</b>
1.1 The Nature of Light and Matter - A Scientific Dispute . . . . .	1
1.2 Double Slit Experiment - The Most Beautiful Experiment in Physics . .	7
<b>2 Theoretical Overview</b>	<b>10</b>
2.1 The Talbot-Lau Interferometer - An Introduction . . . . .	10
2.2 Phase Space Dynamics - The Wigner Function . . . . .	12
2.3 Description of the Interferometer . . . . .	15
2.3.1 Fourier Decomposition of the Diffraction Gratings . . . . .	16
2.4 Decoherence . . . . .	21
<b>3 On the Road to Quantum Interference - The Experimental Realization</b>	<b>23</b>
3.1 Overview of the Experimental Setup . . . . .	23
3.1.1 Decoherence . . . . .	24
3.1.2 Contamination of the Sample Surface . . . . .	24
3.1.3 The Experimental Setup . . . . .	26
3.1.4 The Bake-out Procedure . . . . .	30
3.2 Molecular Beam Source . . . . .	31
3.2.1 The Molecules - Carbon Fullerenes . . . . .	31
3.2.2 Properties of the Beam Source . . . . .	32
3.2.3 The Longitudinal Velocity Distribution of the Thermal Beam . . .	34
3.3 Velocity Selection . . . . .	35
3.3.1 Gravitational Velocity Selection . . . . .	35
3.3.2 Velocity Selection by a Rotating Helix . . . . .	37
3.3.3 A High Resolution, Sideband-Free Slotted Disk Velocity Selector .	40
3.3.4 In-Vacuum Movement . . . . .	44
3.3.5 Comparing the Different Velocity Selection Schemes - A Summary	46
3.4 The Interferometer . . . . .	47
3.4.1 The Adjustment Requirements . . . . .	47
3.4.2 Yaw, Pitch of the Gratings . . . . .	49

3.4.3	Roll	50
3.4.4	The Alignment Procedure	51
3.5	The Detection Scheme	54
3.6	The Detection Surface	54
3.7	Scanning Tunneling Microscopy - STM	55
3.7.1	The Basic Principle	56
3.7.2	Tip Preparation	57
3.8	The Experimental Procedure - A Chronology	59
3.8.1	Sample Preparation	60
3.8.2	Source Preparation	61
3.8.3	Scanning the Sample Surface	62
3.8.4	Alignment of the Source and the Velocity Selector	64
3.8.5	The Experiment	66
3.9	Evaluation	69
3.9.1	Gravitational Selection	69
3.9.1.1	Determination of the Sample Coverage as a Function of the Falling Height	72
3.9.1.2	Scanning for Interference Contrast	73
3.9.2	Helical Velocity Selection	74
<b>4</b>	<b>Image Evaluation &amp; Discussion</b>	<b>76</b>
4.1	Image Evaluation	76
4.2	Discussion	78
<b>5</b>	<b>Conclusion &amp; Perspectives</b>	<b>80</b>
5.1	Conclusion	80
5.2	Perspectives	80
<b>A</b>	<b>Helical Velocity Selector</b>	<b>83</b>
<b>B</b>	<b>Slotted Disk Velocity Selector</b>	<b>87</b>
<b>C</b>	<b>Interferometer</b>	<b>91</b>
	<b>Acknowledgements</b>	<b>95</b>
	<b>Bibliography</b>	<b>96</b>
	<b>Curriculum Vitae</b>	<b>104</b>

# Preface

A concise description of the historical debate about the nature of light and matter marks the beginning of this manuscript. This facilitates the classification of the presented experiment as an extending link in the long tradition associated with the wave-particle duality and its consequences for modern physics and beyond. Furthermore, the introduction guides the reader through the vivid discussion of the early stages of quantum mechanics emphasizing the troublesome process of introducing new concepts to an apparently complete physical picture of reality. The historical remarks may further serve as an appealing motivation, highlighting the necessity for fundamental research as a major incentive for intellectual progress.

This is succeeded by a brief introduction to the double slit experiment as the father of all quantum *weirdness*. Except entanglement it contains all the mysteries arising from quantum theory and it thus provides the reader with the necessary foundation for assessing the importance of the presented work.

For the sake of completeness a brief sketch of the theoretical framework is presented. By focusing on the main concepts rather than on an explicit calculation which is done elsewhere, the reader gains access to the specific theoretical methodology that is necessary for the calculation of the expected results. This conveys a complete picture and allows extensive discussion.

Since the vacuum conditions have a strong influence on the design of the vacuum apparatus a short excursus about the pressure requirements stands at the beginning of the experimental section. A general overview of the vacuum setup, illustrated with schematic drawings succeeds and is completed by a detailed description of the particular parts. Throughout the manuscript it is well distinguished between the theoretical preconditions and the concrete experimental method used to achieve these requirements. Finally, a chronology of the experimental procedure serves as a guiding framework for presenting particular experimental details and results.

This is followed by the description of the evaluation process. The results are discussed and contrasted with the theoretical predictions.

A conclusion summarizes the achievements and provides the foundation for an outlook in which possible improvements for the near future and far reaching perspectives are discussed.

# Chapter 1

## Introduction & Motivation

### 1.1 The Nature of Light and Matter - A Scientific Dispute

Ever since mankind has been reasoning, the longing for elucidating the nature of light and matter has been a considerable part of philosophical and scientific debate. It begins with the atomistic theory of Leucippus and his student Democritus, who coined the term *atom*, reaching Plato, Aristotle, Lucretius and Seneca, whose understanding and intention of categorizing nature's phenomena into fundamental principles can be seen as the birth of a primitive scientific method.

Aristotle even affected the methodical access to nature until the breaking point of modern times with Galileo Galilei, who invented the experiment as an artificial reality to extract natural laws. The almost superhuman act of translating the prevailing difference *Truth - Hypothesis* to the dialectic notion *Truth - Knowledge* marks the beginning of modern natural science [1]. Thus, for a period as long as 1800 years the image, that everything, even light, consists of tiny bits of matter had been considered as an indefeasible truth, just as Aristotle himself.

Robert Grosseteste, an English bishop, who lived in the 12<sup>th</sup> century, speculated for the first time about the affinity of light and waves. A new concept was born, which was then elaborated by Galileo. He introduced the frequency term, which was connected to light by Descartes. But the first to describe light as a consequence of vibrations was Malebranche. At the same time Huygens established the first complete theory based

on a wave theory of light, which not only explained numerous experimental results, but furthermore confirmed Fermat's principle, that light always travels the path of extremal time. However, in a time where authority prevailed over critical reasoning, Newton's concept of light particles was the one of choice. It took until the beginning of the 19<sup>th</sup> century that the new wave description became widely accepted, ignited by the discovery of the interference principle by Thomas Young and its interpretation by Fresnel, who made use of Huygen's principle.

Simultaneously, the new field of electrodynamics emerged, due to the work done by Ampère. He drew back on an experiment of the Danish chemist Ørstedt who investigated the influence of a current, passing through a wire, on a compass needle. This served as a fundament on which Faraday could build up his abstract field concept, which plays a central role in classical and modern physics. Equipped with such powerful tools not much time passed before Maxwell could derive his beautiful electromagnetic theory, which marked the second great unification in physics, after the first carried out by Newton. Even after the revolutionary prediction of electromagnetic waves had been verified by Hertz, the new concept still encountered opposition within the physical community.

Concurrently, John Dalton, an English chemist, came up with the purely physical concept of atoms with a definite and characteristic weight, in order to explain the physical properties of the atmosphere and other gases. Physicists immediately realized the relevance of this idea and thermodynamics was born. Even if the atoms were accepted as useful means to describe things, a large fraction of physicists, especially the positivists around Ernst Mach, simply denied their physical reality.

But the discovery of the x-rays by Röntgen, radioactivity by Henri Becquerel and the experimental proof of the existence of the electron by J.J. Thomson were inevitable evidences, that atoms represent more than just purely imagined objects. Soon the first models about the internal structure of the now divisible atom appeared. The preliminary peak of this development was reached by Nils Bohr, who rested his revolutionary idea of stable, discrete electron orbits on the work of Ernest Rutherford and his experiment using alpha particles scattered at thin gold films.

On the one hand, the ancient idea of atoms as classical point particles staged a successful comeback on the scene of modern physics. On the other hand, Maxwell's prosperous electrodynamic theory of fields and waves was very well established and widely recognized. Initially very separate terrains within physics, the discrete atomistic theory and the continuous fields of Maxwell were firstly brought together by Hendrik A. Lorentz.

He thought for the first time that atoms could consist of charged particles and that this charged particles may serve as the source for electromagnetic waves. Furthermore, he ascribed every electric and magnetic phenomenon a behavior of charged particles. The questions about the electrodynamic of moving objects and how radiation is emitted and absorbed arose from Lorentz's discovery. The first question lead to special relativity and the second to the invention of the quantum. We can further regard this as the turning point in modern physics, where the answers to two, at this time apparently ineffectual and subsidiary questions revolutionized the theoretical framework of centuries and shook our perception of reality to the very foundations.

It was exactly at this definitive point the ingenious impartiality of Albert Einstein helped to pave the way for a new age in the physical understanding of nature. In contrast to Planck, who regarded the assumption of discrete energy levels of the oscillators of a black body as a purely formal one, Einstein was fully aware of the consequences that his idea of quantizing the electromagnetic field itself would have. After some time conservative minded Planck realized that it is not possible to integrate his natural constant into the classical framework, and was willing to find compromises, due to his belief in fact based logical thinking, even if it was contradicting tradition. However, the application of his concept to the electromagnetic field itself, as Einstein proposed in 1905 [2], discarding Maxwell's great theory, in order to explain the photoelectric effect, was unacceptable for Planck. It took six years, until the Solvay conference<sup>1</sup> in Brussels, that Einstein could convince Planck of his new idea.

Maxwell's theory deals with temporal averages and continuous spacial variables, in order to explain the electromagnetic state of space. Whereas Planck invented the quantization of oscillations in an *act of despair* [3], Einstein discretised the field itself and recognized, that it was necessary to find a symbiotic theory that connects the two antagonistic concepts to explain the processes of light absorption and emission coherently. He layed the foundation to such a theory with his hypothesis that the energy of light is discontinuously distributed in space. In his opinion the light quanta are similar to static electric charges, singularities, which are accompanied by a surrounding forcefield [2], wavelike in nature, whose amplitude declines with increasing distance to the singularity.

Thus, Einstein was wise enough to see that each theory has its area of validity. He immediately called for a new theory which would be capable of bringing together the two competing concepts of light, that he considered to be complementary. It took as

---

<sup>1</sup>The first conference organized by the International Solvay Institutes for Physics and Chemistry in Brussels was held in 1911 on the subject: *Radiation and the Quanta*

long as sixteen years and numerous articles of beautiful argumentation, for his pioneering idea to be accepted and finally be awarded the Nobel Prize. The next years, until the mid twenties of the last century, were characterized by the discussion of the new theory of radiation and quanta. It was duke Louis de Broglie, who heralded a new age in the understanding of the nature of matter. De Broglie took the two newly derived equations for Energy, namely Planck's relation  $E = h\nu$  and Einstein's famous equality of mass and energy  $E = mc^2$ , which had been regarded as parts of completely different concepts without any connection and sets an equal sign in between them [4]. Resulting in the expression

$$m_0c^2 = h\nu_0 \quad (1.1)$$

Where  $\nu_0$  has to be measured in the rest frame of the energy packet. Thus it can be inferred that a certain periodic phenomenon with a definite frequency can be assigned to a given mass. But de Broglie recognized immediately that he ran into a contradiction. This is due to the fact that an observer resting with respect to a moving object detects a slightly larger energy, strictly speaking, about the factor

$$\gamma = \frac{1}{\sqrt{1 - \beta^2}} \quad \text{with} \quad \beta = \frac{v}{c} \quad (1.2)$$

larger. This corresponds to a frequency of

$$\nu_1 = \frac{1}{h} \frac{m_0c^2}{\gamma} \quad (1.3)$$

On the contrary, the internal clock of the moving system is subjected to time dilatation by the factor  $1/\gamma$  with respect to the resting observer, corresponding to a frequency

$$\nu = \frac{1}{h} m_0 \gamma c^2 \quad (1.4)$$

The different dependence of  $\nu_1$  and  $\nu$  on the factor  $\gamma$ , de Broglie solved with the theorem of *phase harmony*, which he always regarded as his major achievement [5]. From this point of view the postulated periodic phenomenon with frequency  $\nu_1$  is seen to be in phase with a wave of frequency  $\nu$  propagating in the same direction with velocity  $V = \frac{c}{\beta}$ , which is larger than the speed of light and thus cannot transport energy or information.

Furthermore it can be seen that the group velocity

$$U = \frac{d\nu/d\beta}{d(\nu/V)/d\beta} \quad (1.5)$$

where

$$\frac{d\nu}{d\beta} = \frac{m_0 c^2}{h} \frac{\beta}{(1 - \beta^2)^{3/2}} \quad (1.6)$$

$$\frac{d(\nu/V)}{d\beta} = \frac{m_0 c^2}{h} \frac{1}{(1 - \beta^2)^{3/2}} \quad (1.7)$$

so that

$$U = \beta c = v \quad (1.8)$$

equals the velocity  $v$  of its associated body. The newly invented concept of matter-waves serves as a marking point for a new perception of nature - the connection between the two contrasting representations of matter, with definite mass, located at a particular location and waves distributed over space with the ability to exhibit periodic phenomena. Being able to explain diffraction, interference, the stability of the electron orbits in an atom and the equilibrium of a gas in a box, de Broglie immediately demonstrated the power of this new description. Within his considerations of statistical mechanics de Broglie also introduced the famous expression

$$\lambda = \frac{h}{p} \quad (1.9)$$

for the first time where an explicit wavelength  $\lambda$  is associated with any massive particle. De Broglie's deep conviction to a reality independent from the observer and to precise images in time and space as a representative frame for physical phenomena, may be a reason why the idea of phase-waves should remain his only great contribution to the development of modern physics. A new generation of more formal thinking physicists, like Werner Heisenberg, Max Born and Pascal Jordan succeeded a new mathematical approach, in order to describe this new aspects in a general and coherent way.

By introducing matrix equations Heisenberg layed the foundation for mechanics at an atomic scale - *quantum mechanics* was born. In 1926, Erwin Schrödinger wrote a series of articles [6–10] about the quantization, described as an eigenwertproblem, which resulted in a complete undulatory theory of the mechanics of atoms and molecules. It was mainly the abstractness of the idea of phase waves, which puzzled contemporaries of de

Broglie and which could be an explanation for the fact, that only a few, including Einstein and Schrödinger, recognized the importance of de Broglie's discovery. Schrödinger tried a straight-forward approach, by deriving a wave equation for matter-waves from Hamilton's principle of least action and even deriving Planck's universal relation and de Broglie's wavelength *in a rather simple and unforced way* [6]. By defining a wave function  $\psi$ , that fulfills a classical, non relativistic wave equation, Schrödinger invented a powerful tool, that continues its triumphal procession until present times. It was the great idea of Schrödinger, that quantization can be naturally derived by describing it as an eigenwertproblem:

$$\left[ -\frac{\hbar^2}{2m} \Delta + V(\vec{r}) \right] \Psi(\vec{r}, t) = i\hbar \frac{\partial \Psi(\vec{r}, t)}{\partial t} \quad (1.10)$$

Once a wave equation for matter-waves has been established, the whole toolbox of classical optics can be applied to investigate their properties. Finding new applications and effects by making use of the concepts arising from quantum mechanics on the one hand, and exploring a completely new viewpoint on nature and philosophy on the other hand, determines the further development of this new theory.

By solving the time dependent Schrödinger equation 1.10 with a separation ansatz for time independent potentials  $V(\vec{r})$

$$\Psi(\vec{r}, t) = \phi(\vec{r}) e^{i\omega t} \quad (1.11)$$

equation 1.10 translates to the time independent Schrödinger equation, which is formally equivalent to the fundamental equation of optics named after Hermann von Helmholtz.

$$\left[ \Delta + \frac{2m}{\hbar^2} (E - V(\vec{r})) \right] \phi(\vec{r}) = 0 \quad \leftrightarrow \quad (\Delta + k^2) \phi(\vec{r}) = 0 \quad (1.12)$$

where  $k = \frac{2m}{\hbar^2} (E - V(\vec{r}))$  represents the wave number  $k = 2\pi/\lambda$  with the general harmonic, plane wave solution

$$\Psi(\vec{r}, t) = A e^{i(\vec{k}\vec{r} - \omega t)} \quad (1.13)$$

Arriving now at the fundamental equation 1.12 of electrodynamics the power of this new formalism becomes even more lucid. Without regarding the physical interpretation of de Broglie's phase waves at this point, one can think of a purely formal definition of a refractive index, diffraction, interference, lenses and mirrors for matter waves. Moreover, the tiny wavelength associated with high energy electrons lead to the development of a novel type of microscope developed by Ernst Ruska and Max Knoll in 1931 exceeding the

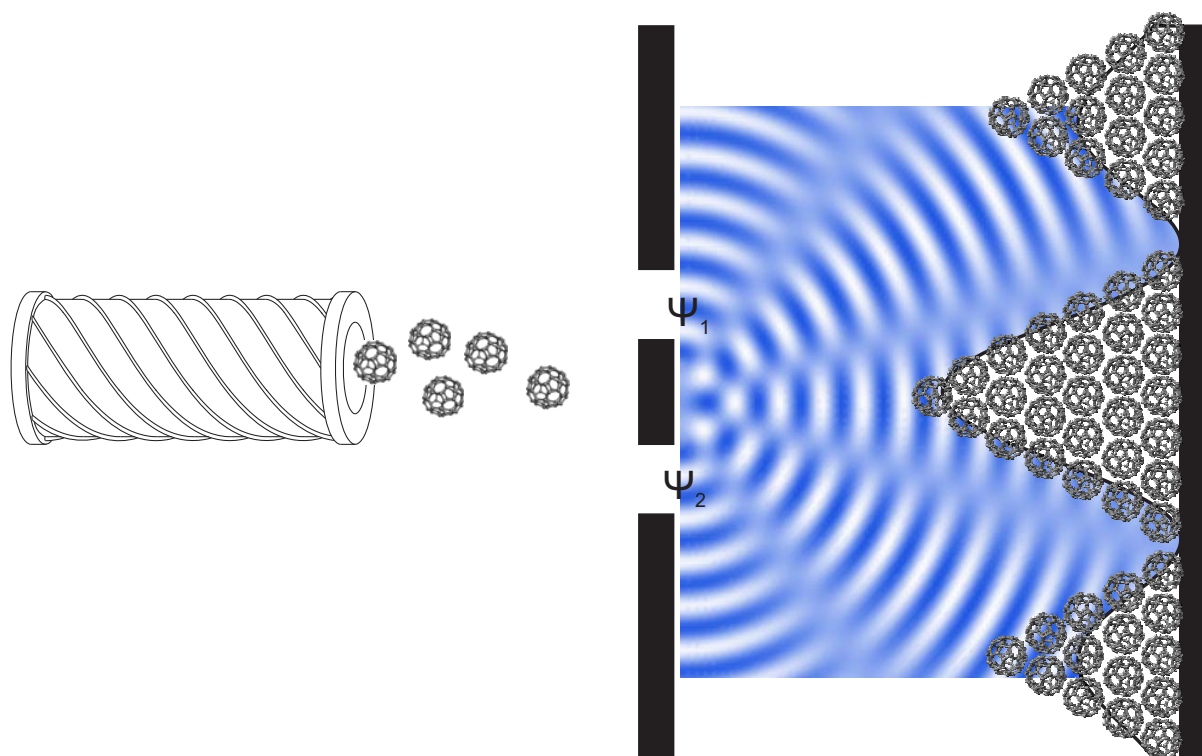


FIGURE 1.1: The double slit represents the prototype experiment for illustrating the wave-particle duality.

resolution of optical microscopes by orders of magnitude. Nevertheless, the first making use of the wave nature of pieces of matter were Clinton Davisson and Lester Germer in 1927 [11], when they fired an electron beam on a single crystal of nickel and discovered a Bragg law for electrons as a result of their wavelike behaviour. Thus de Broglie's hypothesis was confirmed and rewarded the Nobel Prize in 1929.

## 1.2 Double Slit Experiment - The Most Beautiful Experiment in Physics

The concept of this experiment goes back to 1804, when English scientist Thomas Young tried to solve the question about the nature of light [12]. Two parallel slits cut into a thin plate are illuminated by a coherent light source (point source). The elementary, spherical waves emerging from the slits interfere and create a characteristic pattern at the detection screen. For about one century this experiment was indeed the reason that Newton's hypothesis of light particles was discarded. After Albert Einstein had proposed the concept of light quanta, it was Geoffrey Ingram Taylor in 1909, who conducted the

first double slit experiment using a very feeble light source - equivalent to a *candle burning at a distance slightly exceeding a mile* [13]. The light source was so weak that only a single photon at a time was present in the apparatus.

Equipped with a wave equation and a wavelength for material particles one can continue this train of thought to a double slit experiment for matter waves. The first one realizing such an experiment for electrons was Claus Jönsson in 1961 [14]. Followed by Akira Tonomura [15] at Hitachi in 1989 who observed the actual build up of the interference pattern composed of single particles arriving one after the other using a very weak electron source and an electron biprism. One year before that, Zeilinger [16] performed a double slit experiment with neutrons, which are 2000 times heavier than electrons. Their source was so weak that *while one neutron is being registered, the next is still confined to its uranium nucleus inside the nuclear reactor* [17]. The ability of performing experiments with single particles like electrons, neutrons, and later atoms [18], small [19] and large, complex molecules [20] results in what Feynman talked about half a century ago [21]: “We choose to examine a phenomenon which is impossible, absolutely impossible, to explain in any classical way, and which has in it the heart of quantum mechanics. In reality, it contains the only mystery.” It has become the classic gedankenexperiment for illustrating the strange effects which seem to contradict our everyday life experience, the concept of locality, determinism and even reality.

As a consequence of the linearity of the wave equation 1.10 for every single particle with a wave function  $|\psi\rangle$  the superposition principle holds, arriving at the probability of detecting it at a given location  $\vec{r}$ , with  $|\psi_{\text{det}}(\vec{r})\rangle = ||\psi_1\rangle + |\psi_2\rangle|^2$  where  $|\psi_1\rangle$  and  $|\psi_2\rangle$ , represent the spatially separated elementary waves emerging from slit 1 or 2 (an illustrating sketch is given in Figure 1.1). Now we implicitly introduced an interpretation of the wave function, by stating that we can calculate a detection probability, which can be motivated by the actual experimental result, where we see electrons hitting the screen randomly, with an emerging interference pattern after some time. Consequently, the only thing we can say about the outcome of the experiment is that areas exist, where it is less probable for a particle to hit the screen, but where it will actually hits the screen, is determined purely by chance. One must stress at this point that this result has nothing to do with classical randomness, where the stochasticity of the process is only due to imperfect detection apparatus. Here we have to deal with intrinsic and fundamental randomness, which represents something qualitatively new.

Since the interference pattern is composed of single, indivisible particles, here one can ask the question through which slit it actually went through. Measuring that, by monitoring

the two slits results in the disappearing of the interference pattern. Moreover, it has to be pointed out that the actual method of gaining information about the path that the particle took is completely indifferent. It only has to be possible *in principle* to extract information, regardless if it is actually done or not. Thus, we can conclude from the experimental results, that it is impossible to get information about the path of the particle and an interference pattern at the same time. Furthermore, the pure fact of not knowing where the particle actually went through, results in an emerging interference pattern. To owe the words of Nils Bohr, the knowledge of which path the particle took is *complementary* to register an interference pattern. There is only access to one aspect of two complementary *observables*, but not to both at the same time and it is the role of the observer or experimentalist to decide which one he or she wants to have realized. If we continue this train of thought, we arrive at the point where it simply makes no sense to talk about a path the particle took through the interferometer if we have not measured it.

This is further illustrated by John Archibald Wheeler's famous gedankenexperiment, where the method of detection can be delayed to the point where the particle already left the double slit, in order to decide if it actually took one path or should exhibit interference.

However, why is it not possible to experience effects like diffraction and interference of massive particles in everyday life? What are the mechanisms that let our world appear classically? Does a fundamental limit for the quantum interference exist? To this question only the experiment can have the last answer. And a big step towards the answer is the building of interferometers for complex and massive molecules, in order to show, that it is still possible to observe quantum interference, despite their numerous different internal states, their complexity and large mass.

# Chapter 2

## Theoretical Overview

Before the actual theoretical framework is introduced, the line of argumentation which has led to the choice of the specific type of interferometer is discussed. A chronological sequence of the various approaches history brought up is reviewed by discussing the advantages and deficiencies of each setup.

This section is succeeded by the theoretical treatment of the setup. Particular emphasis is layed on the choice of the formalism that allows to stay completely within the framework of quantum mechanics without the necessity of drawing analogous conclusions from classical results. It has to be stressed at this point that the explicit calculations are done elsewhere [22, 23] so that only the main concepts are presented in a rather intuitive way that allows to pursue the train of thought and enables the reader to develop a complete picture.

### 2.1 The Talbot-Lau Interferometer - An Introduction

Over the last century, different approaches have been established with the aim of proving de Broglie's hypothesis that every massive particle is accompanied by a periodic phenomenon. Like mentioned in chapter 1 the first proving the wavelike properties were Davisson and Germer in 1927 [11]. Estermann and Stern [24] demonstrated the diffraction of the hydrogen molecule and Helium on a LiF crystal in 1930. And soon after the discovery of the neutron in 1932 Halban and Preiswerk [25] demonstrated neutron diffraction on MO crystals in 1936. Besides diffraction on crystals, further experiments

with electrons and other particles, up to small molecules [19] have been done, approaching double slit geometry. However, to really explore the transition from the quantum to the classical world, or furthermore realize quantum phenomena on the mesoscopic scale, one must go to far more complex structures than single atoms. Pioneering work on this field has been done in this group in 1999 [20], by diffracting  $C_{60}$  and  $C_{70}$  carbon fullerenes at a nanofabricated diffraction grating with a periodicity of 100 nm. The fact that such a kind of interferometer operates in the Fraunhofer regime, where the characteristic size of the diffraction pattern scales linearly with the wavelength  $\lambda = h/mv \approx 1$  pm and the distance between the grating and the detection screen, it is not suitable for prospective experiments with much larger masses. In addition to that, the requirement for narrow input beam collimation, in order to prevent an overlap of diffraction orders, limits the total source brightness dramatically and represents another disadvantage. A solution to this problem has been found in the so called Talbot-Lau interferometer [26], which operates in the near field or Fresnel regime and uses the self-imaging of a periodic structure, firstly observed by Talbot in 1836 [27] and further described by Lord Rayleigh in 1881 [28]. Rayleigh showed that identical self images of the grating are produced at observation distances that are integral multiples of the Talbot length  $L_T$ . At odd multiples of  $L_T$  an image occurs with the same period, but laterally shifted by half a period. Thus, the first exact image is reproduced at  $2L_T$ . This is further illustrated in Figure 2.1

$$2L_T = \frac{2d^2}{\lambda} \quad (2.1)$$

Chapman et al. carried out an experiment in 1995 [29] in which a collimated beam of sodium atoms was diffracted at a periodic structure and a second, identical grating was used as a mask to observe the Talbot effect and to measure the Talbot length. To get rid of the problems with the source brightness due to collimation with a single slit it is possible to use another grating (a whole array of collimation slits - Lau effect [30]) in front of the diffraction grating in order to prepare the extended, spatially incoherent source properly, to see interference. For the first time such an interferometer was experimentally realized for potassium atoms in 1994 [31] and for  $C_{60}$  molecules in 2002 [26]. Due to the favorable scaling behaviour this is the interferometer of choice for the presented work and is now further elaborated and explained theoretically using the phase space description of quantum mechanics introduced by Wigner [32].

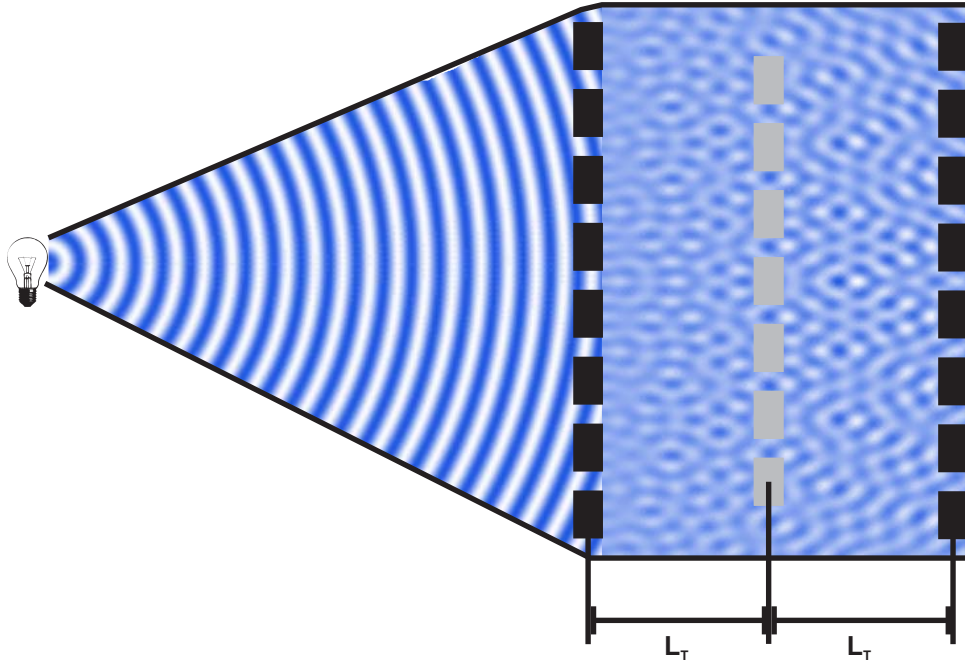


FIGURE 2.1: The Talbot effect. A point like source emits spectrally and spatially coherent light of wavelength  $\lambda$  and illuminates a grating of period  $d$ . The emerging elementary waves propagate, interfere and an exact image of the second grating appears at a distance  $2L_T$

## 2.2 Phase Space Dynamics - The Wigner Function

Werner Heisenberg, Max Born and Pascual Jordan presented in 1925 [33, 34], before Schrödinger published his idea of wave functions, an equivalent way to describe quantum mechanics, using matrices. According to this picture the actual state vector<sup>1</sup>  $|\psi\rangle$  does not vary in time as in the Schrödinger picture, but the actual observables (operators) do vary. Thus an equation of motion for those observables  $\mathbf{A}$  exists,

$$\frac{\partial \mathbf{A}}{\partial t} = \frac{i}{\hbar} [\mathbf{H}, \mathbf{A}] \quad (2.2)$$

where  $\mathbf{H} = \frac{-\hbar^2}{2m} \Delta + V(\vec{r})$  for example represents the Hamiltonian of a particle with mass  $m$  moving in a potential  $V(\vec{r})$  and  $[\mathbf{H}, \mathbf{A}]$  denotes the commutator of  $\mathbf{A}$  and  $\mathbf{H}$ . If now a statistical mixture of *pure* states is regarded, it is not possible to describe the system using a single state vector  $|\psi\rangle$  anymore. Thus, it is convenient to define in analogy to

<sup>1</sup>Heisenberg himself did not speak of state vectors when he invented matrix mechanics. They just represent vectors in a complex space on which the matrices act.

classical statistical mechanics a density matrix  $\rho$

$$\rho = \sum_i p_i |\psi_i\rangle \langle \psi_i| \quad (2.3)$$

where the  $p_i$  represent the statistical weights of the states  $|\psi_i\rangle$ . John von Neumann now showed how this density operator evolves in time according to

$$i\hbar \frac{\partial \rho}{\partial t} = [\mathbf{H}, \rho] \quad (2.4)$$

Another important property can be seen in the fact that the expectation of such observables can be rewritten in the form

$$\langle \mathbf{A} \rangle = \text{tr}(\mathbf{A}\rho) \quad (2.5)$$

### The Wigner Function

By having a closer look at the correction terms, which had to be introduced to classical statistical mechanics due to quantum theory, Eugene Wigner discovered a *quasi-probability function*  $P$ , which could take the place of the classical probability function. But of course  $P$  cannot be really interpreted as the simultaneous probability for coordinates and momenta, as is clear from the fact, that it may take negative values. But of course this must not hinder the use of it in calculations as an auxiliary function which obeys many relations we would expect from such a probability [32].

$$P(x, p) = \frac{1}{\pi\hbar} \int_{-\infty}^{\infty} dy \psi^*(x+y) \psi(x-y) e^{2ipy/\hbar} \quad (2.6)$$

By using the definition 2.3 it can easily be seen that  $P$  can be rewritten in terms of the density operator.

$$P(\vec{r}, \vec{p}) = \frac{1}{h^3} \int d^3s e^{-i\vec{p}\vec{r}/\hbar} \rho(\vec{r} - \vec{s}/2, \vec{r} + \vec{s}/2) \quad (2.7)$$

In order to see the fact that  $P$  can be interpreted as a quasi probability function, one can show that it is possible to write the expectation value of an observable  $A$  in terms of the Wigner function.

$$\langle A \rangle = \text{tr}(A\rho) = \iint d^3r d^3p A(\vec{r}, \vec{p}) P(\vec{r}, \vec{p}) \quad (2.8)$$

Thus,  $P$  really takes the place of the phase space density of classical statistical mechanics, introducing quantum coherences as negative parts of the Wigner function [35]. This enables us to calculate quantum expectation values using the established methods of classical statistical mechanics. Furthermore  $P$  can be seen as the Fourier transform of

the density operator in position representation  $\langle \vec{r}_2 | \rho | \vec{r}_1 \rangle$  which serves as the transition matrix element between the two position eigenstates  $|\vec{r}_1\rangle = |\vec{r} + \vec{s}/2\rangle$  and  $|\vec{r}_2\rangle = |\vec{r} - \vec{s}/2\rangle$

Now coming back to describe the experimental situation, by applying the powerful new tool. Firstly we need to describe the source of our molecules. The molecular beam source we use, consists of a furnace which is resistively heated to high temperatures so that a large amount of molecules transit from the solid to the gas phase. Thus, one expects that the transverse momenta of the particles leaving the furnace orifice to be equally distributed.

$$P_1(\vec{r}, \vec{p}) = \mu(\vec{p}) = \text{const.} \quad (2.9)$$

In equation 2.9 the normalization constant may be disregarded and set to 1, since the normalization can be postponed to the end of the calculation, if required. Provided the quantum mechanical state evolves in a potential that contains only terms up to the second order in position, the time evolution of this quantum states can be described by the classical Liouville equation, even for  $\hbar \neq 0$  [35].

### Free Propagation

Especially, free propagation is of particularly simple form in the Wigner representation and is described by a volume conserving shearing of the Wigner function in phase space. Given the initial value  $P_0$  at time  $t_0$  the Wigner function transforms according to:

$$P_t(\vec{r}, \vec{p}) = P_0\left(\vec{r} - \frac{\vec{p}t}{m}, \vec{p}\right) \quad (2.10)$$

Since the dimension of all the optical elements, such as the source aperture and the gratings, are much smaller than the distance  $L$  between them, a certain degree of collimation can be assumed. Thus, the separation  $\vec{r}$  of the particles from the central interferometer axis can be regarded as small, compared with the distance  $L$ . This results in the separability of the transversal (x component) and longitudinal (z component) parts of the beam state. The longitudinal part then plays the role of an effective time coordinate with  $L = p_z t/m$ . If this is true, only the transverse momentum has to be dealt with and the problem can be simplified to the so called paraxial approximation. Even if the longitudinal momentum, due to imperfect velocity selection, is not perfectly determined and thus rather described by a distribution  $\mu(p_z)$ , the separability of the state makes it possible to weigh the resulting interference pattern with the given velocity distribution.

## 2.3 Description of the Interferometer

The first grating can be described by an array of slits, where every slit is represented by a binary function  $t(x)$ . A general incoming transverse state  $\psi(x)$  experiences an amplitude and phase modulation during the passage through a grating.

$$\psi(x)' = t(x)\psi(x) \quad \text{with} \quad |t(x)| < 1 \quad (2.11)$$

If we now translate this definition to the Wigner representation by using the equations 2.3 and 2.7 it can easily be seen that the Wigner function undergoes a convolution as a result of the passage through a grating.

$$P'(x, p) = \int dq T(x, p - q) P(x, q) \quad (2.12)$$

where  $T(x, p)$  denotes the grating convolution kernel

$$T(x, p) = \frac{1}{2\pi\hbar} \int ds e^{ips/\hbar} t\left(x - \frac{s}{2}\right) t^*\left(x + \frac{s}{2}\right) \quad (2.13)$$

If we now use 2.9 and plug it into equation 2.12 we get the Wigner function  $P_1$  after the first grating.

$$P_1(x, p) = |t_1(x)|^2 \quad (2.14)$$

By making use of the time evolution property of the Wigner function 2.10 and the definition for the passage through a grating 2.12 leads to the Wigner function at the position of the detection screen at the distance  $L_2$  after the second grating

$$P_d(x, p) = P_2'\left(x - \frac{p}{p_z}L_2, p\right) \quad (2.15)$$

$$P_2'(x, p) = \int dq T(x, p - q) P_2(x, q) \quad (2.16)$$

$$P_2(x, p) = P_1\left(x - \frac{p}{p_z}L_1, p\right) = t_1\left(x - \frac{p}{p_z}L\right) \quad (2.17)$$

Thus one can summarize the features of the Wigner function which are most important for our application as the following:

- Propagation is reflected in a simple coordinate transformation
- Transmission is described by a convolution

These two properties drastically simplify the description of the experimental situation, since a coordinate transformation and convolution are far easier to handle than Fresnel integrals if the conventional wave description from classical optics is used. Moreover, the Wigner representation allows to use density matrices which is perfectly suitable for the description of thermal beam state. In addition to that, perturbations can be implemented into the description in a very convenient way. This is further elaborated in section 2.4

One starts from the incoherent, thermal beam with a longitudinal momentum distribution  $\mu(p_z)$  and a constant Wigner function  $P_1$  (equation 2.9) going through the first grating. The density modulation of the beam due to the periodic grating function  $t_1(x)$  results in  $P'_1$ , which is propagated by a distance  $L_1$  to the second grating, using equation 2.10, where a phase modulation due to coherent illumination takes place and results in  $P'_2$ . After another propagation of distance  $L_2$  to the detection screen, the final Wigner function  $P_d$  appears to be

$$P_d(x, p) = \int dq T \left( x - \frac{p}{p_z} L_2, p - q \right) \left| t_1 \left( x - \frac{p}{p_z} L_2 - \frac{q}{p_z} L_1 \right) \right| \quad (2.18)$$

The projection of  $P_d(x, p)$  on to the space coordinate yields the spatial interference pattern  $P_d(x)$  in terms of the Wigner function.

$$P_d(x) = \iint dp dq T \left( x - \frac{p}{p_z} L_2, p - q \right) \left| t_1 \left( x - \frac{p}{p_z} L_2 - \frac{q}{p_z} L_1 \right) \right|. \quad (2.19)$$

### 2.3.1 Fourier Decomposition of the Diffraction Gratings

In order to obtain a more quantitative result of 2.19 we shall now consider the particular transmission function  $t_1$  for a grating of periodicity  $d$ . Whereas the finite lateral extension of the gratings, affects only the transmitted signal strength and thus allows to describe the gratings by a standard one dimensional Fourier decomposition.

$$t_1(x) = \sum_n a_n e^{2\pi i n \frac{x}{d}} \quad |t_1(x)|^2 = \sum_l A_l e^{2\pi i n \frac{x}{d}} \quad \text{with} \quad A_l = \sum_j a_j a_{j-l}^* \quad (2.20)$$

By inserting equation 2.20 into the definition of the convolution kernel 2.13 and by making use of the definition of the delta function  $\delta(f) = \int dt 1 \cdot e^{-i2\pi ft}$  we get the decomposed

integral kernel which is called the *grating kernel*

$$T(x, p) = \sum_{m,n} b_n b_{n-m}^* e^{2\pi i m \frac{x}{d}} \delta \left( p - (2m - n) \frac{\pi \hbar}{d} \right) \quad (2.21)$$

Now the actual beauty and simplicity of this formalism can be seen clearly. Starting from the definition of the Wigner function 2.7 and the obvious transformation 2.12 (amplitude modulation of the incoming incoherent beam for the preparation of coherence with a subsequent phase modulation at the second grating) of a state passing through a grating combined with the simple rules of Fourier decomposition 2.20 of periodic functions lets quantum interference appear in the form of a Dirac delta function, which displaces an incoming coherent state by multiples of  $\pi \hbar / d$ . Putting everything together and rearranging it using the property of the delta function

$$f(T) = \int dt f(t) \delta(t - T) \quad (2.22)$$

we arrive at the Wigner function  $P_d(x, p)$  in the detector plane with

$$P_d(x, p) = \frac{1}{\hbar} \sum_{l,m,n} A_l b_n b_{n-m}^* e^{i\pi l(2m-n) \frac{L}{L_\lambda}} e^{2\pi i(l+n) \frac{x}{d}} e^{-2\pi i(2l+n) \frac{L}{d} \frac{p}{p_z}} \quad (2.23)$$

where we introduced the Talbot length

$$L_\lambda = \frac{d^2 p_z}{\hbar} = \frac{d^2}{\lambda} \quad (2.24)$$

In order to get the spatial interference pattern one must integrate over the momentum variable which leads to Fourier decomposed result of 2.19

$$P_d(x) \propto \sum_l A_{-l} B_{l,m} \frac{L}{L_\lambda} e^{2\pi i l \frac{x}{d}} \quad (2.25)$$

Here the Talbot-Lau diffraction coefficients  $B_{l,m}(\xi)$  have been introduced which can be regarded as the Fourier components of a shifted product of the transmission functions  $t(x)$ .

$$B_{m,n}(\xi) = \sum_j b_j b_{j-n}^* e^{i\pi l \xi (n-2m)} \quad (2.26)$$

Furthermore, the  $B_{m,n}$  are called the Talbot-Lau diffraction coefficients due to the restriction condition  $m = -2n$  which ensures that the spatial distribution of the interference pattern at distances  $L_\lambda = kL_\lambda$  equals the grating profile  $|t(x + kd/2)|^2$  which is consistent with the experiments of Talbot.

In addition to that it can be easily seen by inserting a plane wave in z-direction with  $w(x, p) = \delta(p)$  into the definition of the state transformation 2.17 with the grating kernel of 2.21 and a consequent  $p$  integration in order to get the spatial interference pattern. One has to stress that the result 2.25 is only valid for a symmetrical setup where the grating distance  $L$  is the same as the distance between the second grating and the detection surface. Moreover the grating constant of both gratings is considered equal.

It can be seen clearly that the quality of the interference pattern 2.25 depends considerably on the de Broglie wavelength  $\lambda$  and the distance  $L$  between the gratings and the detection screen. If we now consider the effect that due to reasons of geometry the first grating is not illuminated by a totally incoherent mixture of momenta  $p$  but rather by a restricted distribution  $D(p/p_z)$  the resulting interference pattern reads

$$P_d = \sum_l A_l B_{l,2l} \left( \frac{L}{L_\lambda} \right) e^{2\pi i(m+l)\frac{x}{d}} \tilde{D} \left( 2\pi \frac{L}{d}(2l+m) \right) \quad (2.27)$$

with the Fourier integral of the angular momentum distribution

$$\tilde{D}(\omega) = \int \frac{dp}{p_z} e^{-i\omega \frac{x}{p_z}} D \left( \frac{p}{p_z} \right) \quad (2.28)$$

Corresponding to optics we take as a measure for the distinctness of the interference fringes 2.27 their *visibility*  $V$ , defined by

$$V = \frac{P_{d,max} - P_{d,min}}{P_{d,max} + P_{d,min}} \quad (2.29)$$

One has to bear in mind that this definition of the visibility 2.29 makes only sense if the expected signal exhibits a sinusoidal dependence. Since this is true for the presented setup the definition holds, but one has to stress that this must not be true for other configurations.

At this point one must admit that the symmetrical setup presented, is the standard choice for matter wave interferometry [36], but is not the only possibility to make use of the Talbot effect in order to create images of the second grating by means of interference. Moreover, even magnifying or demagnifying interferometers can be realized using an asymmetrical setup with gratings of different periodicity which is referred to as the *fractional Talbot effect*.

However, to make sure that the density pattern on the detection surface stems from the quantum wave nature of the molecules, one must proof, on the one hand, that the

visibility defined in equation 2.29 depends on the velocity and thus on the de Broglie wavelength  $\lambda$  of the molecules or, on the other hand, choose the opening fractions (the ratio of slit width to period) of the gratings in a way that a classical Moiré image of the second grating is in principle impeded. A specific calculation for a visibility that stems from a classical shadow image is given in [22]. Since a precise distinction of both visibilities is of utmost importance, a numerical simulation comparing these two effects represents the foundation for a successful experiment. The result of such a simulation, developed in [37], is depicted in Figure 2.2.

At this point one has to emphasize that for all the calculations an ideal grating has been considered without taking account for the interaction between the particles and the grating walls. In order to do so, the usual way is to use the *eikonal approximation* which adds a phase factor to the binary function  $t(x)$  for a grating of thickness  $b$

$$\tilde{t}(x) = t(x)e^{-\frac{i}{\hbar} \frac{mbV(x)}{p_z}} \quad (2.30)$$

Regarding this additional phase factor, the grating kernel  $T(x, p)$  and the Talbot Lau diffraction coefficients  $B_{m,n}$  have to be modified respectively. Furthermore, it can be seen that the effect of an interaction potential  $V(x)$  introduces also a velocity dependence on the classical level and in general has severe effects on the visibility. The interaction between the particle and the material grating has been described by Casimir and Polder [38] in 1948 by introducing a potential  $V(x) = -C_4/x^4$  which reduces to the van der Waals Potential  $V(x) = -C_3/x^3$  for close distances to the grating walls, where the interaction constants  $C_3, C_4 > 0$  depend on the used material.

In Figure 2.2 the expected visibility is depicted as a function of the longitudinal velocity. On the one hand, the theoretically expected visibility is displayed, including all Fourier components (red line). On the other hand, the experiment yields a sinusoidal dependency which is reflected in the first Fourier coefficient only (blue line). Thus, the visibility extracted from a sine-fit to the experimental data yields a slightly higher visibility than theoretically expected. Furthermore, we observe an additional visibility peak at about 70 m/s, which is absent if only the first Fourier coefficient is considered. The maximum contrast is expected for a velocity of 112 m/s if the Talbot length is set to  $L_T = 12.5$  mm. Moreover, it can be seen that the expected classical contrast (green line) is close to zero for the correct velocity of the molecules.

For forthcoming experiments with molecules even larger than  $C_{60}$  fullerenes it is of utmost importance to overcome the limiting effects due to the interaction with the grating walls,

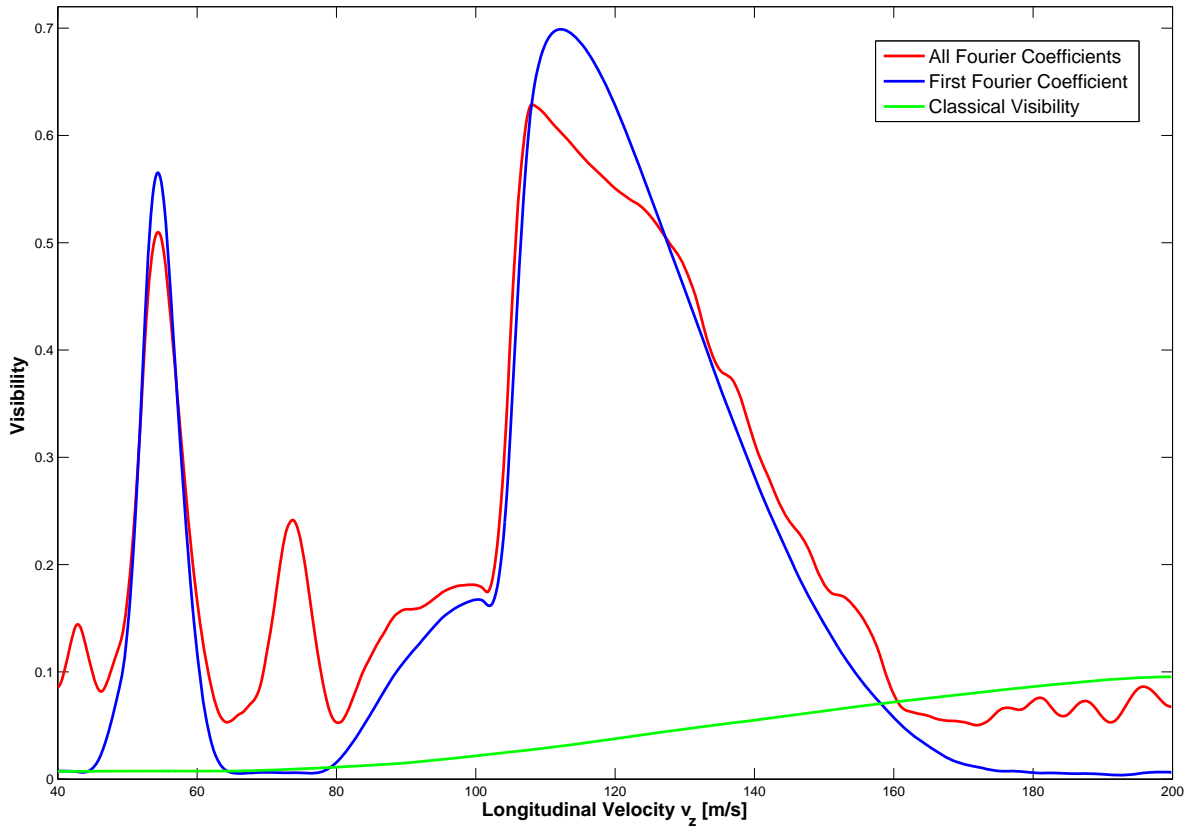


FIGURE 2.2: The calculated dependence of the visibility as a function of the longitudinal velocity.

if one still wants to use a thermal beam source. The challenge lies in the nature of the expected Maxwell-Boltzmann distribution of the molecular velocities which is shifted to low speeds for increasing masses.

On the one hand, this is a very favorable scaling behavior because it increases the de Broglie wavelength, but on the other hand also the interaction time with the grating walls is increased which has severe effects on the expected visibility. In order to avoid that a Kapitza-Dirac-Talbot-Lau interferometer was recently demonstrated [39], where the actual diffraction grating is replaced by a pure optical phase grating. Such an optical phase grating in combination with a highly efficient surface detection scheme represents a promising extension of the recent setup and will be a key point of considerations for future experiments.

## 2.4 Decoherence

Before we conclude this chapter let me briefly summarize the theory of decoherence developed in [22] which will be needed in the succeeding chapter to estimate the pressure requirements of the setup. If a fullerene molecule interacts with other degrees of freedom (scattering of a residual gas particle), entanglement between the molecule and the environment leads to a reduction of the expected visibility. The scattered particle carries which-path information which could be in principle read out. For particles with the state  $\rho(r, r')$  changes

$$\rho'(r, r') = \rho(r, r')\eta(r - r') \quad (2.31)$$

Here  $\eta(r - r')$  indicates the decoherence function which describes the decay of the off-diagonal elements, or coherences, in the density matrix  $\rho(r, r')$ . Starting from this point it continues in the usual way. First the Wigner function is constructed. The state is propagated to the position  $z$  where the scattering event takes place then 2.10 is applied and further propagated to the position of the surface. Finally a momentum integration yields the position density  $P_d(\vec{r})$  at the detection surface. The grating function is decomposed into its Fourier components which gives the transformation for the visibility that determine the Talbot-Lau diffraction components

$$B'_m = B_m \eta \left( -m \frac{d}{2} \frac{L - |z - L|}{L_\lambda} \right) \quad (2.32)$$

If we then ask for the change of the visibility as a function of the occurring decoherence effects (with Rate  $R(z)$ ) the solution of a simple linear ordinary differential equation leads us to

$$V = V_0 e^{-\int_0^{2L} R(z) \left( 1 - \eta \left( -d \frac{L - |z - L|}{L_\lambda} \right) \right) dz} \quad (2.33)$$

with  $V_0$  representing the visibility in absence of decoherence events. We therefore expect an exponential decay of the visibility as a function of the occurring scattering events.

In this chapter we have become acquainted with a very powerful formalism which enables us to calculate the experimental outcome in a rather straight forward and analytical way, while we always remain within the mathematical framework of quantum mechanics. The Wigner function even allows us to predict the effects of classical mechanics due to the analogy to the classical phase space density. Thus, the presented description of the setup suits very well as a means for providing theoretical evidence for the expected experimental results and the adjustment requirements for the interferometer which will be dealt with in the next chapter. Furthermore, it can be concluded that the interference fringes

---

emerging at the location of the detection surface stem from the de Broglie wavelength  $\lambda$  associated with a particle propagating through the interferometer. However, in order to distinguish the resulting interference pattern from a classical shadow image one has to choose the opening fractions, lengths and the divergence of the molecular beam in a way that only a diminishing classical visibility is expected. Finally, we can regard the presented interferometer as a powerful, lens free imaging tool of periodic structures by applying the Talbot effect to matter waves.

# Chapter 3

## On the Road to Quantum Interference - The Experimental Realization

Quantum interference of single, massive carbon fullerenes, recorded on a detection screen and read out with single atom resolution, in order to elucidate the wave-particle duality in its most fascinating way is the goal that has to be reached. An instruction manual on how to build an apparatus which enables us to reach this goal is presented in this chapter. Firstly a complete picture of the experimental setup is given, which is succeeded by a detailed discussion of the particular parts and specified by the typical demands that have to be accomplished.

The chapter is concluded by a chronological presentation of the real experimental situation which is supported by experimental subtleties and particular results.

### 3.1 Overview of the Experimental Setup

Before the actual parts of the experimental setup are presented let me briefly sketch the pressure requirements that have to be met because they essentially influence the design of the apparatus. From chapter 2 we can derive that the expected visibility is determined by the number of decoherence events occurring during the flight of the particle through the interferometer.

The most natural source for such decoherence events is the scattering of background pressure particles at the molecules flying through the interferometer. Thus, the residual background pressure plays a crucial role in this experiment. On the one hand, to prevent collisional decoherence of the wave-function by reducing the number of occurring decoherence events and the contamination of the sample surface due to the deposition of residual gas on the other. If we now want to quantitatively estimate the required pressure conditions for a successful experiment with fullerenes we have to find an appropriate decoherence function  $\eta(r, r')$  from equation 2.31. The rate  $R(z)$  of decoherence events is constant over the whole space and depends only on the density of the gas environment, the effective total cross section of the molecules and the length of the interferometer.

### 3.1.1 Decoherence

Furthermore, the average reciprocal momentum kick due to the scattering with a residual gas particle is by orders of magnitude smaller than the path separation  $\Delta r \approx z\lambda/d$  of the delocalized molecule. This high resolution leads to the fact that a single scattering event is enough to localize the molecule and destroy the coherences in the density matrix completely. Thus the actual decoherence function is solely determined by the effective cross section  $\sigma_{\text{eff}}$ .

$$V(p) = V_0 \exp\left(-\frac{2L\sigma_{\text{eff}}}{k_B T} p\right) \quad (3.1)$$

If we assume a conservative effective cross section [40] of  $\sigma_{\text{eff}} = 100 \text{ nm}^2$  which is about a hundred times larger than the geometric cross section and a Talbot length of  $L = 12.5 \text{ mm}$  we get a limiting background pressure of  $1.7 \cdot 10^{-6} \text{ mbar}$  for which still a visibility of  $V > 0.9 \cdot V_0$  is expected. Thus we can conclude from this estimation the need for a vacuum chamber which is pumped to pressures of roughly  $10^{-7} \text{ mbar}$ .

### 3.1.2 Contamination of the Sample Surface

The detection scheme is able to resolve single atoms on a surface. Thus, one has to make sure that only the desired molecules are deposited on the surface. Although it would be in principle possible to distinguish deposited background gas particles from large fullerenes it is on the one hand very laborious and on the other, if the sample surface itself is contaminated the molecules will not become immobilized. Hence, one has to make sure that the average deposition rate of the background gas stays well below the

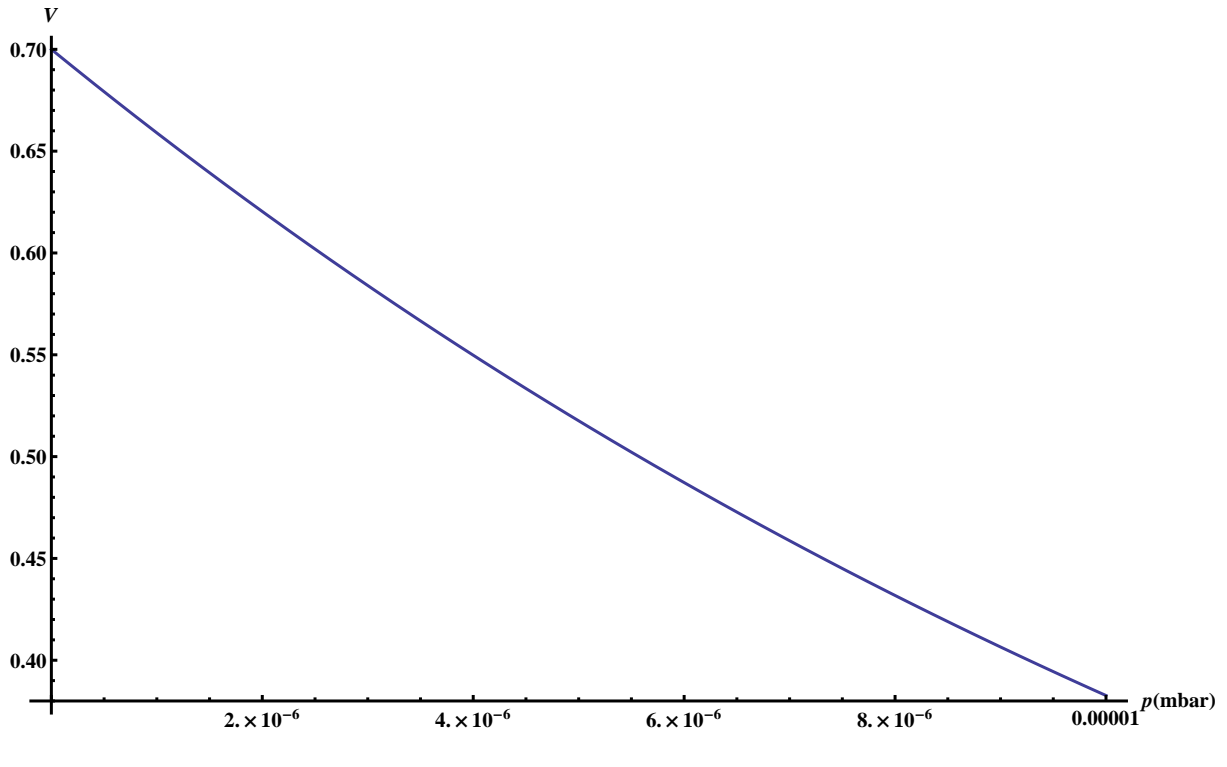


FIGURE 3.1: The expected visibility as a function of the background pressure

time of the entire experiment. For estimating the time that is available when studying surfaces at a given background pressure the term *monolayer time* [41] has been invented. This value describes the time for the creation of a mono layer on the sample surface under the precondition that every rest gas molecule adheres permanently if it hits the sample surface. If the radius of a typical adsorbing molecule is  $1.6 \cdot 10^{-10}$  m the number of particles per  $\text{cm}^2$  is on average  $10^{15}$  if a single particle occupies a close packed area  $A = 2\sqrt{3}r^2$ . If we now assume air as a rest gas with a mass  $M \approx 29^1$ , at room temperature  $T = 300$  K we arrive at the useful relation

$$t[s] = \frac{3.6 \cdot 10^{-4} Pa}{p[Pa]} \quad (3.2)$$

Since Nitrogen is pumped very effectively and is relatively non-reactive due to its strong bond one can assume that it plays a minor role in the contamination process. Hence, the above stated result is a very conservative estimate. The actual experiment in the interferometer chamber takes about half an hour. Thus, a pressure of less than  $10^{-9}$  mbar is necessary which yields a monolayer time of roughly one hour. This is followed by the evaluation of the experiment which can take up to two days and demands pressures of

<sup>1</sup>A weighted average of  $\text{N}_2$ ,  $\text{O}_2$  and Ar

below  $10^{-10}$  mbar. The distinct parts of the experimental setup and the methods of how to meet this ambitious preconditions is the issue of the succeeding section.

### 3.1.3 The Experimental Setup

The entire vacuum setup is parted into three logical sections: The source, the nanolithographic deposition accommodating the interferometer and the analysis, housing a scanning tunneling microscope. As can be derived from the above stated preconditions, an extremely good vacuum environment must be accomplished. Thus differential pumping stages are installed to ensure continuous operation under consistent preconditions and to allow the sample surface to be transferred without the need of venting the ultra high vacuum (UHV). The whole setup is rigidly mounted onto an optical table with pneumatic vibration isolation. Due to the fact that different velocity selection schemes have been tested during this thesis the setup has to be adapted accordingly.

#### The Transfer Chamber

The first step when performing an experiment is that the sample must be transferred into the analysis chamber for preparation. In order to do so, the transfer chamber which is usually hold at a pressure level of  $10^{-8}$  mbar by a turbomolecular pump<sup>2</sup> with a pumping speed for  $N_2$  of 59 l/s is vented with pure nitrogen through a full metal leak valve. Venting with pure nitrogen prevents gases with low compressibility to enter the chamber. This has favorable effects on the time to reach the desired pressure level. The sample is put onto the fork of a wobble stick, the load-lock gate is closed and the chamber is pumped to a pressure  $10^{-7}$  mbar within an hour. Then the UHV gate valve that connects the transfer chamber with the transfer cross can be opened.

#### The Transfer Cross

Using a transfer rod the sample surface is moved into the transfer cross. This chamber is pumped by a small ion getter pump<sup>3</sup> with a pumping speed for  $N_2$  of about 35 l/s<sup>4</sup> leading to a base pressure of  $< 10^{-9}$  mbar. This low pressure is very important because this chamber connects the two major parts of the experimental setup. Solely for the fact that the exposed sample has to be transferred through this part demands good vacuum conditions.

---

<sup>2</sup>Pfeiffer Vacuum Technology AG - Compact Turbo TMU 071 P

<sup>3</sup>Varian VacIon Plus 20 Diode

<sup>4</sup>The pumping speed varies with decreasing background pressure thus a typical mean value is given

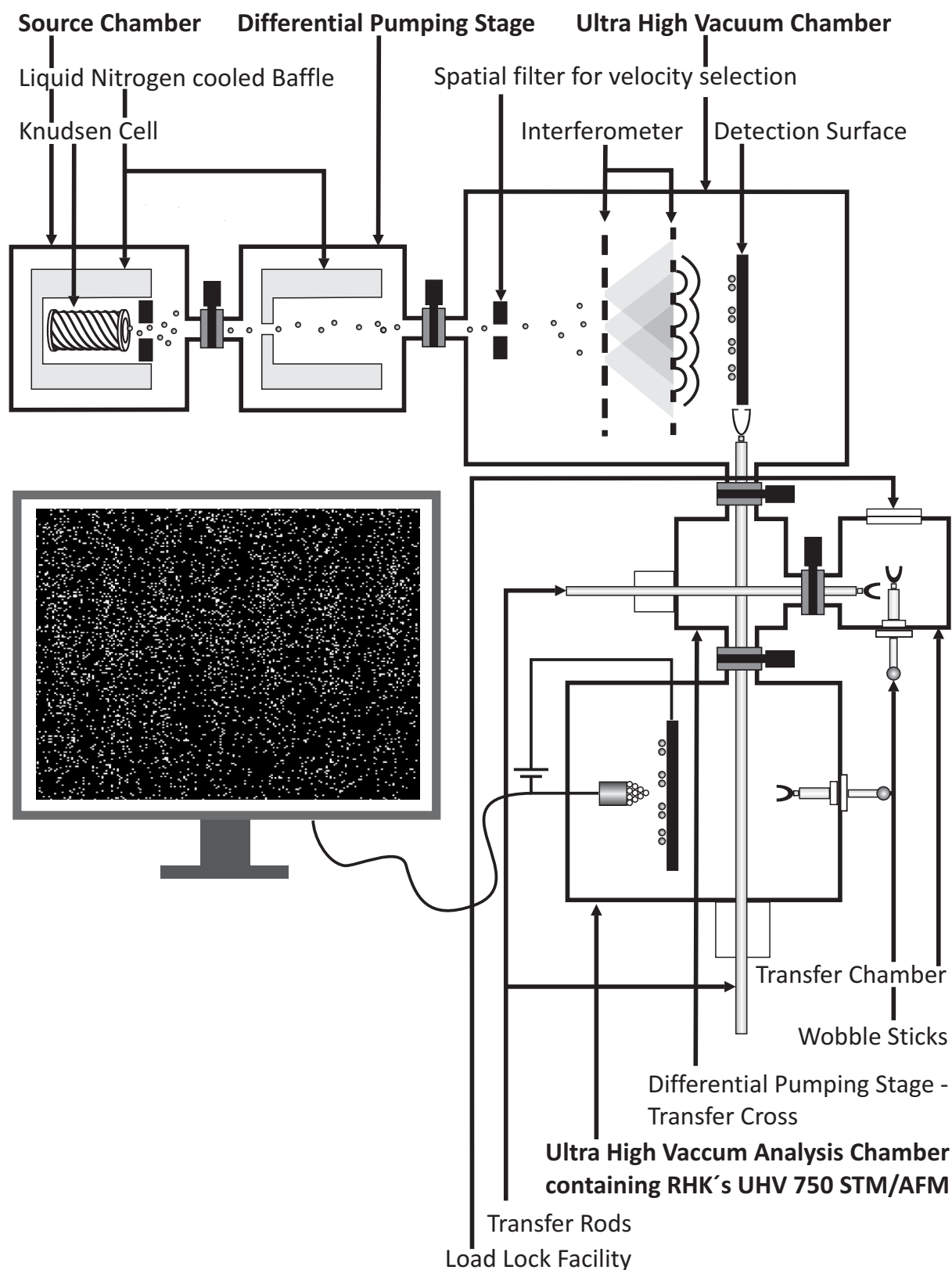


FIGURE 3.2: The experimental setup with gravitational velocity selection. A supplementary differential pumping stage between the source and the lithography chamber containing the interferometer is installed. In order to operate the source at temperatures up to  $800\text{ }^{\circ}\text{C}$  differential pumping with liquid nitrogen cooled baffles must be implemented to limit the base pressure in the source chamber to  $1 \cdot 10^{-7}$  mbar

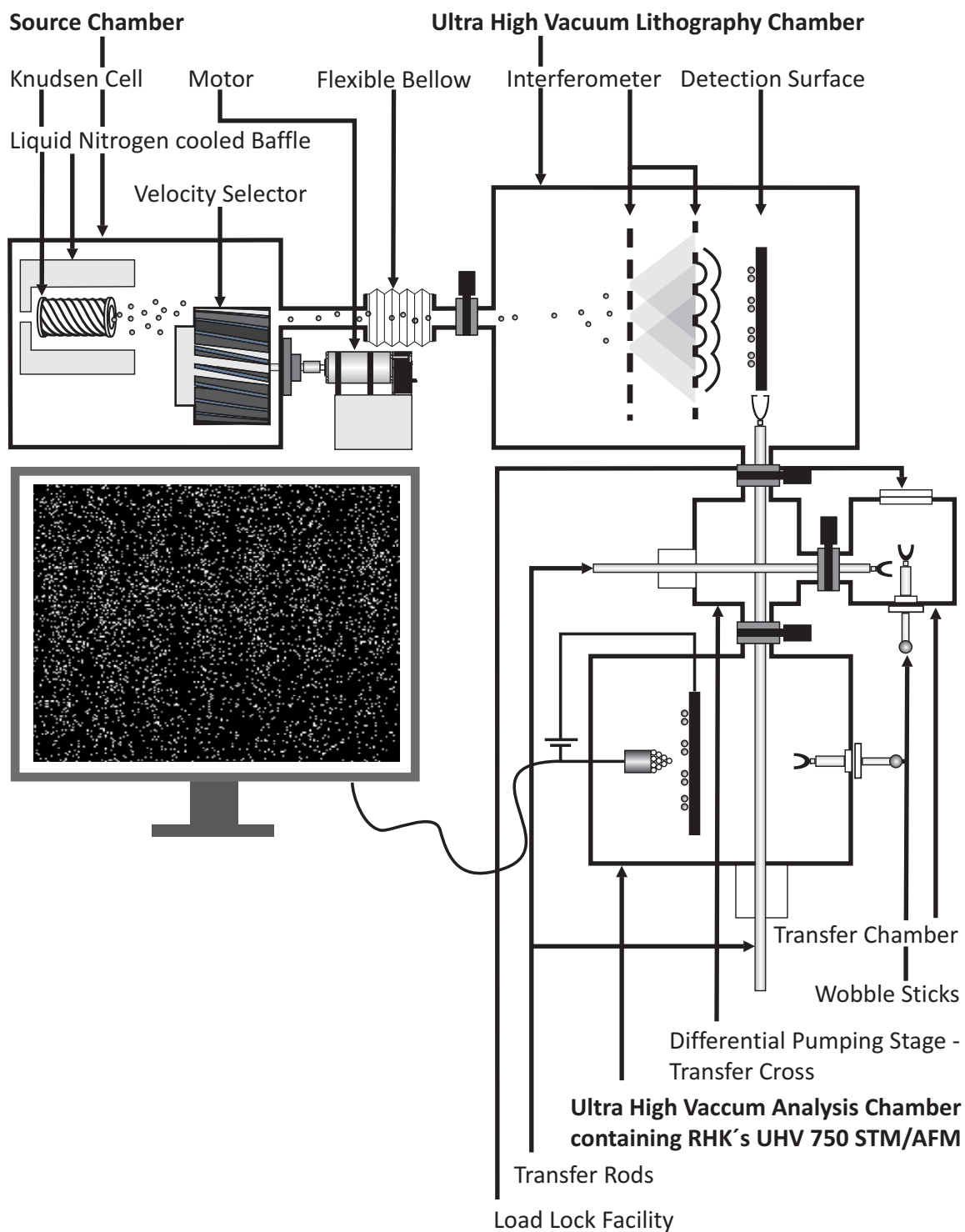


FIGURE 3.3: The experimental setup with the helical velocity selector. The differential pumping stage between the source and the interferometer chamber is replaced by a vibration isolating bellow which dampens the perturbations that stem from the fast rotating velocity selector.

## The Analysis Chamber

After the sample has reached the transfer cross the valve to the transfer chamber is closed again. A few minutes later the pressure is low enough to open the valve to the analysis chamber. At this point the second transfer rod is used to move the sample into the analysis chamber where it is placed onto the sample holder.

The analysis chamber houses the commercial UHV 750 STM/AFM of *RHK Technology* with internal spring suspension and eddy current dampening system. Equipped with such powerful techniques, perturbation due to mechanical influences is effectively damped which allows high stability. Furthermore, a liquid helium cryostat is attached to the vacuum chamber that allows scanning at cryogenic temperatures beneath 25 K.

In order to avoid vibrations due to rotating turbomolecular pumps and the need for even lower pressures than  $1 \cdot 10^{-10}$  mbar the choice was made to use a combination of an ion getter pump with a titanium sublimation pump. This is a well-known option for creating an ultra high vacuum environment. The titanium sublimation pump offers extra high pumping speed for getterable gases (especially for hydrogen with 1580 l/s) whereas the ion pump handles the non getterable gases like argon and methane. With this combination pressures below  $10^{-11}$  mbar are in principle possible.

## The Source Chamber

The source chamber itself is primarily evacuated by a turbomolecular pump<sup>5</sup> with a pumping speed of 210 l/s for  $N_2$ . It contains a resistively heated furnace that serves as the source for the particular molecular species. This furnace only provides a dense molecular beam if the vacuum conditions are good enough. This point is further elaborated in chapter 3.2.

The molecules leave the furnace orifice with a broad angular distribution, but only the small fraction which is close to the central interferometer axis is useful and the remaining molecules simply deteriorate the vacuum conditions. Thus, they have to be removed efficiently. This is realized by a cold shielding coil made from 6 mm copper tube. Liquid nitrogen is pumped through this coil which has the favorable effect that a large fraction of the molecules that leave the furnace in the *wrong* direction are adsorbed at the cool surface of the shield. In addition to this, the heat of the furnace is shielded from the chamber walls which is another positive effect on the resulting pressure level. This does

---

<sup>5</sup>Pfeiffer CompactTurbo TMU 261

not exceed  $1.5 \cdot 10^{-7}$  mbar during the whole experiment which is low enough so that no reduction of the signal is expected due to collisions with the rest gas molecules [42].

### **Differential Pumping Stage**

Depending on the velocity selection scheme an optional differential pumping stage can be inserted between the source and the interferometer chamber to even further improve the vacuum conditions. This chamber is pumped by a turbomolecular pump with a speed of 68 l/s for  $N_2$  and further supported by a small baffle which is cooled with liquid nitrogen.

### **The Interferometer Chamber**

Separated from the differential pumping stage by a UHV shut-off valve the interferometer chamber houses the heart of the experiment - the Talbot-Lau near field interferometer. This chamber again has to be pumped to ultra high vacuum conditions of  $1 \cdot 10^{-10}$  mbar with the same type of combination pump as the analysis chamber.

#### **3.1.4 The Bake-out Procedure**

Usually one must wait for a long period of time before the above stated pressure levels are reached. In order to accelerate that, the vapor pressure of all out gassing materials can be temporarily raised by baking the whole vacuum apparatus. Hence the whole setup has to be isolated from the environment and heated to about 110 °C. This is realized by the use of drywall panels with a thermal conductivity of 0.5 W/mK which is sufficient for that purpose. Two heater fans with 2.5 kW heating power provide even and gentle heating of the system with an air circulation of 200 m<sup>3</sup>/h. Supported by fiber braided heating tapes for the transfer rods and the built-in heating filaments of the getter pumps (100 V is applied usually to both) a pressure of  $1 \cdot 10^{-10}$  mbar in the interferometer chamber and even less than that in the analysis chamber is reached within three days. The bake out procedure is started when an overall pressure of  $1 \cdot 10^{-7}$  mbar is reached. The first day is used to continuously increase the temperature which is monitored by the use of thermocouples attached to and inside the vacuum chambers. During the whole of the second day the apparatus is held on the objected temperature of 110 °C. Furthermore, it is useful to outgas the titanium filaments continuously at a current of 35 A.

During this time all the valves remain open so that the remaining gas is effectively removed by the turbopumps. On the third day all the heating elements are switched off, but without removing the drywall panels yet in order to avoid too large temperature gradients.

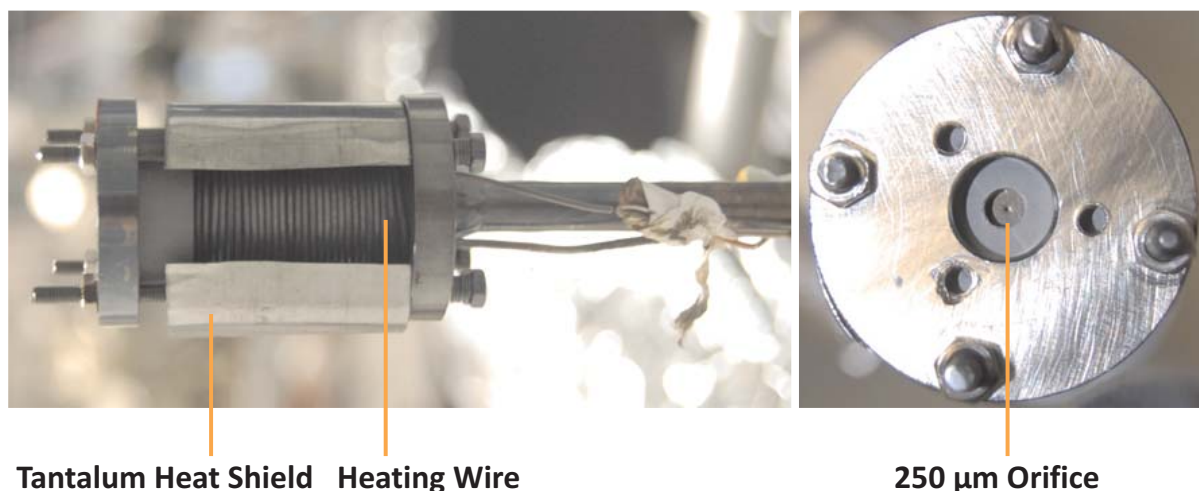


FIGURE 3.4: The molecular beam source. A ceramic crucible contains the molecular specimen and is circumvented by electrically isolated heating wire. With a heating power of 80 W a temperature of 800 °C is reached. A thermocouple attached to the inside of the ceramic crucible is used to measure the temperature.

Subsequently the sublimation pumps are switched on to perform flashing cycles of two minutes at a current of 45 A every hour. After the temperature decreases to about 50 °C the drywall panels are removed and the valves are closed. As a last step it is very important to degas the various pressure gauges. Then it takes about 24 – 36 hours for the system to cool down totally and to reach its final pressure level.

## 3.2 Molecular Beam Source

### 3.2.1 The Molecules - Carbon Fullerenes

Choosing the right molecule is a non-trivial task. Not only regarding the numerous possibilities but also the requirements it has to satisfy. First, it is of great advantage if the molecule is commercially available in rather large amounts (e.g.: a few grams) and high purity (99.5-99.9%). A clean source is of great convenience because only then the detection scheme does not need to be mass selective. Especially the presented detection scheme where a surface serves as a detection screen is particularly sensitive to contaminations of the source. Impurities have different masses which correspond to different wavelengths and result in the blurring of the expected interference pattern if the impurities cannot be distinguished from the actual probe by their height or shape.

Moreover, the source must provide on the one hand an intense beam of molecules so that the exposure time of the sample surface remains in a reasonable dimension (30 minutes) and on the other hand a sufficient dilute beam that one can still speak of single particle interference.

Regarding all these limiting factors the soccer-ball-like fullerene  $C_{60}$  seemed to be a promising candidate fulfilling the above stated restrictions. It is commercially available from different companies in rather large quantities due to the invention of a novel synthesis process by Krätschmer and Huffman in 1990 [43]. In general, the class of fullerene molecules does purely consist of carbon atoms arranged in a specific way (e.g.: the hollow sphere *buckyball*  $C_{60}$  with a cage diameter of 0.7 nm or the cylindrical carbon nanotubes).

The discovery [44] of this new form of carbon, apart from diamond and graphite was awarded the 1996 Nobel Prize in Chemistry and initiated a flourishing field of research. Furthermore, the generation of a molecular beam using  $C_{60}$  appears to be rather simple. The development of such molecular beam sources was triggered by the invention of molecular beam epitaxy by J.R. Arthur and Alfred Y. Cho during the 1960s, where single layers of a sublimed material (e.g.: Gallium, Arsenic) are deposited on a target wafer. Usually a ceramic crucible (aluminum oxide, pyrolytic boron nitride, shapal-m) which contains the molecules is heated resistively by a tungsten wire coiled around the vessel to high temperature which is monitored by a thermocouple attached to the ceramic crucible.

### 3.2.2 Properties of the Beam Source

If an enclosure containing the molecular specimen (sublimed  $C_{60}$  from MER corporation with 99.9% purity) is heated to the temperature  $T$ , the established equilibrium between the gas and condensed phase can be approximately described by the Clausius-Clapeyron relation

$$p(T) = Ae^{\frac{-\Delta H}{k_B T}} \quad (3.3)$$

where  $\delta H^6$  is the sublimation enthalpy and  $k_B^7$  the Boltzmann constant.

---

<sup>6</sup> $\delta H_{C_{60}} = 181.4 \text{ kJ/K}$  [45]

<sup>7</sup> $k_B = 1.38 \cdot 10^{-23} \text{ J/K}$

An ideal Knudsen cell<sup>8</sup> consists of a relatively large enclosure with a rather small orifice so that the equilibrium pressure is not disturbed. If it is operated in the molecular flow regime the mean free path  $\Lambda = kT/p\sigma_{col}$ <sup>9</sup> is larger than the furnace aperture  $b$ . So the Knudsen number  $K = \Lambda/b > h/b > 8$ , where  $h$  stands for the internal dimensions of the effusion cell [46]. For a given temperature  $T = 1070$  K the relation for the vapor pressure of  $C_{60}$  as a function of the temperature reads according to [47]

$$\log_{10}(p) = 8.28(\pm 0.20) - \frac{9154(\pm 150)}{T} + 3 \quad (3.4)$$

This yields a vapor pressure of  $p \cong 560$  Pa. The mean free path is the average distance between two collisions for a gas molecule which can be estimated from kinetic gas theory where the effective collision area  $\sigma_{eff} = \pi \cdot d^2$  is approximated by a circle of  $2d$ , where  $d$  is the diameter of the molecule. Using the ideal gas law, one arrives at the following expression for the mean free path

$$\Lambda = \frac{kT}{\sqrt{2}\pi d^2 p} \cong 6 \cdot 10^{-6} \text{ m} \quad (3.5)$$

The factor of  $\sqrt{2}$  in equation 3.5 appears in order to account for the high average relative velocity. If we compare the mean free path now with the spatial filter of  $50 \mu\text{m} \times 2 \text{ mm}$  which is used as the furnace orifice we see that the Knudsen number  $K \cong 0.1$  does not meet the above stated requirements to be operated in the molecular flow regime. Thus the expected molecular flux out of the orifice reads according to [48]

$$\frac{dN}{dt} = \frac{2}{\gamma + 1} \frac{\gamma + 1}{2(\gamma - 1)} \sqrt{\frac{\gamma m}{k_B}} \frac{b}{\sqrt{T} p} \quad (3.6)$$

with the adiabaticity parameter  $\gamma = c_p/c_v = (f + 2)/f$ , where  $f$  are the degrees of freedom of the gas particle. Equation 3.6 is only valid if the outside pressure is sufficiently lower than inside the reservoir. If the mean free path  $\Lambda$  is larger than the size of the pumped vacuum chamber it is ensured that we get an intense beam with a wide angular distribution [49].

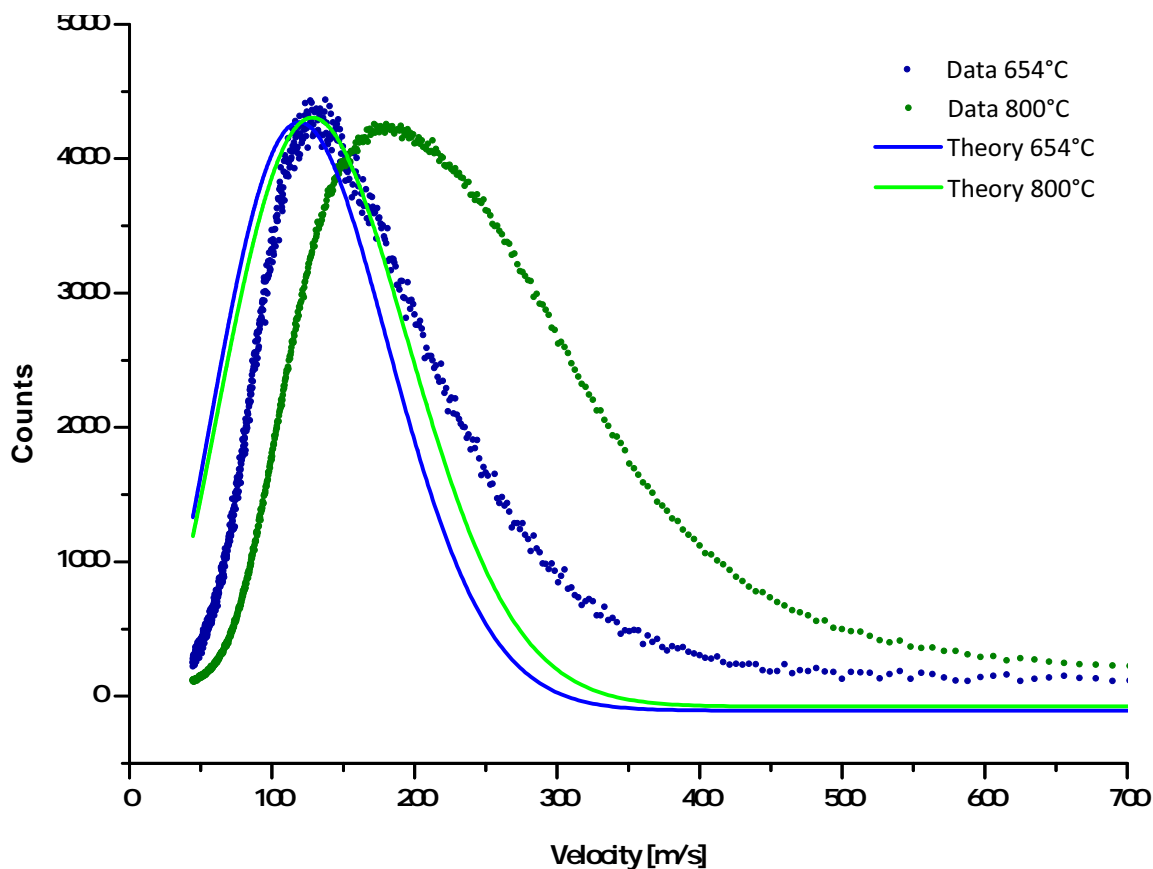


FIGURE 3.5: The velocity distribution of the molecules emerging from the source for two exemplary temperatures.

### 3.2.3 The Longitudinal Velocity Distribution of the Thermal Beam

In Figure 3.5 the measured velocity distribution of the molecules, emerging from the beam source is depicted. The furnace is equipped with a  $50 \mu\text{m} \times 2 \text{ mm}$  slit and heated to two exemplary temperatures, measured by thermocouples attached to the ceramic crucible. The background pressure is held at a level better than  $1 \cdot 10^{-6}$  mbar. An optical chopper about 30 cm further downstream from the source is rotating at a frequency  $\nu = 30$  Hz and sets the starting point of the measurement via a light barrier. The molecules fly a distance of 1 m freely until they are detected by a quadrupole mass spectrometer. Thus, the incoming molecular beam is ionized via electron impact and analyzed. The mass selective signal is recorded and plotted as a function of the arrival time with a high resolution of 1024 points. The time between two consecutive events is set to be  $2 \cdot 10^{-5}$  s.

<sup>8</sup>Named after the Danish physicist Martin Hans Christian Knudsen

<sup>9</sup> $\sigma_{\text{col}}$  denotes the collisional cross section of the molecules

We can clearly see the large discrepancy between theory and experiment for high temperatures. Consequently, theory predicts the most probable velocity only for low temperatures with admissible accuracy. Whereas the overall shape is still asymmetrical the distribution becomes very broad for high temperatures. This fact has severe influence on the gravitational velocity selection.

### 3.3 Velocity Selection

In order to achieve the goal of high contrast interference patterns, the preparation of longitudinal coherence is essential. Two waves are coherent if they have a constant relative phase to each other. The visibility of the interference pattern is a direct measure for the degree of coherence. Monochromatic Laser light has a very high ability to show interference due to the fact that it is perfectly correlated with itself for all delay times  $\delta\tau$ <sup>10</sup>. This is certainly not true for white light, which is a mixture of different frequencies and thus its phase varies quickly over time and position. Since there is no definite correlation for different times any interference vanishes when averaged.

In our experiment we are dealing with a thermal, effusive source where a broad velocity distribution of Maxwell-Boltzmann type is expected for the emerging particles (see section 3.2), similar to white light. Different velocities propagating through the interferometer lead to an averaging of different phases after the second grating that suppresses the formation of an interference pattern. In general, one can say that the larger the range of velocities (de Broglie wavelengths) the faster a wave decorrelates and loses its ability to show interference. Thus, there is a high demand for an efficient velocity selection scheme. In particular, two techniques have been developed by us for that purpose.

#### 3.3.1 Gravitational Velocity Selection

The first method is rather a separation technique than an efficient velocity selection scheme in the sense that the velocities that do not meet the resonance condition are actually removed from the beam. The simple effect of gravitation on massive objects is used for this simple technique. If a molecule leaves the furnace orifice with an initial velocity  $v_0$  and an angle of inclination  $\alpha$  gravitation  $g = 9.81 \text{ m/s}^2$  forces the particle to

---

<sup>10</sup>The phase of a wave  $\phi(t)$  is directly correlated to the time shifted copy of itself  $\phi(t + \delta\tau)$

follow a trajectory of parabolic shape. This can be seen if the horizontal and the vertical components of the initial velocity are separated.

$$z(t) = v_0 t \cos \alpha \quad (3.7)$$

$$y(t) = v_0 t \sin \alpha - \frac{g}{2} t^2 \quad (3.8)$$

Consequently, we express  $t$  as a function of  $z$  and plug it into  $y(t)$  to arrive at the parabolic trajectory

$$y(z) = z \tan \alpha - z^2 \frac{g}{2v_0^2 \cos^2 \alpha} + y_0 \quad (3.9)$$

If we now predefine this parabola by two points  $y_i(z_i)$  using spatial filters (slits) of different size which are separated by a distance  $z_1 = L_1$  from each other and  $z_2 = L_2$  from the surface, we directly see that different initial velocities  $v_0$  arrive at different points  $y_d$  at the detection surface. For the sake of simplicity the first slit ( $50 \mu\text{m} \times 2 \text{mm}$ ) is attached directly to the furnace and serves as the orifice. The second ( $20 \mu\text{m} \times 2 \text{mm}$ ) is mounted on a translation stage in the lithography chamber. Finally, the third point, which uniquely defines the parabola, is a definite area on the surface. This means that all the different velocities  $v_0$  arrive at the sample at different heights  $y_d(z)$ . The area which molecules of a certain velocity occupy, is defined by the proportion of the lengths between the slits to the slit openings ( $\approx 50 \mu\text{m}$ ). The choice of the slit openings is arranged such, that for sufficient signal we still expect a narrow velocity distribution  $\delta v/v \approx 0.08$  for a mean velocity of 100 m/s. Here the major drawback of this velocity scheme can be identified. Since all velocities from the Maxwell-Boltzmann distribution reach the sample surface the exact location of the appropriate velocity has to be determined. From Figure 3.6 we can further derive that the intensity varies for different falling heights of the molecules, since the velocity selection depends heavily on the velocity itself. Therefore one can estimate the position of the right velocity by relating the total number of molecules at a particular position on the sample surface to the maximum number. Thus the number of molecules per unit area as a function of the height on the sample gives a direct indication for the velocity distribution.

One has to identify the maximum number of molecules which can be done by scanning relatively small areas of about  $100 \times 100 \text{nm}^2$ . Subsequently the tip of the scanning tunneling microscope is moved to the estimated height on the sample and the scanning of large areas ( $2.25 \mu\text{m}^2$ ) with high resolution can be initiated to search for the quantum interference pattern. This method requires long scanning times on many sample positions. However, an eminent advantage is its simplicity. There are no moving parts that could

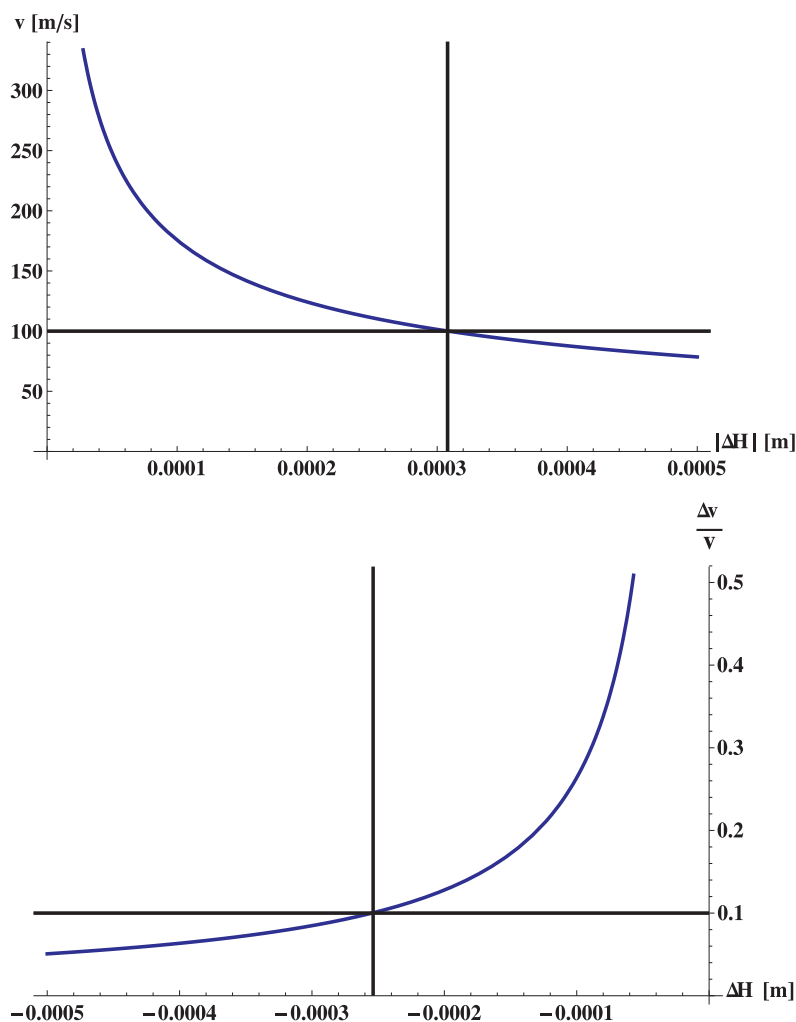


FIGURE 3.6: The gravitational velocity selection. The falling height of the molecules as a function of the longitudinal velocity on the left. The velocity selection critically depends on the velocity itself. Thus for varying heights on the sample one expects different velocity selection and therefore a changing number of molecules per unit area.

cause vibrational noise, or that could degrade the vacuum conditions.

### 3.3.2 Velocity Selection by a Rotating Helix

An ideal velocity selector provides a monochromatic beam of molecules with a high transmission rate without causing vibrational noise or affecting the prevailing vacuum conditions. To fulfill these requirements, different approaches have been considered. Nevertheless, the underlying principle remains the same for all. From Neutron optics this velocity selection scheme is known and well established [50]. A helical path rotates at constant angular velocity  $\omega$  about its symmetry axis. This helical path is determined by its pitch

$dL/d\phi \approx L/\phi_0$ . A straight-forward way to realize such a predefined path of width  $s$  is to mill it into a solid aluminium cylinder of length  $L$  and radius  $R$ . In order to define the pitch of the helix we equate the time of flight of a molecule with velocity  $v_0$  to the time the selector needs to turn by the angle  $\phi_0 = \omega t$ .

$$v_0 = \frac{L \cdot \omega}{\phi} \quad (3.10)$$

We shall now consider the influence of a helix with finite width on the transmitted velocity distribution. If a molecule with a velocity  $v = v_0 + \Delta v$  travels the distance  $L$  the rotor turns by the angle  $\phi_0 - \delta\phi$ , where  $0 \leq |\delta\phi| \leq \psi$  with  $\psi = s/R$  as the angular aperture of the helix to the incident beam. Thus, the width of the helically milled slots solely determines the width of the transmitted velocity distribution.

$$\sigma = \frac{\Delta v}{2v_0} = \frac{v_{max} - v_{min}}{v} = 2 \frac{\psi/\phi}{1 - \psi^2/\phi^2} \approx \frac{11}{\phi} \psi \quad (3.11)$$

In this equation  $v_{max}$  corresponds to the maximum allowed velocity for which the rotor turns by the angle  $\phi - \psi$ . The fraction  $T_0$  of the molecules that actually enter the slots of the velocity selector is simply determined by the opening fraction  $NR\psi/2\pi R$ . This ideal transmission function is only valid for the velocity  $v_0$  we want to select from the thermal beam. For the other velocities  $v$  the transmission function changes to

$$T(\Delta\phi) = T_0 \left( 1 - \frac{|\Delta\phi|}{\psi} \right) \quad (3.12)$$

Furthermore, the divergence of the beam may have influence on the performance of the presented velocity selector, especially on the transmission. If the velocity selector is illuminated by a beam of angular spread  $2\alpha_0$  an additional term appears in the transmission function 3.12. The transverse distance moved within the slot now depends on the velocity  $v$  and the displacement  $L\alpha$  where  $-\alpha_0 < \alpha < \alpha_0$ .

$$T(\Delta\phi, \alpha) = T_0 \left( 1 - \frac{\Delta\phi + (L/R)\alpha}{\psi} \right) \quad (3.13)$$

### The Design of the Velocity Selector

To determine the dimensions of the selector we start from the velocity we want to select. The gravitational velocity selection depends heavily on the actual velocity of the

<sup>11</sup>Here the Taylor-Series expansion  $\frac{x}{1-x^2} \approx x + x^3 + O(x^5)$  is used

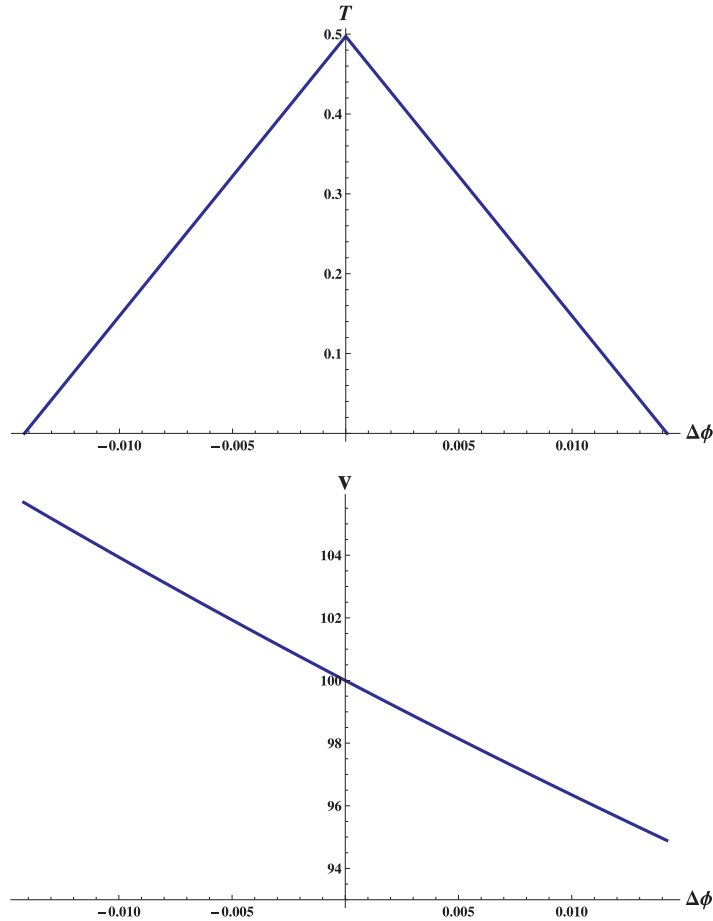


FIGURE 3.7: The normalized transmission function of the helical velocity selector 3.12 (top) and the transmitted velocity as a function of the effective slit width (bottom)

molecules. Thus, if it should be possible to test both selection methods in the same setup one must find a compromise between large signal and a narrow velocity distribution of the gravitational selection. The velocity distribution of the fullerenes has its maximum value about 180 m/s. But since the gravitational velocity yields a selection efficiency  $\sigma = 0.3$  this velocity class has to be excluded. A value, for which the gravitational selection yields acceptable results at adequate signal strength is 100 m/s.

As a second step the width of the resulting velocity distribution is fixed. A value which still yields a large signal with high contrast is  $\sigma \approx (v_{max} - v_{min})/2v_0 = 0.05$  where  $\sigma$  is the full width at the half of the maximal value of the transmitted distribution.

If we now fix the openings of the slots to the smallest value that can be manufactured with accurate precision to about 300  $\mu\text{m}$ ,  $\phi_0$  is defined and the only thing which can still be varied is the product  $\omega L$ . From 3.10 we can extract that this product has to satisfy the condition  $\omega \cdot L \cong 27$  for a given radius  $R = 0.022$  m which has been chosen in a way

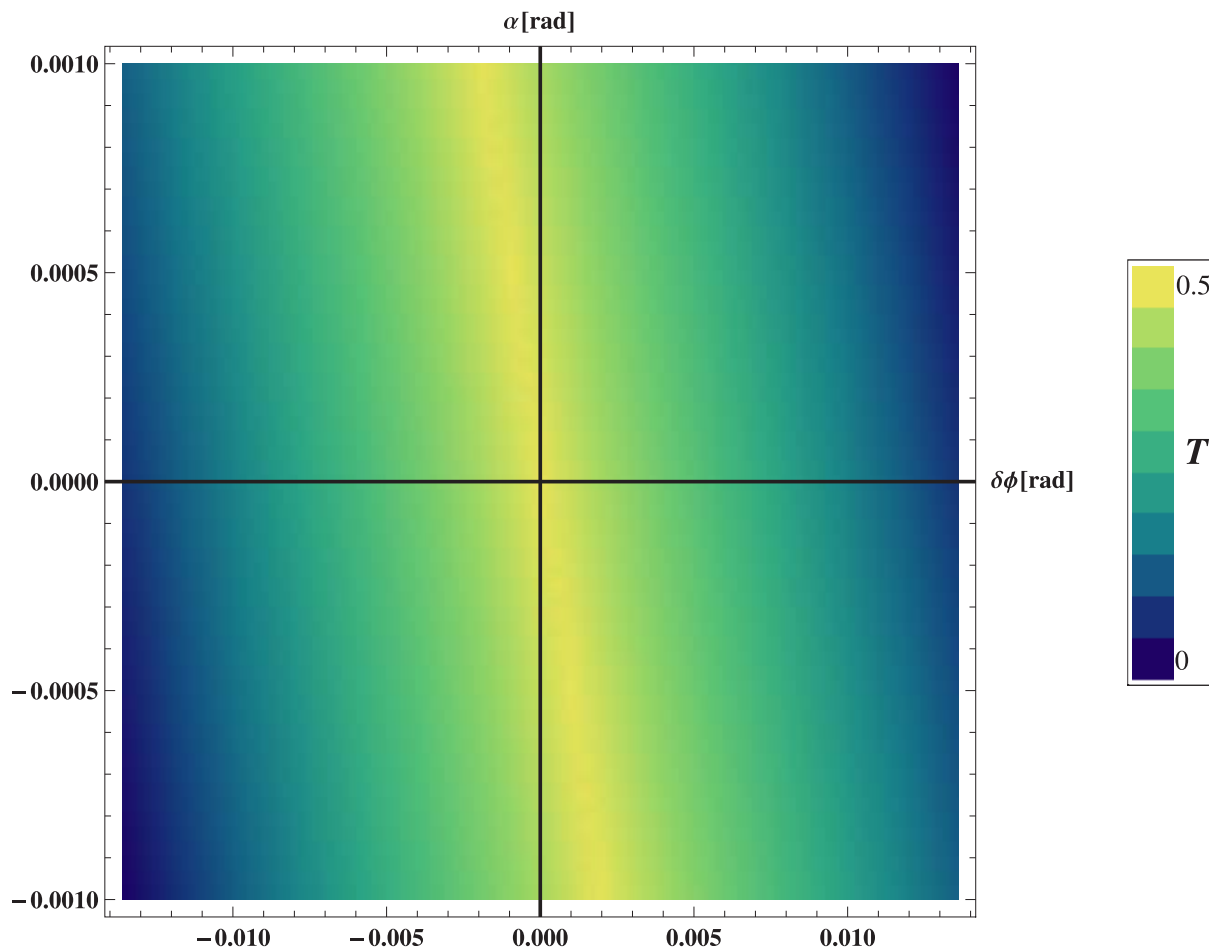


FIGURE 3.8: Molecular transmission 3.13 as a function of the effective slit width and the angular spread  $\alpha = 1$  mrad of the molecular beam.

that the selector can be mounted eccentrically on a CF100 flange so that the molecular beam still defines the central axis of the apparatus. The chosen radius leads to a total number of 220 slots with an elementary opening fraction of  $T_0 = 0.5$ . The inertial mass is minimized by using a hollow cup instead of a solid cylinder with a resulting mass of about 50 g. Further details are provided in the appendix A.

### 3.3.3 A High Resolution, Sideband-Free Slotted Disk Velocity Selector

If a resolution better than  $\sigma = 0.05$  is required, one encounters the limits of the helical setup. An alternative way to define a helical path for molecules is by an array of slotted disks which have a predefined angle with respect to each other. A schematic drawing of the selector is depicted in Figure 3.10. Slotted disks possess a very low inertial mass and

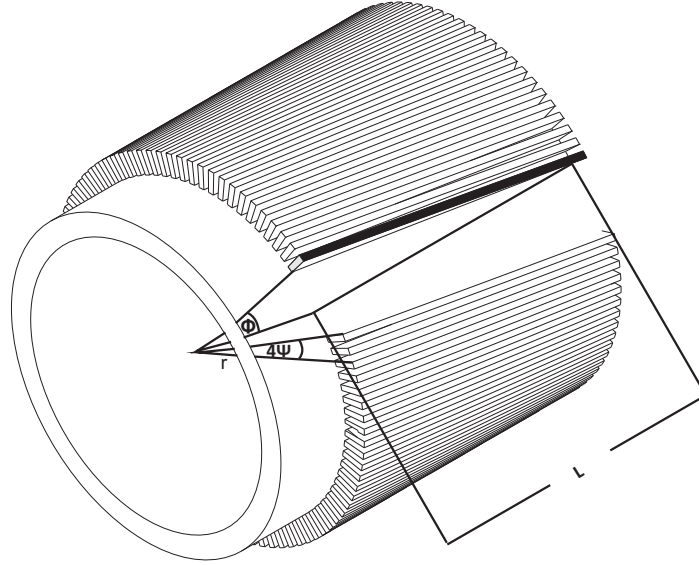


FIGURE 3.9: The helical velocity selector

thus can be accelerated to high angular speeds. Moreover, the slots can be accurately manufactured with an average width of 100  $\mu\text{m}$  and a length exceeding 3 cm using photolithographic etching techniques. Thus, we expect large throughput over a huge area, which facilitates the adjustment process described in section 3.8.4. Finally, the molecules with wrong velocity are effectively removed by collisions with the face of a disk rather than a thin slot wall [52] and the overall mass is dramatically reduced which results in a minimum vibration level. The theoretical description of this selector is in complete analogy to the one presented above, with the only difference, that the finite width of the disks plays a central role regarding the effective elimination of the velocity sidebands. The transmission function  $T$  is governed by the velocity distribution of the incoming beam  $f(v)$  which is of Maxwell-Boltzmann shape and the effective slit-width 3.12.

$$\frac{v_{max}}{L-d} = \frac{\omega}{\phi_0 - \psi} \quad (3.14)$$

$$\frac{v_{min}}{L+d} = \frac{\omega}{\phi_0 - \psi} \quad (3.15)$$

By introducing the geometrical parameters  $\beta = d/L$  and  $\gamma = s/r\phi_0$  we arrive at the simple expression for the resolution  $\sigma$  of the selector.

$$\sigma = \frac{v_{max} - v_{min}}{2v_0} \cong \gamma - \beta \quad (3.16)$$

If we now consider that within the allowed velocity range the distribution  $f(v) \approx v_0 = c$  can be assumed homogeneous for a given  $\omega$  and further regard  $\beta$  and  $\gamma$  small compared

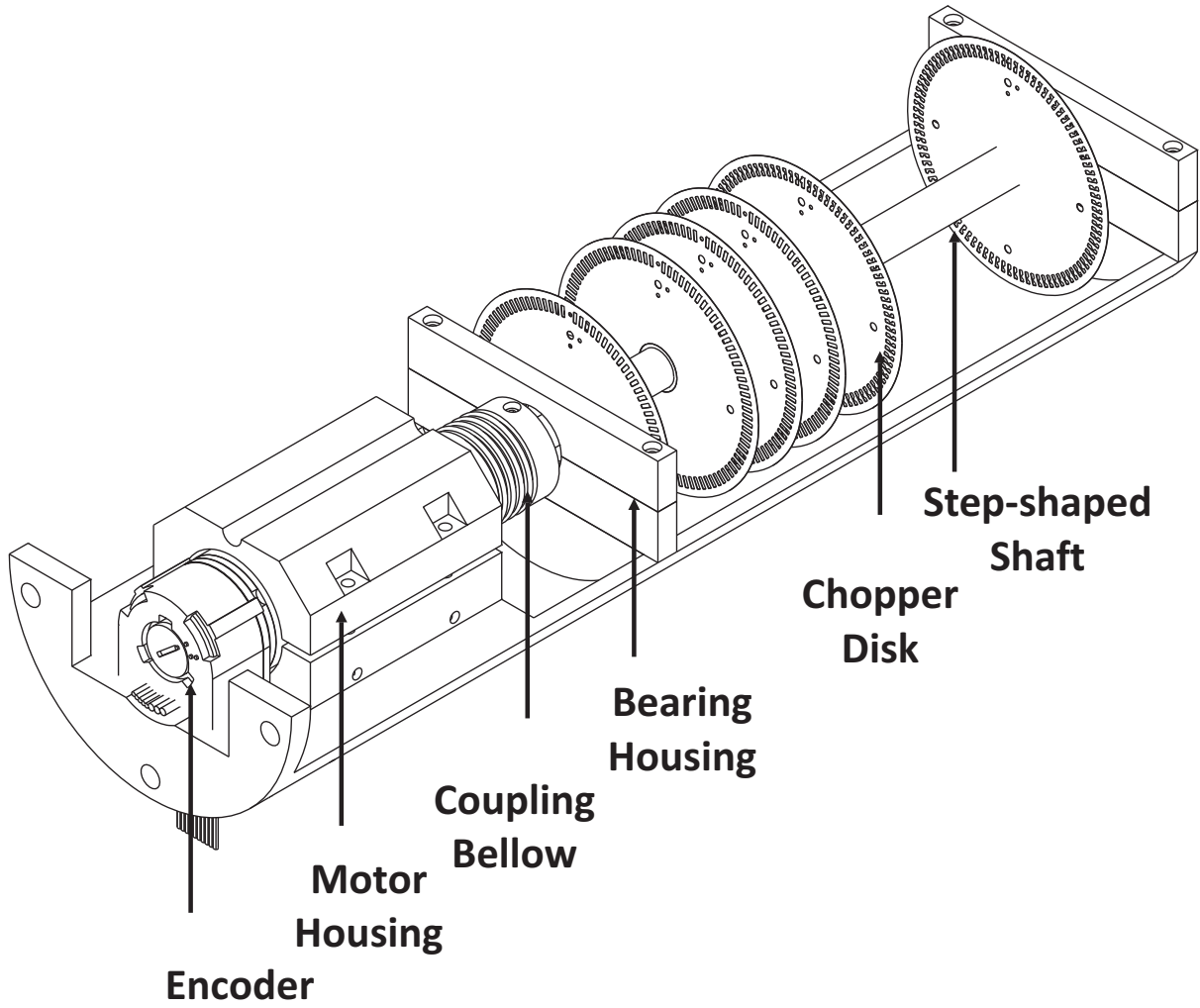


FIGURE 3.10: The design of a slotted disk selector. Since the slotted disks possess a definite angle in respect to each other, no velocity sidebands exist. Thus, only the aimed velocity passes the selector in contrast to the design presented in [51]

to unity the transmission  $T$  reads

$$T = Gv_0f(v_0) \quad \text{with} \quad G = T_0\gamma\left(\frac{1-\beta}{\gamma}\right) \quad (3.17)$$

If the molecular beam is directed onto the selector with a residual, tangential inclination  $\alpha$  due to misalignment, the transmission changes according to

$$T' = T(1 - 2\delta) \quad \text{with} \quad \delta = \frac{\alpha L}{r\phi} \quad (3.18)$$

From 3.18 we infer the need for a precise alignment technique which is subsequently described.

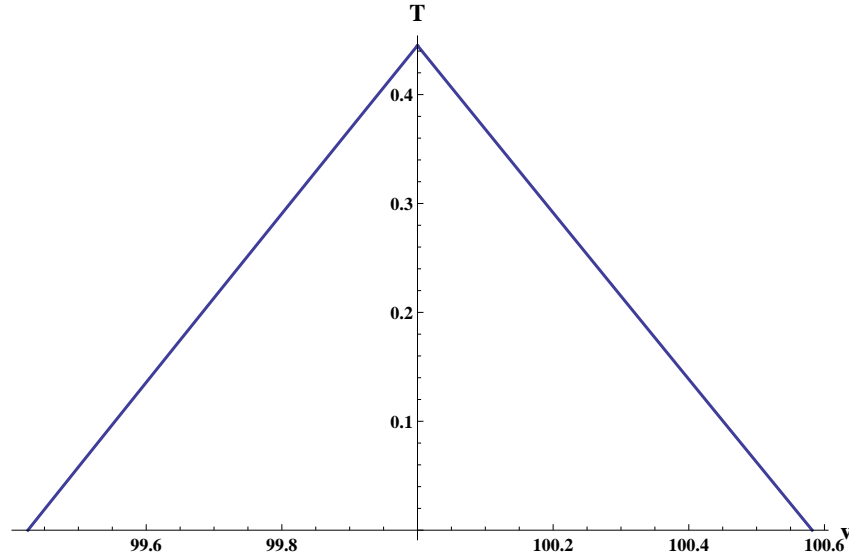


FIGURE 3.11: The Transmission function of the slotted disk selector

### The Design of the Velocity Selector

Particular preconditions must be met by considering the actual dimensions of the velocity selector. The housing should be compatible with an already existing helical velocity selector. Furthermore it was intended that it is in principle possible to push the resolution  $\sigma$  to a limit of 0.005 of the incoming velocity distribution. Finally the assembly should easily fit into a tube of 100 mm diameter and the slotted disks should be exchangeable in order to realize different selection scenarios. The technical drawings and concrete dimensions are provided in appendix B

Hence, the length  $L = 140$  mm is fixed and the diameter of the disks has been chosen to be 64 mm whereas the mean radius of the slits is set to be 28.5 mm with an opening angle  $\psi = 7.5$  mrad for the  $\sigma = 0.005$  solution. In order to achieve such a high resolution the rotary frequency has to be set to 150 Hz for a chosen velocity of 100 m/s. This corresponds to an angular displacement  $\phi_0 = 75.6^\circ$  between the first and the last disk. In order to diminish the influence of misalignment onto the residual vibration level the motor and bearing housings are prearranged with dowel pins which are positioned with the accuracy of a CNC milling machine. Moreover, the bearing housings are designed bipartite so that the shaft with the slotted disks can easily be exchanged. The disks are manufactured from 0.1 mm stainless steel. They are mounted onto a stainless steel shaft whose diameter changes over the length in such a way that the distance between the disks is mechanically predefined without introducing imbalances. The only thing one has to ensure is the radial alignment of the disks to each other. For this purpose the disk slits

are already manufactured with the requested angles to each other so that only the origins have to be superposed. This can easily be done by directing a laser beam through the drilled calibration holes which are also used to align the assembly and the molecular beam source to the central interferometer axis. Regarding the diameter of the disks it becomes obvious that the beam has to pass decentralized through the CF100 double cross source chamber. Hence the source chamber has to be lowered with respect to the interferometer chamber and the molecular beam source by a specific amount. This is done by means of two appropriate adapter flanges.

### 3.3.4 In-Vacuum Movement

For the desired mean velocity of 100 m/s the selector has to be accelerated to high rotational speeds. On the one hand it is of utmost importance to reduce the possibility of dephasing, due to lateral shifts of the gratings caused by vibrational noise of the rotating part. On the other hand, the vacuum conditions must not be spoiled by any grease or lubricants ordinary bearings rely on. Furthermore, UHV compatible, fast-spinning motors commercially available. Thus, one has two options: either one tries to improve available motors or the actuation component has to be completely transferred to the outside of the chamber.

Both ways have been investigated and realized. Since the helical velocity selector has a very low inertial mass it is possible to directly mount it onto a ferrofluid sealed, rotary vacuum feedthrough. These solid shaft feedthroughs provide excellent torque transmission at a very low leakage rate of  $< 10^{-11}$  mbar · l/s which allows to achieve base pressures of below  $10^{-8}$  mbar in the source chamber. Combined with the capability of transmitting very high rotational speeds (up to 15000 rpm) these feedthroughs serve as an ideal tool for accomplishing our demanding requirements.

Since there is no magnetic coupling, but rather a shaft directly put through the vacuum flange, effective sealing is necessary. This is realized by a ferrofluid held in position by a strong permanent magnet. This provides excellent in-phase rotation without any backlash.

The slotted disk selector, on the other hand is driven by a high precision brushless servomotor with special vacuum compatibly lubricated bearings. In order to improve the overall background pressure even further, all the rubber insulated cables are replaced and the black coating of the motor is removed. Two special ceramic hybrid bearings are

mounted onto the step shaped shaft of the disks. Ceramic ( $\text{Si}_3\text{N}_4$ ) balls in a stainless steel housing in combination with a dry lubricant ( $\text{WO}_2$ ) are necessary in order to assure unobstructed use in ultra high vacuum conditions. The very low production tolerance of ABEC7 associated with the increased stiffness of the ceramic balls represent excellent preconditions for a smooth and continuous operation.

One has to be very careful when mounting such high precision bearings onto the shaft. The shaft itself has to fulfill characteristic norms depending on the particular bearing and its use within the assembly. In cooperation with Professor Helmut Springer from the Vienna University of Technology a typical scenario has been realized, in which one side of the shaft has a small oversize of about  $0/+5\ \mu\text{m}$  and thus is axially fixed and the other side has a small undersize  $-2/-7\ \mu\text{m}$ . This saves the bearings from damages by thermal expansion of the shaft.

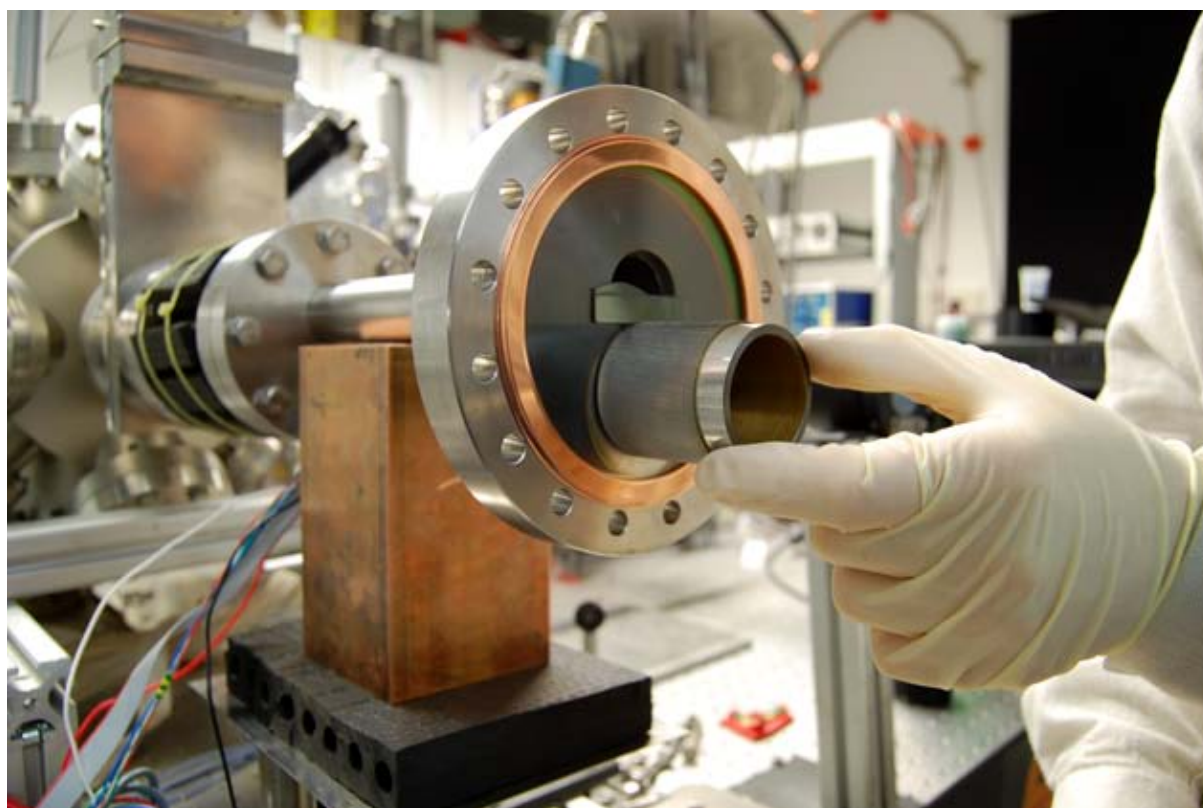


FIGURE 3.12: The velocity selector mounted on a vacuum flange. Molecules that leave the central axis and do not pass through the whole selector length are removed by a shield.

### 3.3.5 Comparing the Different Velocity Selection Schemes - A Summary

The major drawback of the gravitational selection theme lies in the fact that a huge variety of velocities reaches the sample surface. Hence, it requires enormous scanning effort to find the velocity which fulfills the resonance condition and yields an interferogram of high contrast. Apart from this deficiency, very small spatial filters have to be used (e.g.: 20  $\mu\text{m}$ ) in order to obtain the required velocity selection which have severe influence on the total number of transmitted molecules. These handicaps counterbalance the enormous advantage that it works in the absence of any moving parts which could cause vibrational dephasing. Moreover, the alignment procedure which is described in the following section, turns out to be simplified dramatically. Large effort has now been put into the development of alternative velocity selection schemes. These are mainly governed by the idea that only the desired velocity which fits to the defined Talbot length should enter the interferometer chamber. Two different methods were presented:

First the rotating helix which is milled into an aluminum cup and mounted onto a ferrofluid sealed rotation feedthrough. Here everything is mechanically predefined, but the alignment with respect to the interferometer axis remains a challenge that can be met with a sufficiently focused laser beam.

Second, if one desires to push the limits to extremely narrow distributions of  $< 0.01$ , then the slotted disk version is the sole choice. Due to the possibility of fabricating such tiny slots with high accuracy and the small weight of the disks it can be accelerated to high rotational speeds which results in its invincible resolution. Care must be taken when aligning the disks with each other, as this determines the actual resolution. However, if the average error remains small against the slit width, then its influence is negligible. We can easily reach this goal by using a focused laser beam and direct it through the defined calibration bores in the disks. From the previous sections it can be inferred that we get an almost monochromatic beam of molecules for the price of having to deal with vibrations and demanding technical challenges.

Every rotation which relies upon conventional bearings generates vibrations which must be coped with, so that the contrast of the interference pattern is not blurred out. This can be done by accurate balancing techniques and a precise fitting of the selector bore to the rotating shaft. Moreover, the use of a mechanical feedthrough offers great opportunities with respect to the improvement of the vacuum conditions and vibration isolation as well. The only part which stays inside the vacuum chamber is the rotating aluminum

cup. Hence, it is possible to adjust the coupling of the motor to the feedthrough in a way that only a minimal vibration level can reach the interferometer. Furthermore, if problems occur there is no need to vent the whole chamber. Everything is easily accessible from outside and thus represents a great improvement regarding the long term operation and stability of the velocity selector.

## 3.4 The Interferometer

The interferometer consists of two photolithographically etched silicon nitride gratings with a periodicity  $d = 257.4$  nm [53]. The opening fractions (ratio between slit-width to the periodicity of the grating) of 32.4% and 64% are chosen as a way to obtain large contrast  $> 70\%$  with a reasonable velocity selection scheme of  $\sigma = 0.05$ . The smaller one chooses the opening fraction of the first grating, the higher the expected visibility, but at the expense of a reduced number of transmitted molecules.

Furthermore, the opening fraction of the second grating determines the interaction strength of the molecules with the grating walls (van der Waals interaction) and thus has severe effects on the expected visibility. A small opening fraction yields a high, but very narrow visibility as a function of the longitudinal velocity which demands an exceptional control mechanism of the velocities entering the interferometer for opening fractions beneath 40%. A suitable compromise, permitting high visibility with a reasonable velocity selection, has been found for the above stated values.

When constructing an interferometer one has to ensure that specific preconditions are met. To prevent length variations due to thermal fluctuations the grating support is made of stainless steel and is mounted onto a stainless steel rail. The two gratings have to be aligned to each other with high accuracy. This is realized by designing a bipartite grating holder. Furthermore, the grating holder itself is fabricated in such a way that the gratings are not damaged by thermal expansion during the bake-out procedure. Thus uncomplicated adjustment of the gratings can be associated with high stability and the security that the gratings are not damaged due to temperature gradients.

### 3.4.1 The Adjustment Requirements

In total, ten degrees of freedom must be controlled very precisely in order to perform a successful experiment. Starting from the pitch, yaw and roll of both gratings coming to

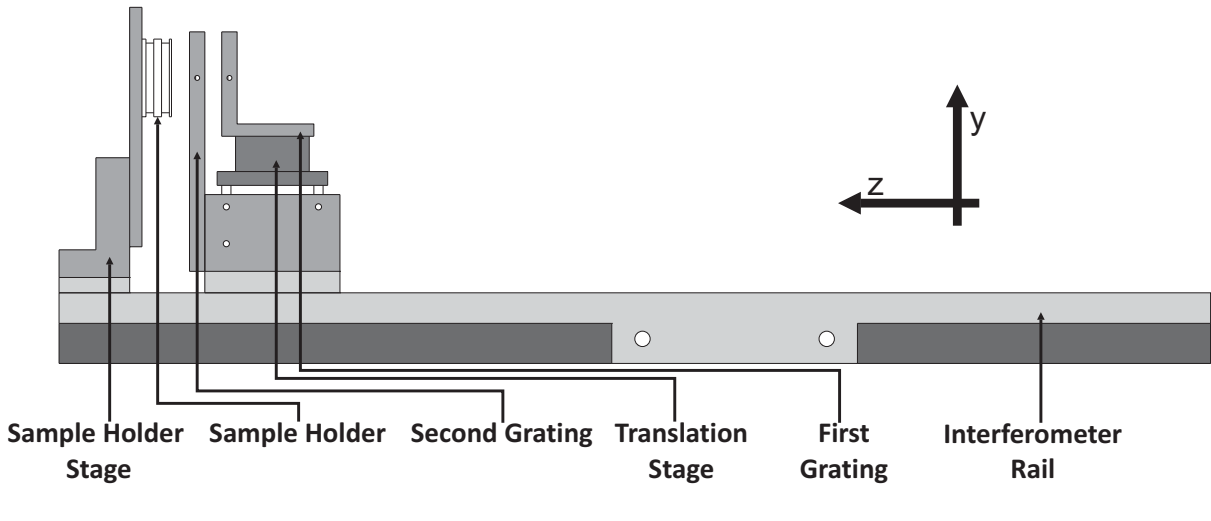


FIGURE 3.13: A schematic drawing of the interferometer

the length between the gratings and the detection surface arriving at the periodicity of both gratings. The necessity for a powerful adjustment technique can be seen.

### Length Scales

If all the imprecisions are regarded as independent in the first approximation, the periodicity of both gratings are considered equal and the setup is symmetrical, a bound for the adjustment precision can be found [23].

$$\frac{\delta L}{L} + 2\frac{\delta d}{d} < \frac{d}{4\pi\alpha L} \cong \frac{1}{N} \quad (3.19)$$

Where  $N$  denotes the number of slits illuminated at the first grating. Furthermore the factor  $4\pi$  enters due to the definition of the expected sinusoidal visibility. The variance of the grating constants has been measured by *Ibsen Photonics* to be equal within the  $\delta d = 0.01$  nm and thus can be neglected. So as to obtain a quantitative result for the adjustment precision  $\delta L$  of the distance between the gratings and the surface we insert the experimental values for  $\alpha = 1$  mrad,  $L = 12.5$  nm and  $d = 257.4$  nm. The angle  $\alpha$  is determined by the degree of transverse collimation defined by the experimental setup. It is basically defined by the lateral size of the source and a 1.5 mm *skimmer* between the source and interferometer chamber. The above stated condition then yields a maximally allowed length mismatch  $\delta L \approx 19$   $\mu\text{m}$  to get a visibility  $V > 0.9 \cdot V$ . The method on how to reach this requirements and the precision is given in section 3.4.4.

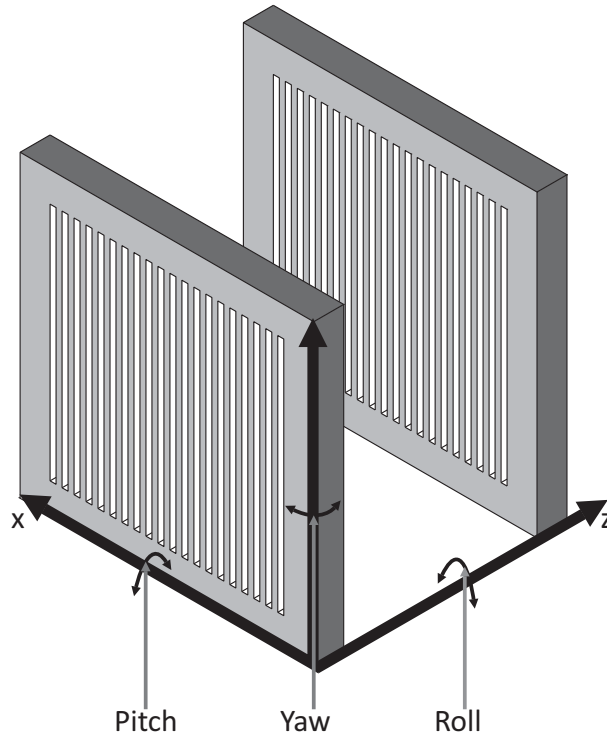


FIGURE 3.14: The definition of pitch, yaw and roll of the two diffraction gratings.

### 3.4.2 Yaw, Pitch of the Gratings

The yaw, pitch and roll of the gratings have various different influences on the expected visibility which shall now be discussed in detail. If one of the gratings is yawed about the central axis by the amount of  $\gamma$  a decreased opening fraction due to the finite grating thickness  $b = 160$  nm is one consequence. But this has minimal effect if the angle stays within reasonable amounts of several mrad and thus can be neglected. But a remaining yaw of a grating also induces a length mismatch between the two gratings of the amount

$$\delta L = 2\Delta \cdot \gamma \quad (3.20)$$

So if  $\delta L < 20$   $\mu\text{m}$ ,  $\gamma$  should not exceed 2 mrad if  $\Delta x \approx 6$  mm represents the maximum distance from the central axis of the grating (half of the grating diameter). The same relation holds for the pitch of a grating. Although the periodicity and the opening fraction is not affected, the distances change according to equation 3.20 and thus must not be neglected.

### 3.4.3 Roll

Basically there are three different ways the grating roll influences the quantum interference. First, if one grating is rolled with respect to the other, the grating constant deviates by a specific amount which has severe effects on the visibility. If we use 3.19 and assume  $\delta L = 0$ , an upper bound  $\phi_{max}$  for the roll of the second grating can be given with

$$\phi_{max} = \cos^{-1} \left( \frac{1}{1 + \frac{\delta d}{d}} \right) = \cos^{-1} \left( 1 - \frac{\delta d}{d} \right) \quad (3.21)$$

Secondly, if both gratings are parallel, but rolled with respect to the central axis of the interferometer the interference pattern appears rolled on the screen by the same amount, but without any loss of visibility. This is only true if gravity as a source of natural dephasing can be neglected. So if two interfering paths experience different gravitational potentials due to a slight angular mismatch  $\theta$  of the grating with respect to the direction of gravitation, the interference fringes shift according to [54]

$$\Delta x = g \sin \theta \frac{L^2}{v_z^2} \quad (3.22)$$

Due to the small size of our interferometer with  $L = 12.5$  mm,  $\Delta x \approx 1$  Å, if the total amount of the roll is of the order *unit*1mrad. Thus the influence of gravity can be neglected. Nevertheless one must stress that a shifted pattern does not effect the visibility directly. Since the lateral shift 3.22 depends on the longitudinal velocity, a finite velocity distribution leads to a diminishing visibility. But regarding the small lateral shifts of 3.22 and a width of the velocity distribution of  $\sigma = 0.05$  this effect can be neglected.

Finally, a grating roll introduces a phase shift which depends on the relative height at the gratings. Following [55] this phase shift reads

$$\phi = \frac{2\pi}{d} (\Delta x_1 - 2\Delta x_2) \quad (3.23)$$

Molecules passing the gratings at different heights  $y_i$  due to the grating roll experience different grating shifts  $\Delta x_i = \alpha_i y_i$  if grating  $i$  is rolled by the amount  $\alpha$ .

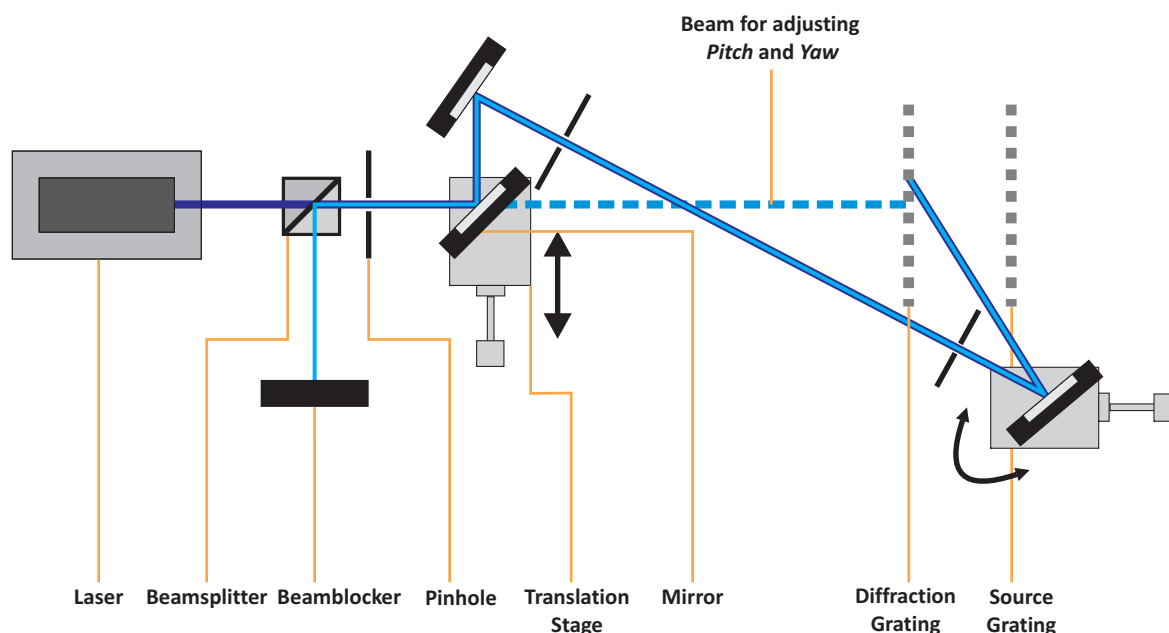


FIGURE 3.15: A schematic illustration of the alignment procedure. Pitch and yaw of the gratings are aligned by laser-backreflection. For the roll angle a Littrow adjustment scheme is realized.

### 3.4.4 The Alignment Procedure

In the previous section the alignment requirements were introduced which serve as the framework for the now presented approach to position the gratings in an appropriate way. The whole procedure is done in air with the rail carrying the interferometer fixed to the optical table. The angle of the rail with respect to the table has been checked and adapted by measuring the exact distance from the table's edge. Furthermore, the inclination with respect to gravity has been verified and compared with the inclination of the rail mounted in the vacuum chamber.

Then a *Coherent* laser diode module, emitting light at  $405 \pm 5$  nm with a maximum output power of 50 mW a typical spot size of 1.4 mm and a divergence of 0.4 mrad is fixed in a distance of 6 m to guarantee high accuracy.

In a first step the laser beam is directed through two pinholes of the same height in order to assure the orthogonality of the laser beam to the direction of the gravitational center. Then a mirror is put onto the sample stage to check the tangential angle of the sample stage with respect to the mounting rail. Now, that it is made certain that the laser beam passes straight through the sample stage, the length gauge *Heidenhain CT 6002* with a system accuracy of  $0.1 \mu\text{m}$  is positioned by the use of a YZ translation stage. The

angles of the stages, which crucially influence the measured length have been surveyed using a water balance with an accuracy of  $< 1$  mrad and of the length gauge with the backreflection from a mirror held onto the measuring plunger. Thus, one can be sure that the measured length is not distorted by an angle between the length gauge and the central interferometer axis.

Then a stainless steel calibration sample is inserted into the sample stage and the length gauge is set to its origin. In addition to this the height of the three real samples has been measured in relation to the steel sample. This is necessary to ensure that no mistake is made when measuring the samples outside in another sample stage. The second grating, already carefully fixed in its rotatable frame with stainless steel springs, was mounted into the frame holder which is designed in a way that an independent adjustment of roll, yaw and pitch is feasible. Yaw and pitch can easily be arranged in the right way by directing the partially reflected laser beam back onto itself. Since this is realized with an angular resolution of 0.16 mrad the requirements stated above can easily be met.

### **Roll - The Littrow Adjustment Scheme**

A slightly more sophisticated technique is required for the adjustment of the roll angle. A removable mirror is put into the beam path which directs the laser onto another mirror which is mounted on a linear translation stage so that both gratings can be illuminated in the same run. Due to the fact that the grating constant is smaller than the wavelength of the laser it is not possible to dissolve the grating structure and use the diffraction pattern to adjust the roll of the grating. However, if the laser beam hits the grating at a specific angle  $\theta_l$  in the XZ plane the first diffraction order is reflected back into the diode if the grating roll diminishes to zero. The diffraction condition in this so called Littrow arrangement is

$$\sin \theta_l = \frac{d}{2\lambda} \quad (3.24)$$

The crucial difference to the usual diffraction condition is the factor two in the denominator which appears due to reflection. The necessary path difference for constructive interference is twice the one of the transmission.

But before we start with the alignment of the angle one has again to be sure that the laser beam itself is perpendicular to the direction of the earths gravity field vector, by means of a water balance and two pinholes of the same height. Furthermore, this can be checked by arranging the beam which is directly reflected on to the grating surface with the first diffraction order in line with a water balance horizontally mounted onto a tripod. This is done accurately for both gratings.

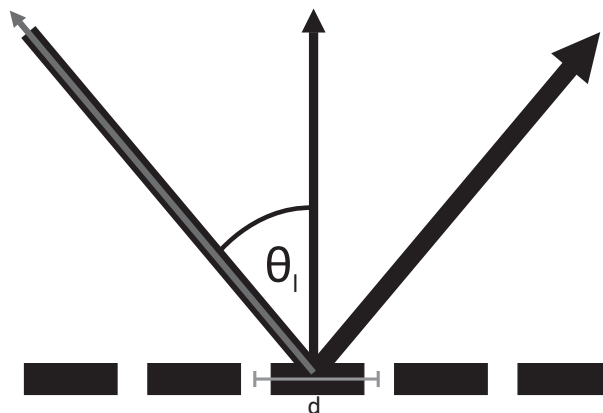


FIGURE 3.16: The Littrow adjustment scheme. If a Laser hits a diffraction grating with particular inclination of in the XZ plane the grating constant  $d$  appears larger. Thus it is possible to get diffraction and the first order is reflected back into the laser beam if the angle fulfils the Littrow condition 3.24.

In addition to that the interferometer is fixed onto a computer controlled, motorized, rotational stage in order to qualitatively check the grating constant which can be verified with an accuracy of  $257.4 \pm 0.2$  nm. The precision is limited owing to the restricted bidirectional repeatability of the rotational stage due to a finite backlash of  $0.03^\circ$ .

### Length Scales

One has to be very careful when measuring the distances of the gratings with respect to the steel sample. Due to their fragility, it is only possible to measure the distance between the grating's silicon wafer frames. Thus the thickness  $b = 390$   $\mu\text{m}$  of the wafer must be considered when adjusting the lengths. After the distance of the second grating with respect to the calibration sample is fixed the first grating is placed on an UHV compatible, linear, horizontal stepper positioner with nanometer resolution. Pitch and yaw are aligned with the adjustment screws of the table which holds the positioner and the roll angle with the rotatable grating holder. Subsequent to the angle adjustment, the stepper motor is positioned to its absolute zero and the distance with respect to the second grating is registered. The implementation of a linear positioner is necessary due to the fact that the samples differ slightly in height, typically by  $50 - 100$   $\mu\text{m}$ , so that the length between the first and the second grating has to be adjusted accordingly. The actual height of the samples with respect to the steel calibration sample is therefore measured outside with the *Heidenhain* length gauge.

## 3.5 The Detection Scheme

The main disadvantage of the existing Talbot-Lau interferometers is their dependence on the ionization of the molecules by high power lasers, or by electron bombardment. Especially as the mass and complexity increases, effective ionization is not guaranteed [56]. Hence a universal detection scheme with an efficiency close to unity, as presented here, represents a major step to overcome these limiting effects. It is the nature of this detection method that it may be easily scaled to larger molecular species. As the first step towards establishing this new method as a general detection scheme, the choice was made to use a scanning tunneling microscope in order to read out the recorded interference pattern, due to its unsurpassed resolution. Although the surface has to be conductive in order to use STM, this can be overcome by atomic force microscopy (AFM) which measures ultrasmall forces between the sample surface and an AFM tip. AFM is also implemented in our experiment, but has not been used so far because of the superior resolution of STM. As a first step, a detailed description of the detection surface and its preparation is given, succeeded by a brief introduction to scanning tunneling microscopy and its application.

## 3.6 The Detection Surface

A major ingredient for the realization of this detection method is the preparation of a surface which is atomically flat over large areas, combined with the capability of immobilizing the deposited molecules. A clean semiconductor surface turned out to be a promising candidate - the Si(111)-7x7 reconstructed surface.

Ordinary silicon with its diamond like face centered cubic lattice is cleaved along the (111) surface. A special heating procedure which is presented in section 3.8.1 results in the 7x7 reconstruction which took surface scientist over 25 years to determine it. It was Gerd Binnig and his co-workers [57] who resolved the structure in real space for the first time with their previously developed scanning tunneling microscopy technique [58].

This discovery marked the breakthrough of this new powerful technique. However, it took until 1985, that Takayanagi and his co-workers proposed their dimer-adatom-stacking-fault model which finally solved the problem accurately [59]. According to this model, the reconstruction consists of dimers along the sides of triangular subunits of the unitcell, a stacking fault layer and twelve adatoms at the top layer of the surface which locally form a 2x2 structure. Furthermore, a vacancy is formed at each corner of the 7x7 unit cell

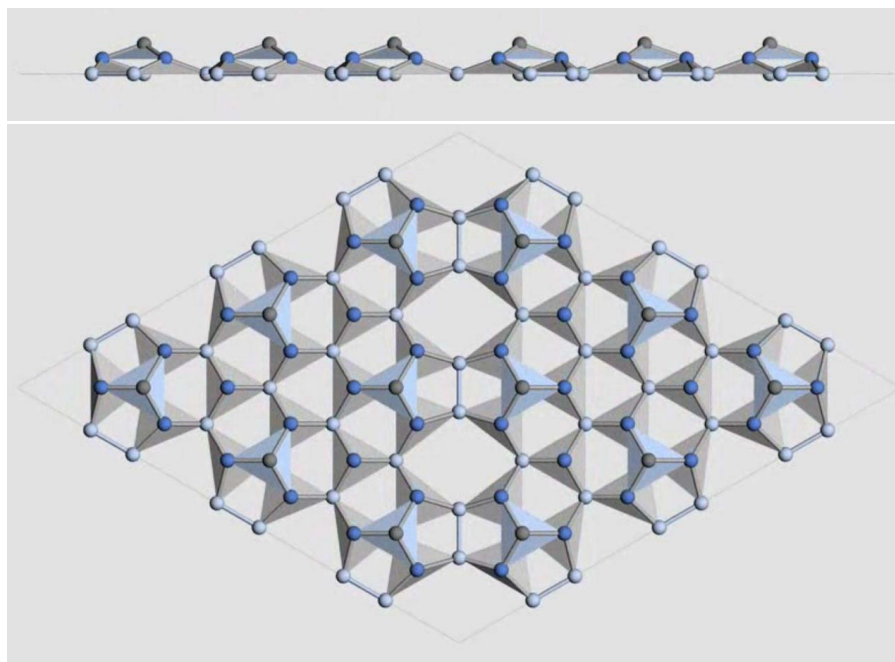


FIGURE 3.17: A schematic drawing of the Si(111)-7x7 surface. A side view on the top and the top view beneath.

which additionally contains 19 dangling bonds (broken covalent bonds). These dangling bonds are the main reason that adsorbed molecules do not diffuse, but rather form strong bonds comparable to the van der Waals forces between the molecules of the  $C_{60}$  solid [60–62]. On other surfaces like Au(111) or GaAs(110) [63] fullerenes migrate and form islands. Thus, the high density of dangling bonds on the Si(111)-7x7 surface suppresses the surface mobility of the  $C_{60}$  molecules effectively, which is a key requirement for our detection scheme.

### 3.7 Scanning Tunneling Microscopy - STM

The invention of the scanning tunneling microscope by Gerd Binnig and Heinrich Rohrer in 1982 [58] heralded a new age of nanotechnology. For the first time it was possible to obtain three dimensional images of solid surfaces with atomic resolution. The importance of this new technique was immediately recognized and led to the award of the Nobel Prize in 1986 for the inventors. While the pure imaging capabilities dominated the early years, the physics and chemistry of the probe-sample interactions opened completely new fields of interest and have become a major driving force for nanoscale science and technology.

### 3.7.1 The Basic Principle

Tunneling through potential barriers is a typical example of the wave-like behavior of particles. In quantum mechanics, a particle with a kinetic energy that is smaller than the height of a barrier potential is capable of penetrating this barrier. Thus, if the barrier is sufficiently narrow and low, a certain probability exists that the particle will *tunnel* through.

Tunneling plays a major role in nature and was observed for the first time by Julius Lilienfeld in 1922 [64] who dealt with field emission from metals. Whereas the theoretical explanation of the effect using tunneling through a potential barrier was given by Fowler and Nordheim in 1928 [65].

The basic concept of tunneling can be theoretically described by using the time independent Schrödinger equation with a one dimensional rectangular potential barrier, utilizing the wave-matching method. Since this can be found in every standard Quantum Mechanics textbook only the results are presented here. The transmission probability  $T$  for an impinging electron with energy  $E$  and mass  $m$  on a potential barrier of height  $V_0$  and width  $s$  is

$$T = \frac{1}{1 + \frac{(k^2 + \kappa^2)^2}{4k^2\kappa^2} \sinh^2(\kappa s)} \quad (3.25)$$

If the potential barrier is strongly attenuating which is the case for  $\kappa s \gg 1$  equation 3.25 simplifies to

$$T \approx \frac{16k^2\kappa^2}{(k^2 + \kappa^2)^2} \cdot e^{-2\kappa s} \quad (3.26)$$

with the decay rate

$$\kappa = \frac{1}{\hbar} \sqrt{2m(V_0 - E)} \quad (3.27)$$

The extraordinary spatial resolution of STM rests upon the strong exponential dependence of  $T$  on the barrier width  $s$ . In STM a bias voltage is applied between a sharp metal probe tip and the conducting sample. If the tip is brought into close vicinity to the sample surface (typically to about 0.3 – 1 nm) the applied potential difference of 0.1 – 2 V leads to a current of 0.1 – 1 nA, due to the above presented quantum mechanical tunneling effect. By scanning the tip over the surface while keeping the tunneling current constant (adjusting the vertical position respectively by means of a feedback loop) a topographical image of the sample surface is created.

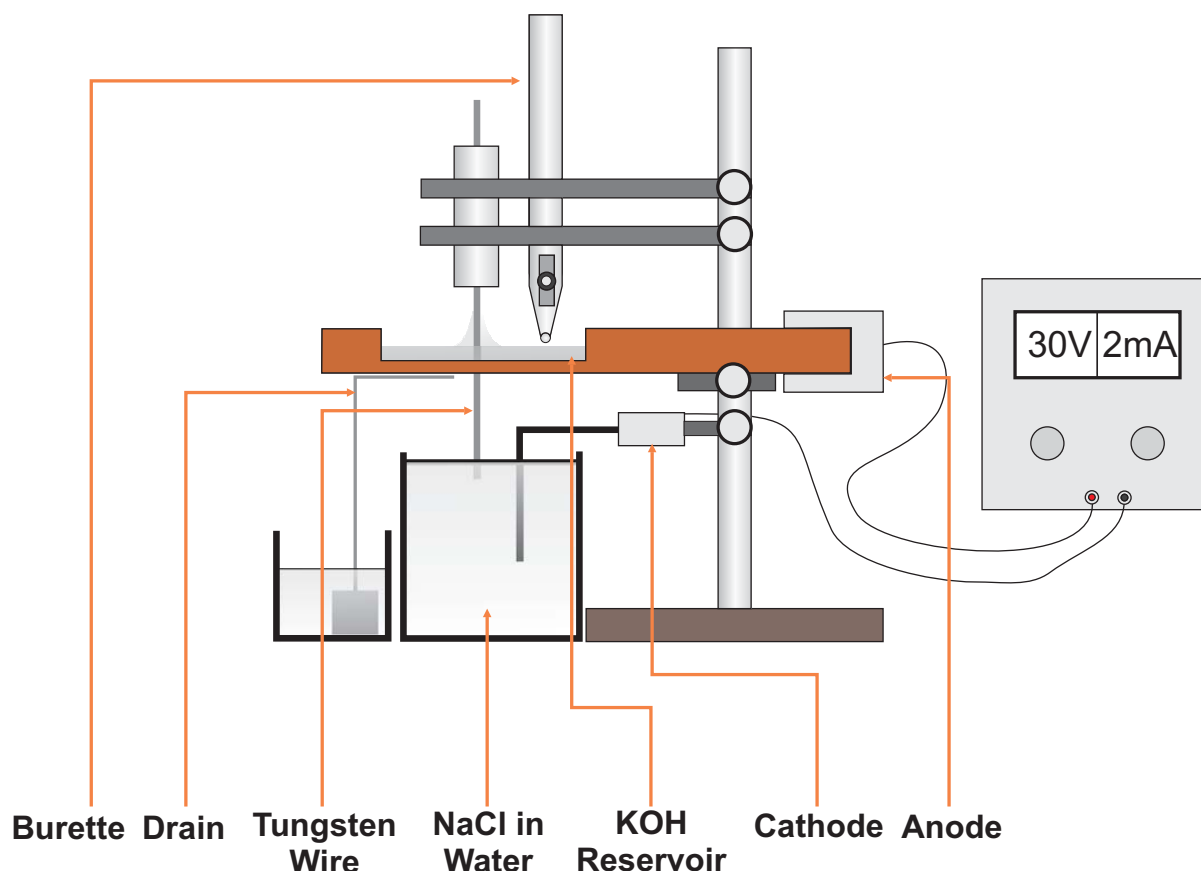


FIGURE 3.18: The tip preparation process. Tungsten wire is electrochemically etched with potassium hydroxide. This well established technique yields sharp and geometrical stable tips.

### 3.7.2 Tip Preparation

From the previous section it can be seen that the tip properties greatly determine the performance of the experiment carried out. Typically the nature of the sample surface being investigated and the scanning environment affect the choice of the tip material and its production method. In particular, two materials gained popularity within the STM community. First, tungsten which is limited to ultra high vacuum conditions due to the fact that it builds up an insulating oxide layer under ambient conditions. It is very hard and resists damage during tip-sample contacts. Controlled contact of sample and tip can be used to sharpen the tip even further. For imaging under ambient conditions, a chemically inert material should be chosen. Tips fabricated from platinum wire alloyed with iridium in order to increase its stiffness provide high performance. However, due to their geometry these tips still remain fragile. Thus, even boron doped diamond tips have been investigated to achieve reproducible, stable tips with high resolution [66]. Numerous methods exist to fabricate sharp metal tips for STM. But the most common

ones are mechanical procedures such as grinding or cutting and electrochemically etching. In contrast to mechanically cut metal wire, electrochemically etched STM tips yield reproducible and desirable results. Hence, this method is preferred and now described in detail. A schematic drawing of our etching station is depicted in Figure 3.18.

Although the results of the etching process are promising, it is well known that the use of ordinary cold drawn wire leads to instabilities during the scanning process [67]. Since we have to scan large areas of  $1.5 \times 1.5 \mu\text{m}^2$  the stability of the tip is of utmost importance. The use of single crystal tungsten wire is known [68–72] to yield sharp tips that have a well-defined shape and are mechanically stable. But since single crystal tungsten wire is about 10000 times more expensive than ordinary wire the following method has been implemented in our lab [67]:

Deformed metals can be recrystallized by heating them to sufficiently high temperatures so that diffusion takes place and the defect density is reduced [73]. A straight forward way to heat tungsten wire (0.25 mm in diameter and 1 m long) to high temperatures is by passing current through it. The sample, 99.99% pure tungsten wire, is fixed onto a vacuum flange and loaded with a small weight so that it stays under tension. The sample is annealed using a current of 7 A for about 30 minutes in vacuum ( $1 \cdot 10^{-4}$  mbar). After the tungsten wire has cooled to ambient temperature the actual etching procedure is initiated.

The wire is put through a thin membrane of 5% KOH into a sodium chloride solution. The potassium hydroxide serves as the cathode and is contacted via a copper plate to the DC voltage supply. The graphite anode is put directly into the sodium chloride solution and thus contacts the tungsten wire indirectly via the electrolyte.

It is crucial at this point to mention that a continuous flow of the potassium hydroxide is necessary for a satisfying result. One must ensure that, on the one hand, the flux is slow enough that the etching membrane is undisturbed, but, on the other hand the current remains constantly at a level of about 2 mA for the first five minutes. This is realized by the use of a buret made of acrylic glass and a draining facility at the bottom side of the copper plate. Compared to other etching methods where the tip is directly put into a basin of potassium hydroxide this setup has two main advantages: firstly, no elaborated switch-off electronics are needed to prevent blunting of the tip due to excessive etching after the wire has broken off. Because the mere breaking of the wire causes the disruption of the electric circuit and stops the etching process at exactly the right moment. Secondly, disturbance of the etching process at the anode due to emerging  $H_2$  gas is prevented a

priori. After the tip geometry is inspected with an optical stereo light microscope it is mounted into the tip holder.

The length of the tip with respect to the tip holder must not exceed  $1.7 \pm 0.1$  mm because the axial travel of the STM head is limited. The tip is now ready to be transferred into the vacuum apparatus.

Since Tungsten is not a very noble metal an insulating oxide layer is created which must be removed to achieve a good tunneling junction. This can be effectively done in the ultra high vacuum analysis chamber. By passing a current of 1 A, the built in tantalum filament is heated and emits electrons. The electrons are accelerated and directed onto the tip by a potential difference of about +100 V between tip and filament. Thus the tip is locally heated at a current of  $0.1 \mu\text{A}$  which is enough to sublime the  $\text{WO}_2$  layer that enfolds the tungsten tip.

The combination of recrystallization with the directed heating of the tip in UHV conditions leads to phenomenally sharp tips that provide atomic resolution. Furthermore, the lifetime is dramatically increased. Before the invention of the recrystallization procedure and the directed, controlled heating, it was impossible to use a tip for longer than a few days. Now, a single tip can be used for months with superior stability during the scanning process of large areas, not to mention the time that is saved by preparing the etching process and the transfer of the tip holders into and out of the UHV chamber.

### **3.8 The Experimental Procedure - A Chronology**

The vacuum system is prepared and the experimental preconditions for the source, velocity selector and detection scheme are known and have been accomplished using the methods already presented. Besides, the scanning tunneling microscope is equipped with a sharp tungsten tip and is ready to be used. Thus, we can approach the real experimental situation. Each distinct step is now presented, in order to provide a detailed and comprehensive picture of the experimental procedure. This will serve as a guiding framework to explain the experimental subtleties of which one must be conscious when matter wave interferometry is associated with scanning probe microscopy and surface science.

### 3.8.1 Sample Preparation

The sample preparation usually marks the starting point for a new experiment. Commercial, doped silicon wafers cut into the right dimensions of the sample holder must be prepared in a particular way so that the preconditions are met. The preparation of a reconstructed Si(111)-7x7 surface is now a well known and established technique. First, the wafers are cleaned ultrasonically in methanol to remove dust particles. As a second step, the wafer is carefully mounted into the sample holder where it is of absolute importance that the sample does not get into contact with any metal so that surface impurities could influence the nucleation and growth behavior of the reconstruction.

After the sample has been successfully mounted into the holder, the angles of the sample with respect to the optical table is measured and adjusted by using the reflection of a laser beam from the sample surface. This is necessary so that the length between the second grating and the surface is not distorted and remains indifferent for each point on the surface. Previously, the angle of the laser beam was calibrated by the partial reflection at the glass surface on which the sample is placed. With this method the pitch and yaw angles of the sample can be measured with an accuracy of 0.5 mrad.

In addition to that, the actual sample height has to be accurately measured so that the distance between the first and the second grating can be adjusted respectively. The above mentioned high precision length gauge is mounted into a special stainless steel holder. This configuration for determining the height of the sample must be calibrated in order to ensure that the sample height measured during the adjustment of the interferometer equals the sample height measured outside. Consequently, the height difference of all

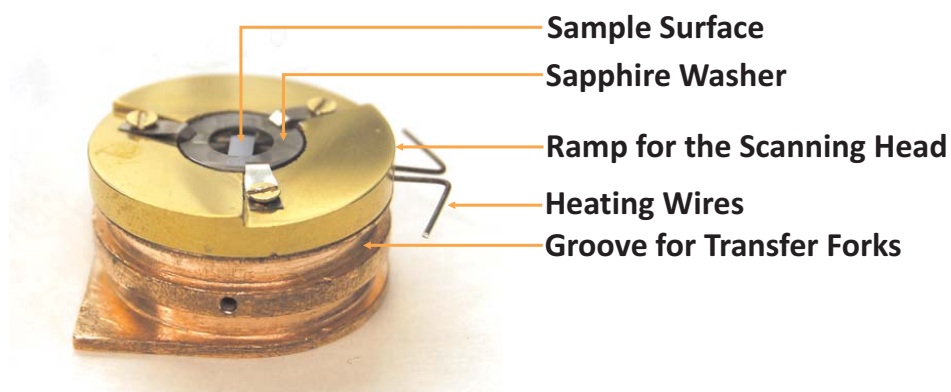


FIGURE 3.19: The sample holder is equipped with a silicon surface. The preparation of the reconstructed surface is realized by heating the sample resistively via the heating wires that contact the sample through tantalum pads.

samples with respect to the steel calibration sample has been measured and recorded during the adjustment of the interferometer. Then the length gauge has been mounted into its measurement stage, where the angle of the gauge is adjusted in a way that the determined length corresponds to the one measured during the adjustment of the interferometer.

After the conductance of the sample has been checked by measuring the resistance at the heating contacts (should not exceed  $10 \Omega$ ) of the sample the transfer chamber is vented. Moreover, the silicon sample must not have electrical contact to its holder. This is very important because only then is uniform heating guaranteed.

Subsequently the sample is put into the fork of the wobble stick inside the transfer chamber which is then pumped to a pressure of about  $1 \cdot 10^{-7}$  mbar. By passing a current of 1.5 A through the sample it is resistively heated to about  $600 \text{ }^\circ\text{C}$  for about an hour.

After this procedure the sample is transferred into the analysis chamber for further treatment. Fixed onto the sample stage, the computer controlled reconstruction procedure is initiated. Usually the sample is degassed at a temperature of  $600 \text{ }^\circ\text{C}$  for a period of twelve hours under UHV conditions, before the actual reconstruction procedure starts. The heating current is then gradually increased by 0.2 A while the temperature and the pressure are continuously monitored. The boundaries are set in a way that the pressure must not exceed  $1 \cdot 10^{-9}$  mbar for a particular set point. If it does, the step is repeated until the requested condition is satisfied. If the target set point of  $1220 \text{ }^\circ\text{C}$  is reached without transcending the limiting current of 5 A the sample is gradually cooled to ambient temperature. Within two minutes to about  $950 \text{ }^\circ\text{C}$  and to room temperature with a rate of approximately 8 K/min. At a temperature of  $860 \text{ }^\circ\text{C}$  the surface structure transforms from the  $1 \times 1$  unit cell to the  $7 \times 7$  structure [74] and thus this temperature range has to be passed very slowly. The complete procedure is now fully automated and incorporated to a *LabView* program. This is usually initiated on the day before the actual experiment takes place and yields very satisfying results. Since everything is done automatically and computer controlled during the night, the sample preparation time is effectively reduced by more than half a day.

### 3.8.2 Source Preparation

Usually on the same day as the preparation of the sample, the furnace is refilled with the desired molecules. In our case this is commercially available, sublimed  $\text{C}_{60}$  of high purity

(99.99%) from *MER* which is available as black crystalline powder.

This powder is filled into the ceramic crucible of the furnace to about two third of its capacity. The crucible is sealed with a ceramic cap with a central aperture of 1 mm in diameter. Depending on the velocity selection scheme, different apertures must be used. On the one hand, a  $0.05 \times 2 \text{ mm}^2$  spatial filter is used for the gravitational selection, on the other hand a pinhole with 0.25 mm in diameter is fixed on the furnace when the helical selection is applied. For the gravitational selection the two spatial filters should be aligned to the same horizontal plane with respect to gravity, otherwise the remaining angle between the slits leads to a larger effective opening which has negative effects on the velocity selection. Therefore, the furnace is fixed in a horizontal plane with respect to gravity using a water balance whereas the spatial filter is then adjusted by the same means. Thus, the orientation of the flange and the spatial filter are directly related to each other. Furthermore, the angle of the spatial filter can be adjusted by a rotatable flange outside. When everything is firmly fixed and the resistance of the heating wire is verified to be  $140 \Omega$  the furnace can be mounted into the vacuum chamber. When the pressure has reached a level of  $1 \cdot 10^{-6}$  mbar the furnace is heated to a temperature of  $300 \text{ }^\circ\text{C}$  to degas the fullerene powder so that potentially present solvents are removed. Furthermore, the heat improves the vacuum conditions so that after one night a base pressure of  $3 \cdot 10^{-8}$  mbar is reached.

### 3.8.3 Scanning the Sample Surface

Before the surface is transferred into the interferometer chamber the quality of the reconstruction is examined with the scanning tunneling microscope. Information about the tip condition can be gained and if required the tip is thermally treated by electron bombardment. Before any scan process, the turbomolecular pump adjoint to the transfer chamber is switched off to improve mechanical stability.

A good tip yields sharp images of the reconstructed surface with atomic resolution. An exemplary image is shown for both, positive and negative bias voltage, respectively in Figure 3.20 Since the bias is applied to the sample surface, electrons tunnel from the tip into the sample when the bias is positive and for negative bias vice versa. The twelve silicon adatoms per unit cell can be seen very clearly. The triangular subcells are highlighted when a negative bias is applied to the surface. Furthermore, one can see a slight height difference between the two subcells due to the particular electronic structure of the silicon surface. From this one can infer that not a real topographic image is taken, but rather

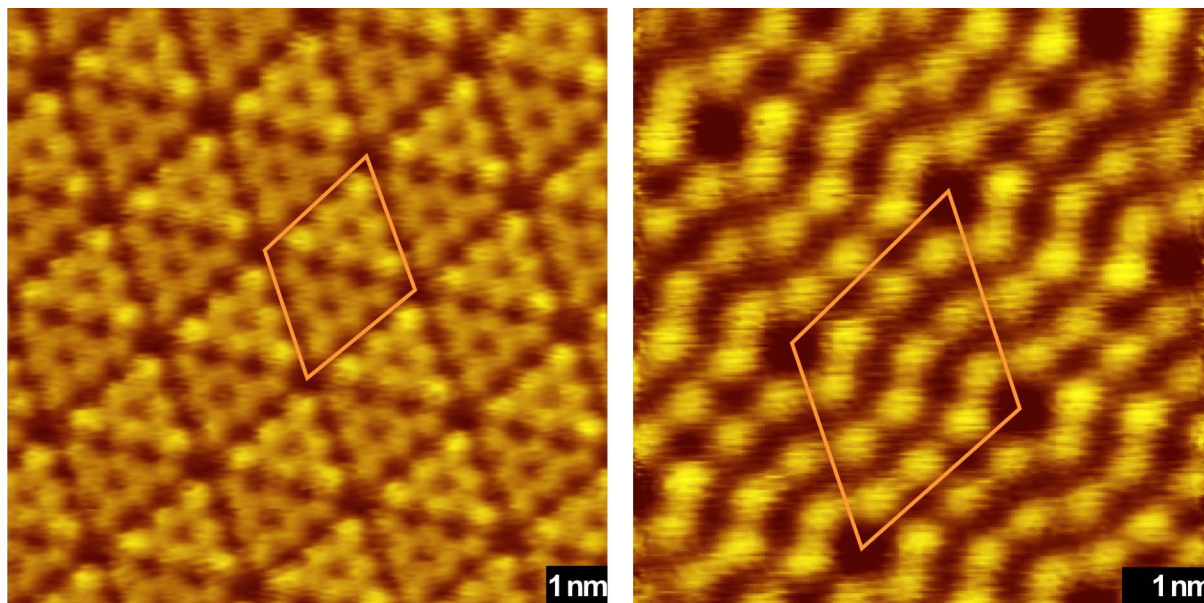


FIGURE 3.20: The unit cell of the Si(111)-7x7 reconstructed surface.

the local density of states is mapped. The 19 dangling bonds of the reconstructed surface contribute to both, the occupied and unoccupied levels that can be accessed via the sign of the bias voltage. Thus, the imaging of the local density of states, gives accurate information about the actual topography of the surface.

Since the particular shape of the electronic structure is well understood [75] and it is of minor importance for our purpose this will not be discussed any further. However, it is important to stress at this point that the scanning tunneling microscope is not only an imaging tool with supreme resolution, but moreover it is used as an analytical tool that permits access to a whole variety of surface properties. Furthermore, it may even serve as a tool for the manipulation of surfaces [76–79], single atoms [80] and large molecules [81]. This leads to the ability to fabricate nanometer scale structures.

Since the apparent distance of two corner holes is known to be 2.668 nm [74] the lateral dimensions of the STM are calibrated accordingly. However, one has to be aware of thermal drifts that could affect the distance between two neighboring corner holes. A detailed lattice based analysis of a recorded image makes it possible to clearly identify the areas of thermal drift. Those areas must be excluded when calibrating the STM. If the tip yields atomic resolution and the surface is reconstructed without defects, a large scale scan admits information to the surface roughness. Especially the total quantity and shape of the apparent, mono-atomic steps are of particular interest since they have severe effect on the tip stability and image quality. A scanning area of  $300 \times 300 \text{ nm}^2$  gives clear

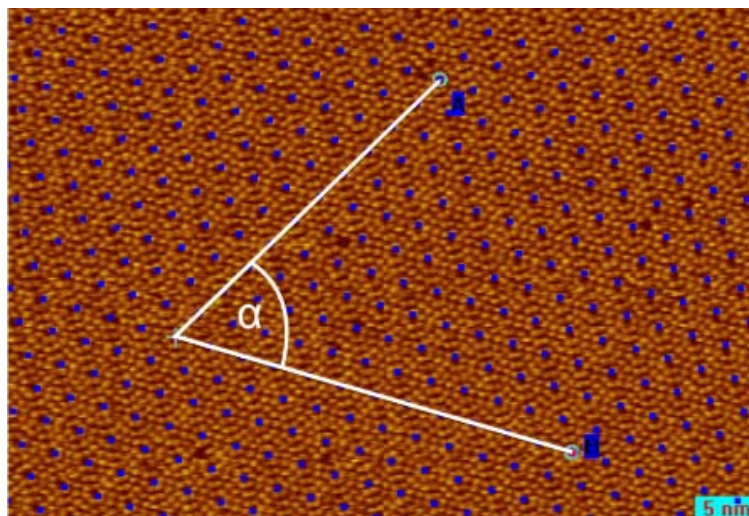


FIGURE 3.21: A lattice based analysis of a STM image of a Si(111)-7x7 reconstructed surface. If the angle  $\alpha$  deviates from  $60^\circ$ , it is a good indication for thermal drift

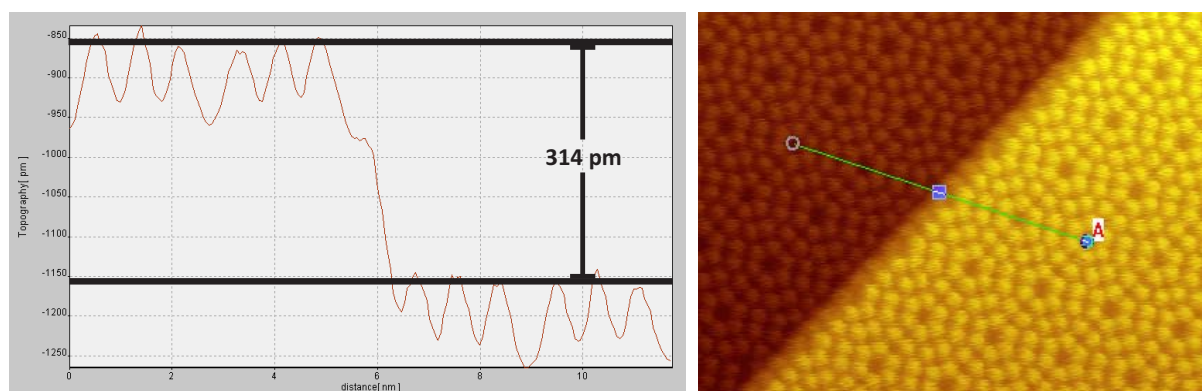


FIGURE 3.22: Detailed analysis of a mono-atomic Si step for the calibration of the vertical STM dimension.

indication of the applicability of the surface based on limited scanning effort. Moreover, a detailed analysis of the mono-atomic steps permits the calibration of the vertical axis of the STM. Since the height  $h = 0.314$  nm [82] is a well known quantity it is perfectly suitable for that purpose.

### 3.8.4 Alignment of the Source and the Velocity Selector

To determine the trajectory of the molecules and to ensure that molecules leaving the furnace actually fly centrally through the interferometer and hit the sample surface, the subsequent approach has been followed. A laser beam predefines a line which is given

by the center of the gratings and the skimmer between the source and the interferometer chamber. The skimmer is monitored by an ordinary digital video camera so that the angle of the laser beam is adjusted with high precision.

If the gravitational selection scheme is used, an additional skimmer is placed between the source and the baffle chamber. This skimmer is aligned to the central interferometer axis so that the laser beam passes it centrally. This is realized by adjusting the height and the angle of the source chamber, which rests upon adjustable feet. To facilitate the alignment, a mirror is placed into the baffle chamber to check whether the laser beam passes the skimmer without the loss of intensity.

The furnace is mounted onto an XY manipulator which allows one to position it so that the laser spot is centrally on the spatial filter. Finally, the second spatial filter which is mounted onto a translation manipulator attached to the interferometer chamber is positioned centrally into the laser beam. Again, this can be precisely done by making use of a video camera which is equipped with high digital zoom rate. If one prefers the helical velocity selection scheme, the alignment procedure is more subtle. Since the vibrations of the rotating selector must be isolated from the rest of the setup, a vibration damping bellow is mounted between the source and the interferometer chamber. Thus, there are far more degrees of freedom than if it were rigidly connected.

Apart from the height of the selector with respect to the interferometer axis the source chamber can be tilted and yawed. Since the resolution of the selector critically depends on the tilt of the chamber because it effectively reduces the length of the rotating helix a precise alignment technique is required. In addition to that, a remaining horizontal angle in the XZ plane exceeding 20 mrad has severe effects on the actual transmitted velocity. For the purpose of precise alignment, two calibration slots of 0.8 mm width have been milled into the aluminum cup. The transmittance of the adjustment laser through one of this calibration slots indicates the correct horizontal angle but has no information about the tilt of the chamber. Thus, one slot is blocked with an opaque, vacuum compatible adhesive that has exactly the height of the milled slots, so that the laser is obstructed if the selector is directly in line with the interferometer axis. This allows precise adjustment of the velocity selector and makes sure that all the molecules that reach the interferometer chamber have actually been subjected to the velocity selection procedure.

To summarize one can recapitulate three adjustment requirements:

- The flashing of the laser point on the furnace with the rotational frequency of the cylinder indicates that the selector is positioned at the appropriate height.

- The maximum intensity of the laser beam transmitted through the calibration slot is reached if the azimuth of the source chamber is negligible with respect to the interferometer axis.
- A diminishing inclination of the velocity selector is assumed if the laser beam is impeded by the adhesive spot in one of the calibration slots.

If all three requirements are met, the furnace is positioned so that the laser spot coincides with the aperture and a perfect line from source to sample is defined.

### 3.8.5 The Experiment

The sample surface is flat and reconstructed. All the pressure conditions are satisfied and the source is brought in a line with the velocity selector and the interferometer. Thus, everything is ready for the actual experiment. As a first step the furnace temperature is gradually risen to the desired temperature of 800 °C. In order to make sure that the heating is done homogeneously a PID controller is connected to the power supply of the furnace so that a precise heating rate of 10 K/min is achieved. But before the sample is transferred to the interferometer chamber, the distance between the first and the second grating has to be adjusted. Usually it takes the electronics of the linear positioner up to 30 minutes to warm up, which is necessary to achieve the highest accuracy. The distance is adjusted by the following rule

$$\Delta z = \frac{1}{5} (\Delta H - 2G2 + G1 + b) \quad (3.28)$$

where  $\Delta H$  is the measured height of the sample related to the steel calibration sample in units of the Heidenhain sensor ( $1\text{u} \hat{=} 0.2 \mu\text{m}$ ),  $G2 = 65330\text{u}$  the measured distance of the second grating to the steel sample (measured onto the wafer frame of thickness  $b = 360 \mu\text{m}$ ),  $G1 = 139075\text{u}$  the distance between the first and the second grating.

If one uses the gravitational selection scheme, the experiment is initiated after the sample is fixed in its designated stage on the interferometer rail, by opening the valve between the source and the interferometer chamber, when the temperature of the furnace has reached the aimed value and the optical table is floated.

However, if the helical velocity selector is used the, vibrational level must be minimized by adjusting the motor coupling before initiating the experiment.

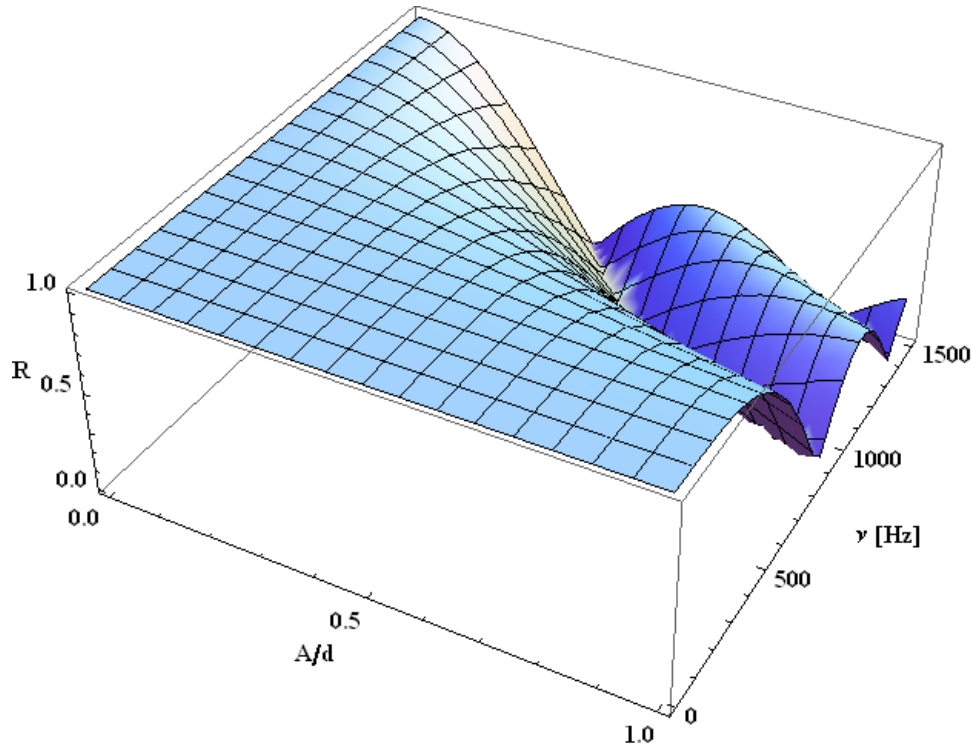


FIGURE 3.23: The visibility reduction factor  $R$  as a function of the frequency  $\nu$  and the proportion of the measured mechanical deflection to the grating constant.

The influence of vibrational perturbations is studied in [54]. It turns out that only the transverse shifts have a significant effect on the visibility, which is described by the reduction factor  $R_p$ . If we assume that the whole interferometer exhibits fixed pendulum oscillations, one finds the reduction factor

$$R_p = \left| J_0 \left( 8\pi \frac{A}{d} \sin^2 \left( \frac{\nu L}{v_z} \pi \right) \right) \right| \quad (3.29)$$

where  $J_0$  is the zero order Bessel function with the driving frequency  $\nu$  of vibrations with amplitude  $A$ . In order to find a quantitative result the vibrational level is monitored with an accelerometer which is read out and Fourier-analyzed by a fast oscilloscope (LeCroy Waverunner). To calculate the exact mechanical deflection  $A$  generated by vibrations with an angular frequency  $\omega = 2\pi\nu$  of the velocity selector one has to translate the measured acceleration according to

$$x = \cos(\omega t) \quad (3.30a)$$

$$\ddot{x} = -\omega^2 \cos(\omega t) \quad (3.30b)$$

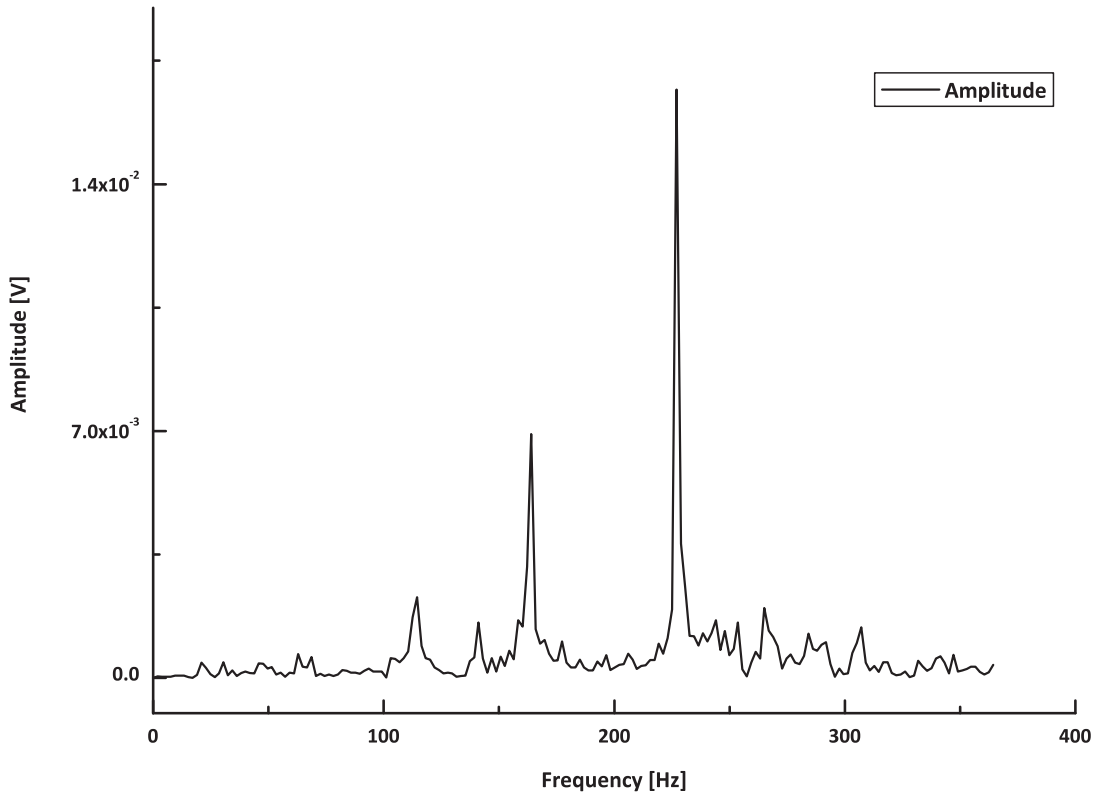


FIGURE 3.24: A Fourier analyzed vibration spectrum of the helical velocity selector rotating at a frequency  $\nu = 114$  Hz. The accelerometer is rigidly attached to the interferometer chamber in radial direction. The second harmonic has larger amplitude, but the deflection is reduced by a factor of four, due to the higher frequency.

Inserting the first into the second equation yields

$$x = -\frac{\ddot{x}}{\omega^2} \quad (3.30c)$$

The specifications of the accelerometer yield a calibration factor of  $1 \text{ V} \hat{=} 10 \text{ m/s}^2$  which corresponds to a deflection  $x = 2.5 \cdot 10^{-5} \text{ m}$  at a driving frequency  $\nu = 100 \text{ Hz}$ . Typically, we measure a vibration level of  $5 \text{ mV}$  if the maximum amplification factor of  $100$  is set. This gives rise to a prevailing mechanical deflection of  $1.25 \text{ nm}$ . Since this adds up to only  $0.5\%$  of the grating constant this effect can be neglected. Furthermore, the time-of-flight of a particle with a velocity of  $100 \text{ m/s}$  through the interferometer is of the order  $0.1 \text{ ms}$  and thus very small compared with the period  $T = 10 \text{ ms}$  of the grating oscillation. This reduces the effective deflection to only  $1\%$  of the maximal value. Hence the resulting effective deflection of the gratings during the transit of a molecule reduces to  $0.005\%$  of the grating constant, which is negligibly small. After the vibration level is adjusted the sample is placed into the stage on the interferometer rail.

The laser which is used for the adjustment of the source and velocity selector is switched on again to check whether it hits the sample surface centrally from the backside to ensure that the surface is in line with the interferometer, the velocity selector and the source.

To conclude one can point out that the small dimensions of the interferometer lead to very high stability of the setup to external, vibrational excitations and thus offers unique preconditions for a successful experiment.

## 3.9 Evaluation

Half an hour at a furnace temperature of 800 °C yields a coverage of the sample with 1/1000 of a monolayer independent from the velocity selection scheme. Hence, after the sample has been exposed the valve is closed again and the sample is transferred into the analysis chamber where the surface is scanned. Since the evaluation strategy heavily depends upon the velocity selection scheme, the situation when gravitational selection is used is described separately from the helical.

### 3.9.1 Gravitational Selection

The sample stage of the microscope must be decoupled from the environment by lowering its position fixing clamps. A bias voltage of 1.7 V is applied and the feedback parameters adjusted. The slope of the sample with respect to the microscope must be reset. The sample is monitored by a two megapixel webcam via adjustable zoom optics with a magnification factor of 40. The tunneling tip is fixed in the scanning head that rests with its three piezo tubes on the sample holder. The sample holder is free-hanging in a spring suspension system which is damped by an eddy-current brake to avoid any influence of external vibrations.

The positioning of the tip is realized by moving the scanning head over the surface. In a first approximation, it is sufficient to use a simple overlay technique to get an impression of the distances one travels on the surface. An elementary drawing software is superimposed to the webcam read out software (*Matlab*) by increasing its transparency. This permits a rough notion of the traveled distances by comparing the length between two labeled spots with the diameter of the sample that scales the magnification. Length measurement in pixels can be easily done in *Adobe Photoshop* by using the ruler tool. Furthermore, the

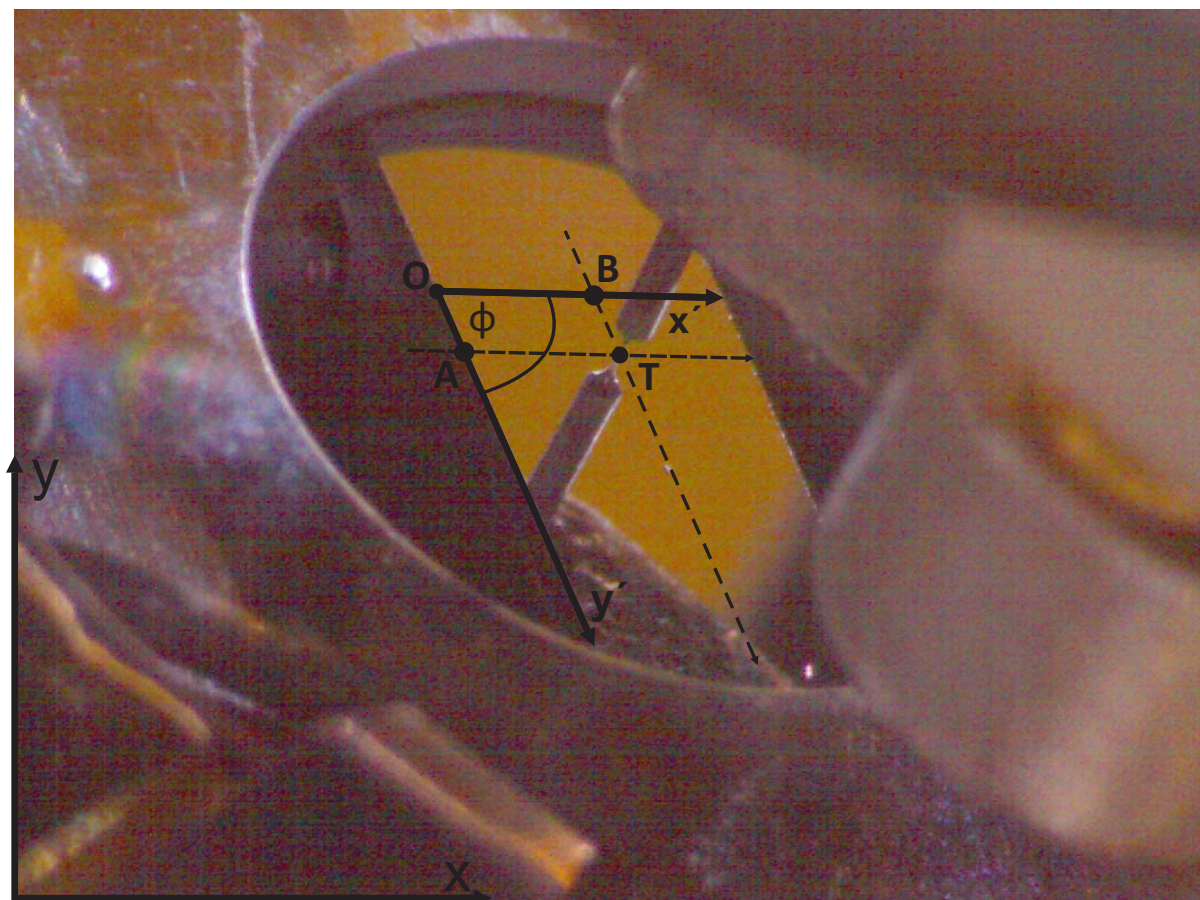


FIGURE 3.25: An image of the tip and its reflection in the surface. The point  $T$ , where the tip touches its reflection defines the accurate tip position. The coordinates of point  $T$  are then translated into the local coordinate system  $(x',y')$ , so that relative measurements of the scanning position are possible with high accuracy ( $5\ \mu\text{m}$ ). The angle  $\phi = 64.7^\circ$  is measured by introducing a bisected sample, so that the actual angle between the two sides of the sample can be identified.

correct angle for an accurate measurement of the sample width is displayed and adjusted. However, since the viewpoint of the camera is not parallel to the surface, the edges of the surface are not perpendicular. Thus, the local coordinate system is rotated and nonorthogonal. Accurate measurement of the sample width to scale the image is only accomplished if the angle is known with high precision. In order to do so, a bisected sample surface with orthogonal edges is measured with the ruler tool along the cleaved edge. The measurement yields the result that the square angle of the sample edges is depicted as  $\phi = 64.7^\circ$  on the screen. Since the displayed square angle of the sample and the orientation of the local coordinate system  $(x',y')$  in Figure 3.25 depend on the orientation of the camera, the angle measurement must be redone after each bake out procedure where the optics must be removed due the high temperatures. However, once the angle is determined, accurate measurement of the sample width in pixels is feasible

and yields the scaling factor  $1 \text{ px} \hat{=} 5 \text{ }\mu\text{m}$ . Since the tip is reflected on the sample surface one can easily define the central point between them which is then marked by a dot  $T$ .

To ensure that accurate tip positioning is still guaranteed if the tip is exchanged as a consequence of a tip crash, a local coordinate system  $(x',y')$  is introduced. This is necessary due to the fact that the scanning head slightly drags the sample holder when the tip is moved to a new position. Therefore the global coordinate system of the image  $(x,y)$  is futile.

High precision in identifying the tip position  $T$  is obtained by zooming to the level where individual pixels can be identified. The  $x$  and  $y$  value is recorded. The  $y$ -axis is defined by two points on the edge of the sample and the  $x$ -axis is constructed by rotating about the angle  $\phi$ . The identification of the pixels to define the  $y$ -axis is done several times to ensure that the method is repeatable. The inclination of the sample with respect to the window frame is calculated from that. Therefore the global coordinate system  $(x,y)$  of a live image with the origin in the bottom left corner is firstly translated and rotated onto the sample surface by the usual coordinate transformation

$$\vec{r}'' = \begin{pmatrix} x'' \\ y'' \end{pmatrix} = \begin{pmatrix} \cos \Phi & -\sin \Phi \\ \sin \Phi & \cos \Phi \end{pmatrix} \begin{pmatrix} x - a \\ y - b \end{pmatrix} \quad (3.31)$$

where  $a$  and  $b$  are the coordinates of the selected origin on the sample surface. The angle of transformation is defined as  $\Phi = 90 - \theta$  where  $\theta$  is the angle of inclination which is determined by two pixels on the edge of the surface with coordinates  $(x_1, y_1)$  and  $x_2, y_2$  by

$$\theta = \cos^{-1} \left( \frac{|x_1 - x_2|}{|y_1 - y_2|} \right) \quad (3.32)$$

Secondly the angle between the axes is adjusted. The coordinates of the tip position  $T$  are then translated into this new coordinate system according to  $x' = x'' / \cos \xi$  with  $\xi = 90 - \Phi - \phi$  and  $y' = y''$ .

It is of utmost importance to position the tip with such high accuracy when dealing with the gravitational selection because different velocities are located at different heights of the sample. One has to bear in mind that if all the particles with high velocities (above 200 m/s, which is about 35% of the whole Maxwell-Boltzmann distribution) follow almost the same trajectory (see Figure 3.6) the maximum coverage is to be expected there. Thus, if this area can be identified precisely, it can be assumed that the location of the velocity which is accurate for the interferometer is found 300  $\mu\text{m}$  below this point if the sample is orthogonal to the interferometer axis.

The above presented straight forward method represents a fast approach and allows accurate tip positioning which is a crucial ingredient for effective evaluation. This leads us now to the first part of the evaluation procedure.

### 3.9.1.1 Determination of the Sample Coverage as a Function of the Falling Height

An essential step during the evaluation of the sample is the determination of the coverage as a function of the falling height. Since this is a direct indication for the velocity distribution it fulfills two particular purposes. Firstly the desired velocity of 100 m/s is located about 300  $\mu\text{m}$  from the maximum intensity. Secondly, one has access to direct information about the actual velocity distribution of the molecules.

It is useful to divide the sample into sectors of equal size so that one has a guiding grid (700x700  $\mu\text{m}^2$ ) which helps to find the spot on the sample. Since the molecules are usually spread over an area of 1  $\text{mm}^2$  it is rather simple to find a location where the first molecules appear. Figure 3.26 shows the internal, electronical structure of a single fullerene. It is useful to cool the sample to cryogenic temperature if the internal structure is resolved, but it is not necessary since even the rotational degree of freedom is suppressed [83] due to the strong bonding nature between the molecules and the surface. The shape of the molecular orbital depends heavily on the position the molecule is adsorbed to and, moreover, on the bias voltage. However, the resolved internal structure can clearly be seen and meets theoretical simulations given in [84–86]. Since the coverage rate is independent of the lateral dimension  $x$ , the determination of the sample coverage is initiated from this point. From there one follows in large steps of about 30  $\mu\text{m}$  the local  $y'$ -axis and records an image of about 200x200  $\text{nm}^2$  for each location. This size yields sufficient information about the coverage and can still be scanned within a few minutes. Therefore it represents an efficient technique for acquainting information about the actual deposition rate. To be sure that one is not deceived by statistical errors, it is advisable to record two or more images at the same location and averages. For this purpose, one can access an area of about 5x5  $\mu\text{m}^2$  via the software of the microscope.

The result of such a measurement is depicted in Figure 3.27. The experiment yields a considerable difference to the theoretical prediction. Since the number of the deposited molecules as a function of the falling height is a direct measure for the quality of the velocity selection, one can deduce two reasons: first, the actual velocity distribution of the molecules that are sublimed in the Knudsen cell can not be approximated by a

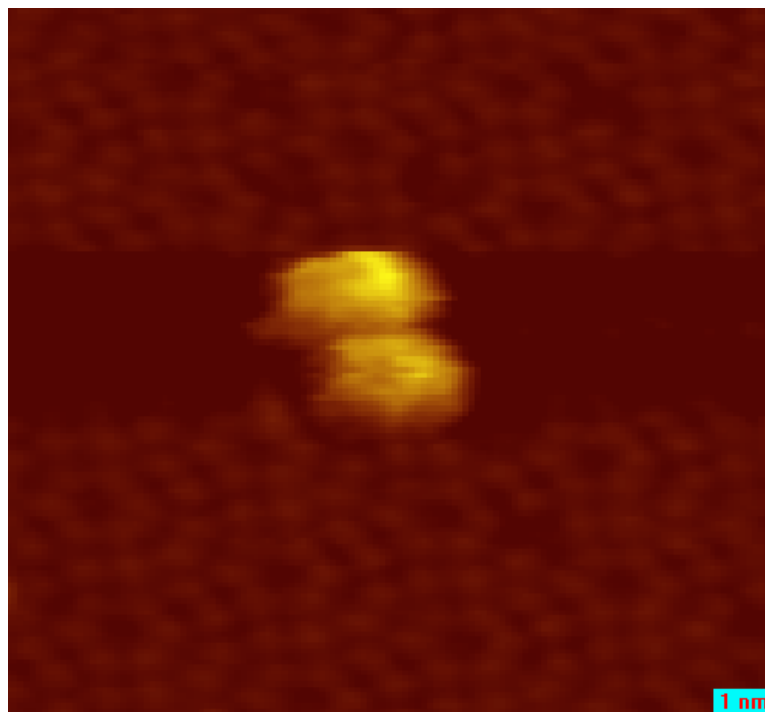


FIGURE 3.26: Single  $C_{60}$  molecules on the silicon surface. One can still see the adatoms of the Silicon surface which indicate very good pressure conditions during the experiment and the transfers. The image is taken at a sample bias of +2 V and even resolves the molecular orbitals. This image is taken at 25 K.

Maxwell-Boltzmann distribution. Second, scattering at the second spatial filter leads to a broadening of the distribution. This would also explain why the resulting distribution is of rather symmetrical shape.

### 3.9.1.2 Scanning for Interference Contrast

The spot size is identified and the coverage of the sample surface with molecules as a function of the falling height is given. To get a clear image of the resulting interference pattern it should be noticed that the more periods appear on the image the clearer the contrast can be analyzed. Thus, large areas of  $1.5 \times 1.5 \mu\text{m}^2$  must be scanned which requires an immense tip stability. Setting the resolution to a satisfying value of 1024 points per line, which is enough to ensure that no molecule is missed, one image takes 33 minutes at a scanning speed of  $1.5 \mu\text{m}/\text{s}$ , which once more elucidates the need for an ultra stable tip geometry. Moreover, the chance of acquiring an image successfully is increased if the boundaries of the image are free of dirt which could influence the quality of the image. This can be checked in advance by continuously rotating the scanning direction.

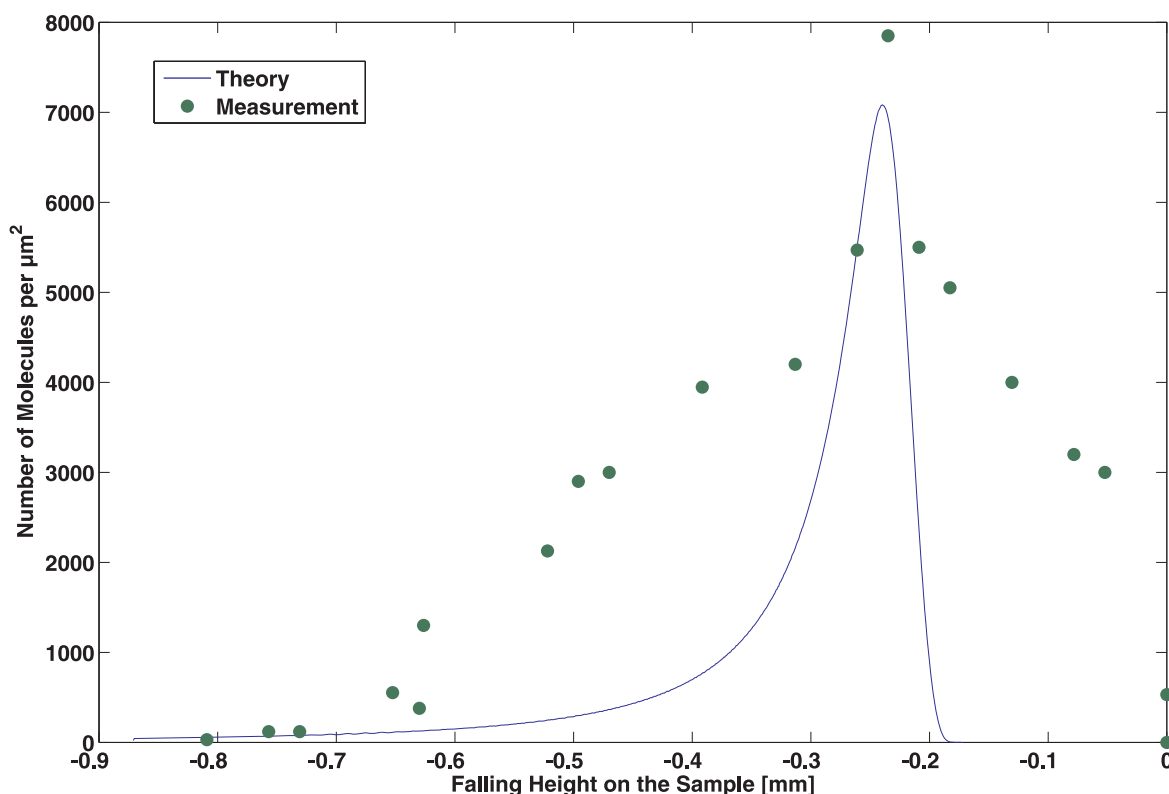


FIGURE 3.27: The total number of molecules per  $\mu\text{m}^2$  as a function of the falling height on the sample. The measured dependence of the coverage as a function of the falling height differs considerably from the theoretical description

If the area is clean and the tip yields satisfactory pictures of the molecules, the recording of the large scale image is initiated.

### 3.9.2 Helical Velocity Selection

On the other hand, if the helical velocity selector is used, its unique feature that only the molecules with the suitable velocity are transmitted, leads to an enormous facilitation of the analysis procedure. Since only a limited class of velocities is deposited on the surface, one does not need to find the right velocity. Thus the scanning effort is dramatically reduced. However, since it can occur that there is a slight misalignment of the furnace with respect to the interferometer, it is possible that not all of the molecules pass through the full length of the selector. Hence, one is on the safe side, when the scanning process is not limited to a single location, but rather to three spots at different heights. Usually after each approach the tip deposits some material on the surface. Thus it makes sense

to move the tip by a few  $\mu\text{m}$  while it is manually retracted with the z-coarse regulator: a soft and easy method to ensure that the scanning area is free of impurities due to too fast tip approach.

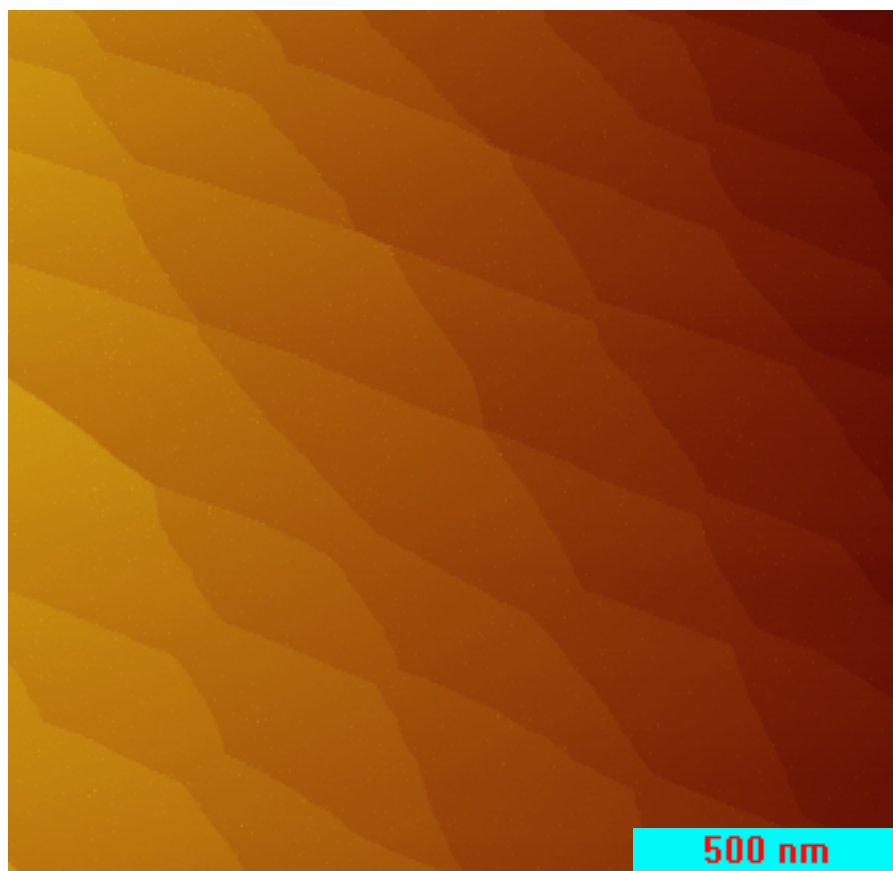


FIGURE 3.28: An extract of a large scale  $2.25 \mu\text{m}^2$  image. The numerous steps make it impossible to see the interference pattern by eye. Thus postprocessing is required where the individual molecules are identified and plotted as a function of the transversal coordinates.

# Chapter 4

## Image Evaluation & Discussion

The huge advantage of the scanning tunneling microscope is its resolution. However, when it comes to the scanning of large areas this advantage turns out to be also the major challenge. Changes in the tip geometry due to excessive scanning over a grainy surface covered with large molecules, mono-atomic steps of the silicon surface, residual gas particles and tip material deposited on the surface, all effect the quality of the resulting images. Thus a distinct method for the identification of molecules and the numerical evaluation of the interference pattern is necessary.

### 4.1 Image Evaluation

A clear and unmistakable indication for the presence of a molecule is its height and size with respect to its surrounding. An image showing individual molecules on the reconstructed surface is demonstrated in Figure 4.1. But, in addition to the shape of the molecules, their height also depends upon the tip geometry [87]. Therefore if a pixel value fulfills the condition  $0.5 \cdot 10^{-9} \text{ m} < H < 0.8 \cdot 10^{-9} \text{ m}$  with respect to its adjacent pixel values, the molecule is identified. Since this can easily be done automatically the image is exported as an ASCII file and loaded into the evaluation software which is extensively described in [42]. This program identifies the molecules, sums all the molecules of the  $1024 \times 1024$  pixel matrix column by column and plots the total number for each column as function of the column index. This analysis should exhibit a sinusoidal dependence with a periodicity of 257.4 nm.

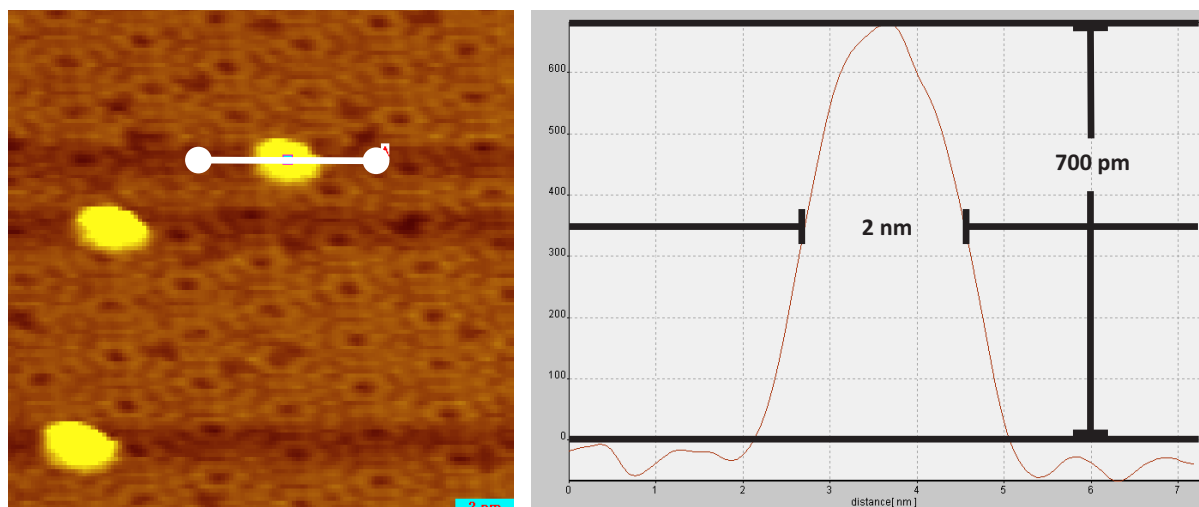


FIGURE 4.1: The appearing height and lateral dimensions of a molecule critically depend on the geometry of the tip. A new way for producing ultra sharp tips with a very small apex radius lead to satisfying results.

However, the orientation of the interference pattern within the recorded image is not the same for all runs, but rather is related to the scanning tip length. The three feet of the scanning head rest upon a helically shaped stage on the sample holder. Thus, the simple rotation of the head lowers the tip by a specific amount defined by the pitch of the helical stage. At this point, it becomes obvious that the tip length plays a crucial role for the ultimate orientation of the scanning head. If the coordinate system of the scanning tip is rotated in respect to the surface, the interference pattern appears to be rotated as well. Accordingly, it is not enough to simply sum the pixels for each column, but rather evaluate the contrast as a function of the rotation angle. In order to do so, the binary matrix constructed from the identification process is rotated by an increment angle  $\phi$  and for each column the total number of molecules is recorded. Every angle  $\phi$  yields its characteristic dependency that is subsequently Fourier analyzed and fitted with a sine function. The visibility as a function of the angle  $\phi$  gives clear indication about the rotation of the interference pattern.

Since the rotation of the scanning axes can be adjusted manually, it is convenient to compensate for this offset in order to ensure that all the recorded data is used for the evaluation. Explicit evidence for quantum interference prevails if high contrast is found for a specific angle  $\phi$  with a sinusoidal fit of exactly the predicted periodicity.

The raw image of Figure 3.28 is subjected to the evaluation procedure described above and evaluated. The resulting binary matrix and evaluated interference contrast is depicted in

Figure 4.2.

## 4.2 Discussion

In Figure 4.2 the result of a successful experiment is displayed. The top part of the figure depicts the actual interference pattern which can be clearly seen. A precise image of the second grating, created by individual, large fullerene molecules, due to quantum interference is recorded on a silicon surface. However, to elucidate the contrast even further  $7 \times 7 \text{ px}^2$  are binned to a single pixel.

In order to evaluate the interference pattern the binary matrix is rotated about the angle identified by the evaluation software and the pixels are summed column by column. This allows to gain a quantitative estimate of the interference contrast and gives clear indication for quantum interference. Since the wavelength fitted by the evaluation software is  $244 \pm 1 \text{ nm}$  and thus deviates only by 5% of the expected value of 257 nm, the assumption that the image is created due to the wave nature of the molecules is confirmed. The slight discrepancy can be explained by minimal thermal drifts during the scanning process.

The interference contrast  $V = 34\%$  is only half of the expected visibility of 70%, but still the mere fact that there is visibility is a clear indication for quantum interference. Furthermore, the experiment has been repeated several times with different velocity selection schemes, always yielding the above mentioned visibility. Regarding the long exposure time of 30 minutes due low molecular flux, the effect of thermal fluctuations on the stability of the interferometer could be a reasonable explanation for the observed reduction of visibility. This is now further investigated. The replacement of the steel parts by materials that exhibit minor length variations due to thermal fluctuations represents a consecutive step towards higher stability. Combined with a spring suspension for the interferometer which is dampened by an eddy current system, this could lead to even increased mechanical rigidity and isolation. In addition to that, the overall length of the apparatus can be dramatically reduced, since the helical velocity selector does not need long distances to yield high resolution. Thus the signal can be increased by a factor of ten which would result in an exposure time of three minutes. High stability combined with length reduction, thus provides unique opportunities for future applications.

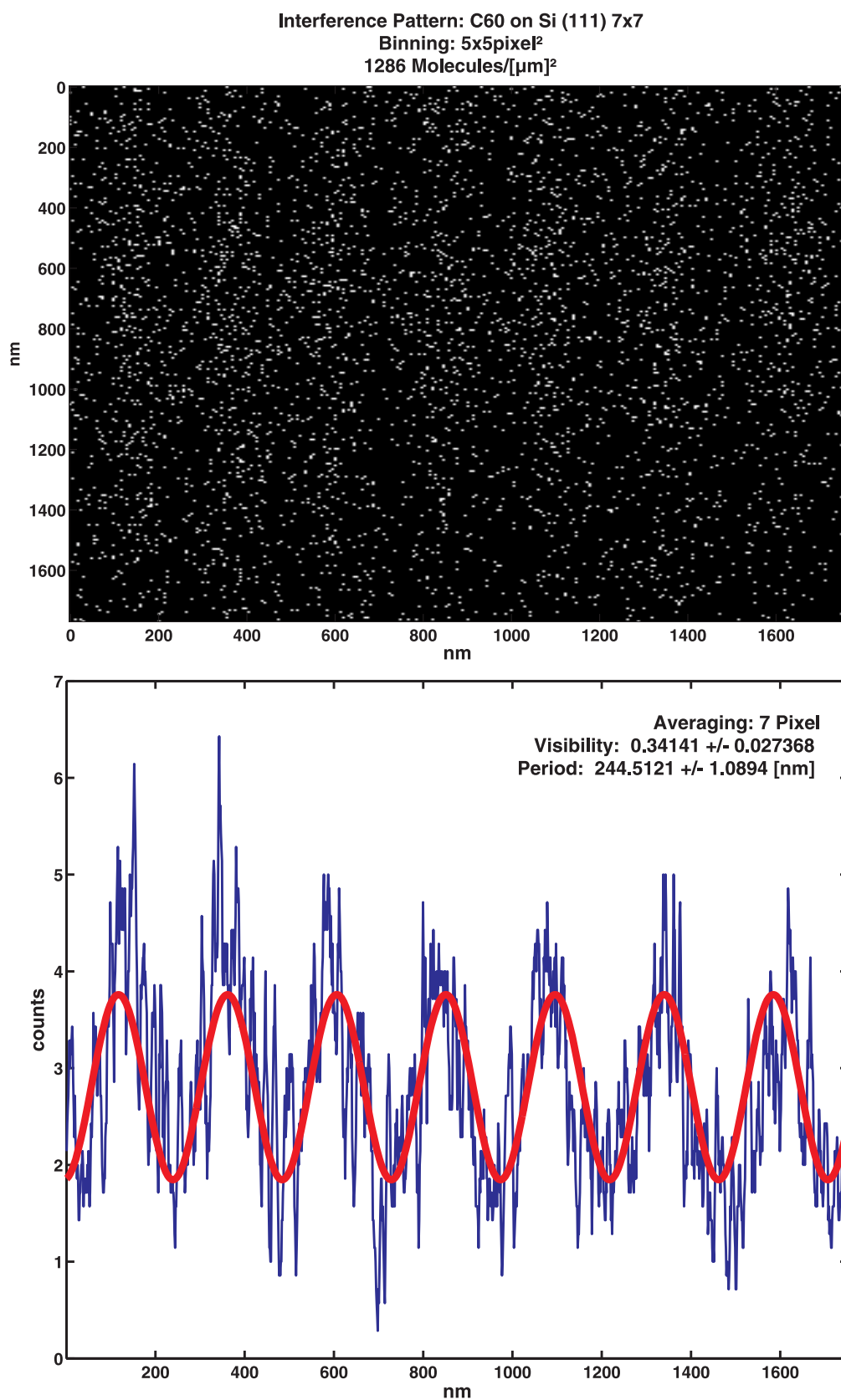


FIGURE 4.2: The image on the top depicts the evaluated interference pattern and the figure beneath the number of molecules as a function of the column number. This allows to fit a sine function to the evaluated data in order to get a quantitative result for the interference contrast.

# Chapter 5

## Conclusion & Perspectives

### 5.1 Conclusion

The introduction provided the reader with historical details in order to gain insight to a development which is characterized by a dialectic discourse between value conserving authorities and revolutionary minds. It is the progress arising from these vivid conversations in the early 1930s that established the logical framework for the presented work here. The fact that eighty years later we are still not able to estimate all the consequences emerging from these radically new thoughts, indicates the importance for experiments elucidating the fundamental aspects. Furthermore, we discussed the theoretical requirements that are essential preconditions for the concrete physical realization. New methods have been introduced to guarantee a continuous work flow and essential inventions regarding the velocity selection of a molecular beam and the imaging process have been realized. The high precision of the alignment procedure we developed, coupled with the improvement of the vacuum conditions made it possible to present the first successful surface images of molecular interference patterns as an important result of this thesis.

### 5.2 Perspectives

The experiment presented here leads the long tradition of the double slit experiment to a new climax by revealing the wave-particle duality of large, massive, complex and hot molecules in its most distinct form. The molecules are filled into the furnace as solid powder, leave the orifice as single, individual buckyballs and *explore* on their way

through the interferometer, an area which is orders of magnitude larger than their physical appearance or de Broglie wavelength, to then be finally deposited on a surface where they appear as single, individual molecules again.

Whereas history shows the creation of interference patterns for elementary particles like electrons, neutrons or single atoms we explore hereby a new field of complexity in matter wave interferometry. For the first time it is possible to actually *see* the interfering particles with atomic resolution by associating molecular quantum optics with nanotechnological methods.

Apart from the mere foundational approach to detect molecules of increasing mass and complexity with high efficiency to probe the quantum to classical transition the presented method offers an alternative route towards structuring of complex molecules. Although lithographic imaging using masks (of light) is a well established technique for atoms, the contact free method using near field interferometry offers interesting possibilities for particles with complex internal structure that could serve as single functional elements.

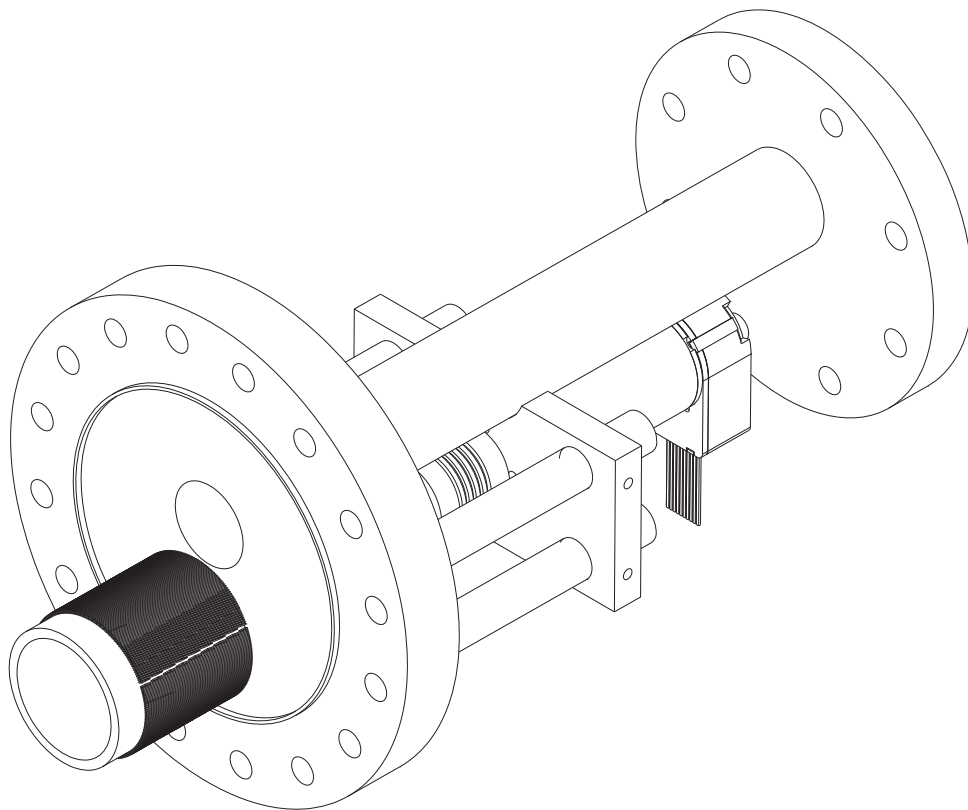
Depositing complex molecules on a silicon substrate in a structured and periodic way over large areas, could herald a new era of lens free imaging of nanometer-scale patterns for imprinting logical elements onto semiconductor surfaces. Although it might not be considered as a serious candidate for a next-generation lithography technique for replacing optical lithography in computer chip production, scientific applications of regular molecular structures at nanometer scale will play an important role in the future.

Since demagnifying interferometers [26] that make use of the fractional Talbot effect are in principle capable to writing structures of a few 10 nm width it could serve as a complementary tool to other lithographic techniques like electron-beam direct-write lithography (EBDW) and double patterning. Furthermore, regarding the recently developed approaches like Dip-Pen Nanolithography (DPN), our quantum optical nano-structuring could be ideally utilized for a rough prestructuring followed by a scanning probe nanopatterning technique such as DPN to refine it. Furthermore, technological applications involving chemically amplified fullerene resist material deposited on semiconductor surface could serve as an ideal precondition for various kinds of chemical post treatment on the nanometer scale. In addition to that, applications of fullerenes and their derivatives range from solar cells or composite polymers to molecular electronics. Whereas it has still to be proven to what extent our work is industrially viable, its innovation in the combination of closely related but previously carefully delimited fields - quantum optics, surface science and scanning probe microscopy. Furthermore, the work provides access to the most

fundamental questions in physics and simultaneously marks the initial point for fruitful technological applications.

# Appendix A

## Helical Velocity Selector



---

FIGURE A.1: The helical velocity selector is mounted onto a ferrofluid sealed vacuum feedthrough from *Beamtech*. It is driven by a high-power *Mason ESC-powerboat* brushless servomotor with 200 W output power to provide a continuous torque of 120 mNm. The encoder has a resolution of 1000 impulses per revolution in order to provide accurate rotation speeds. The flexible bellow coupling allows a slight mismatch of the motor shaft in respect to the vacuum feedthrough.

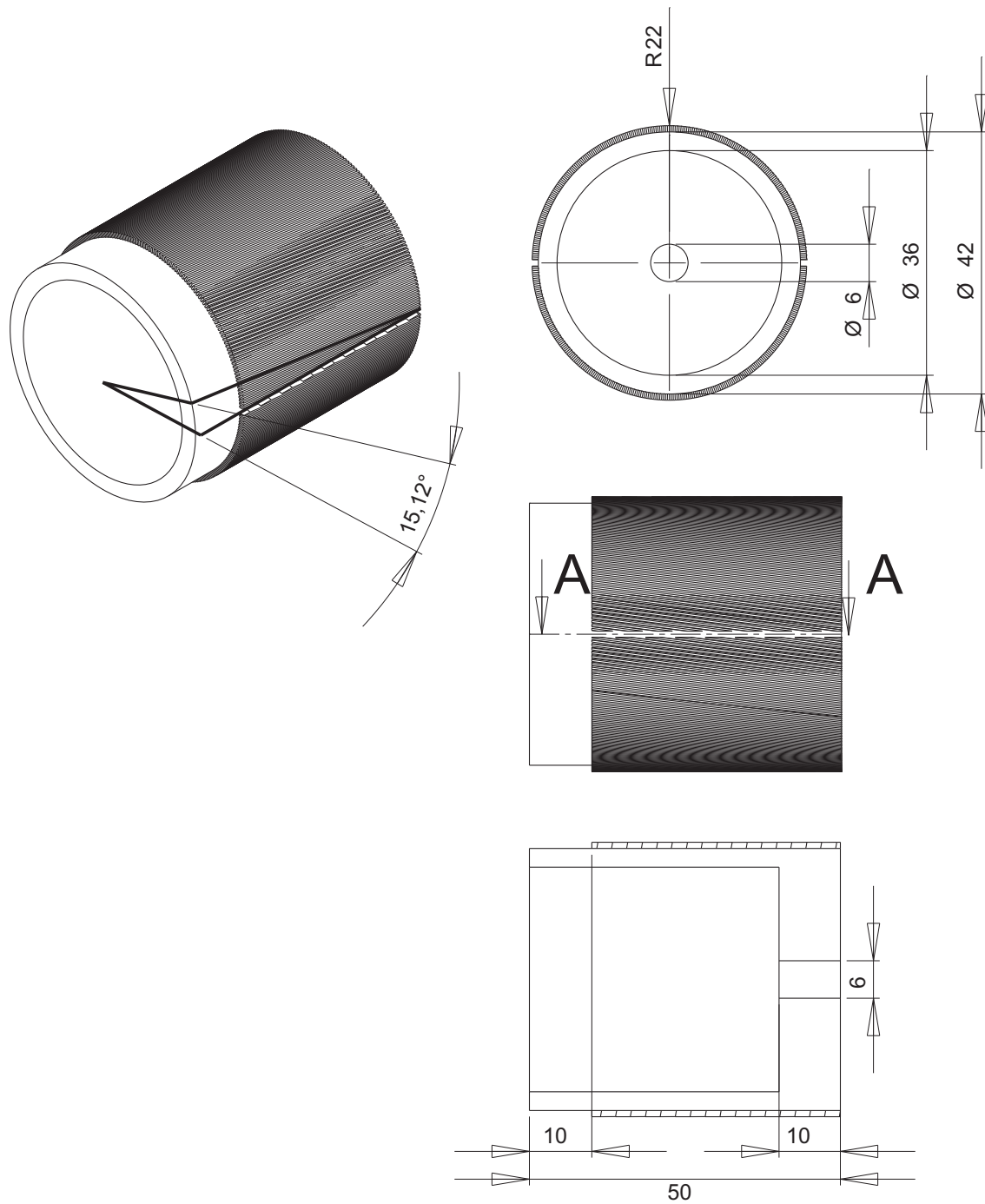


FIGURE A.2: The helical velocity selector. The geometry yields low inertial weight which allows to mount it directly onto the shaft.



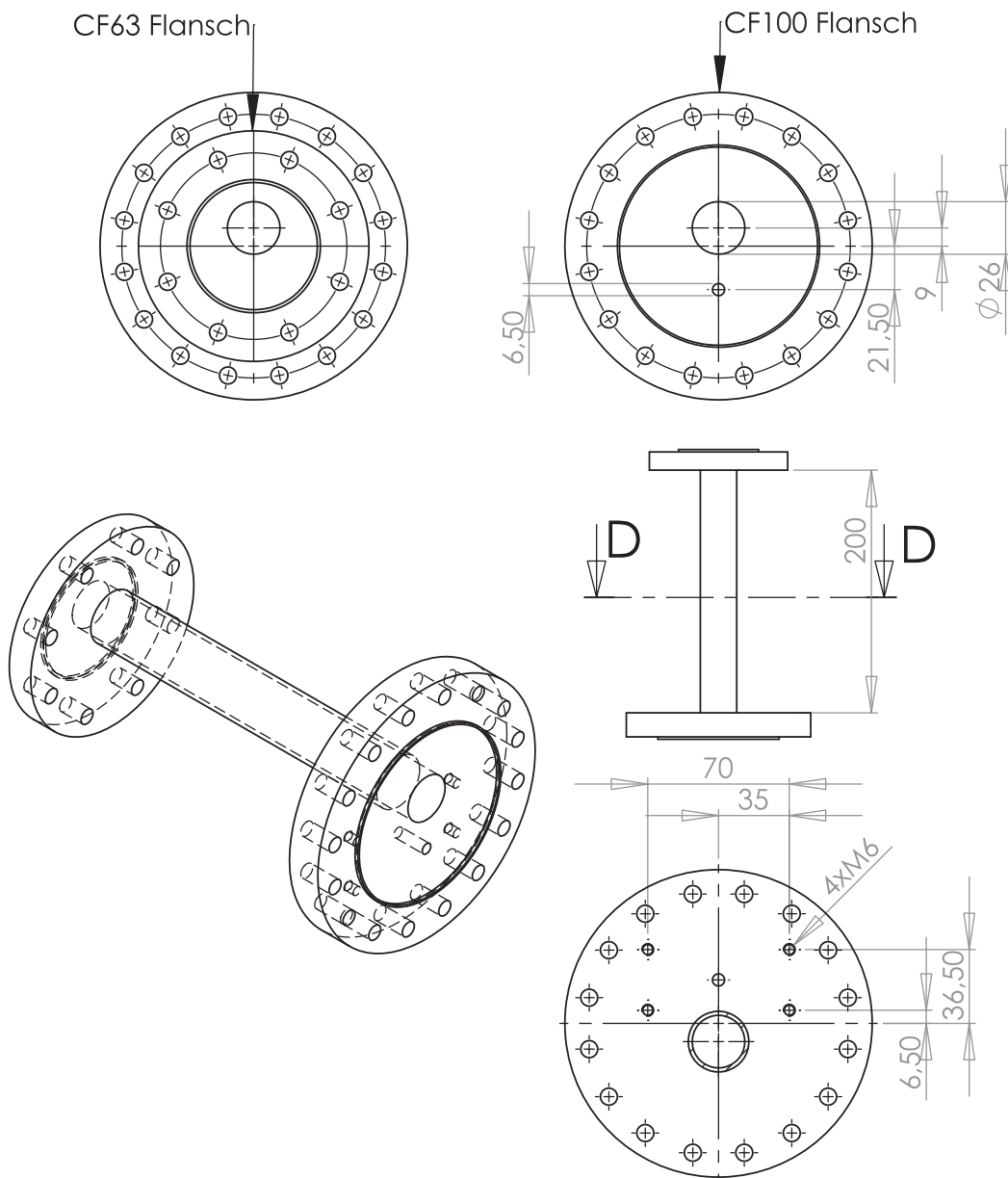


FIGURE A.4: The vacuum flange.

# Appendix B

## Slotted Disk Velocity Selector

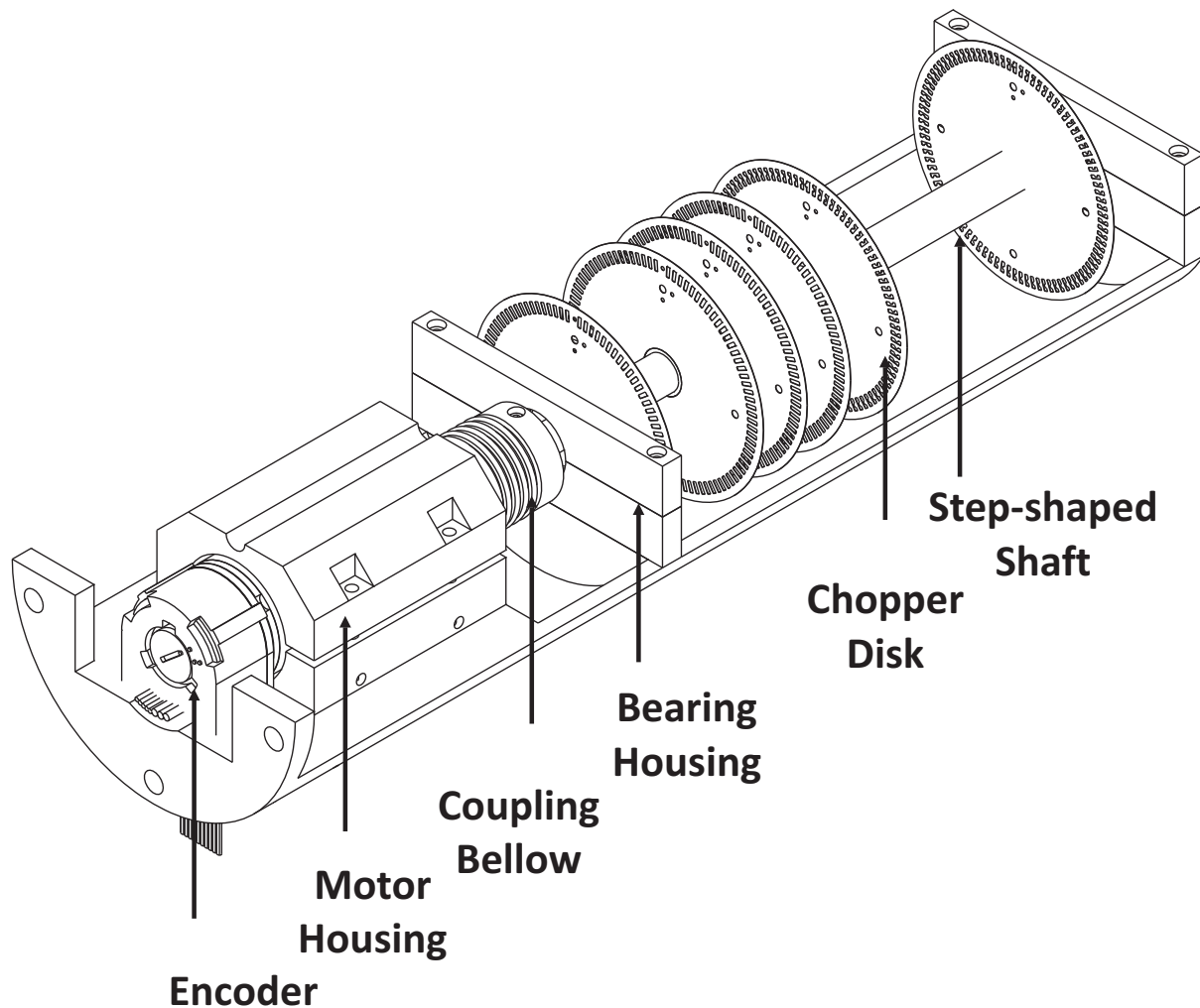


FIGURE B.1: The slotted disk velocity selector. It is directly attached to a CF 100 flange and mount into the vacuum chamber.

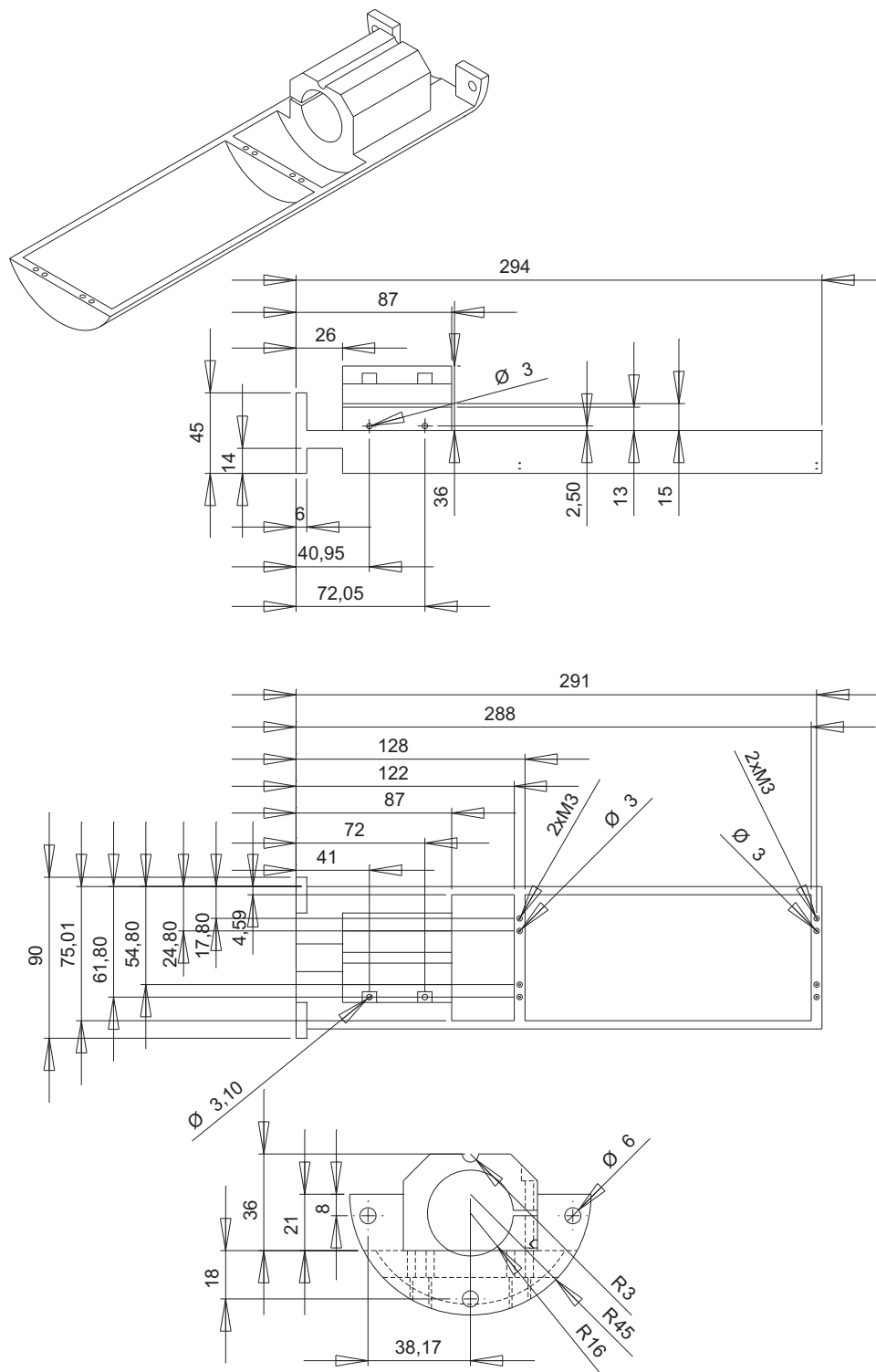


FIGURE B.2: The mounting is fabricated from a single stainless steel piece, to guarantee high accuracy which is needed for low vibrational noise.

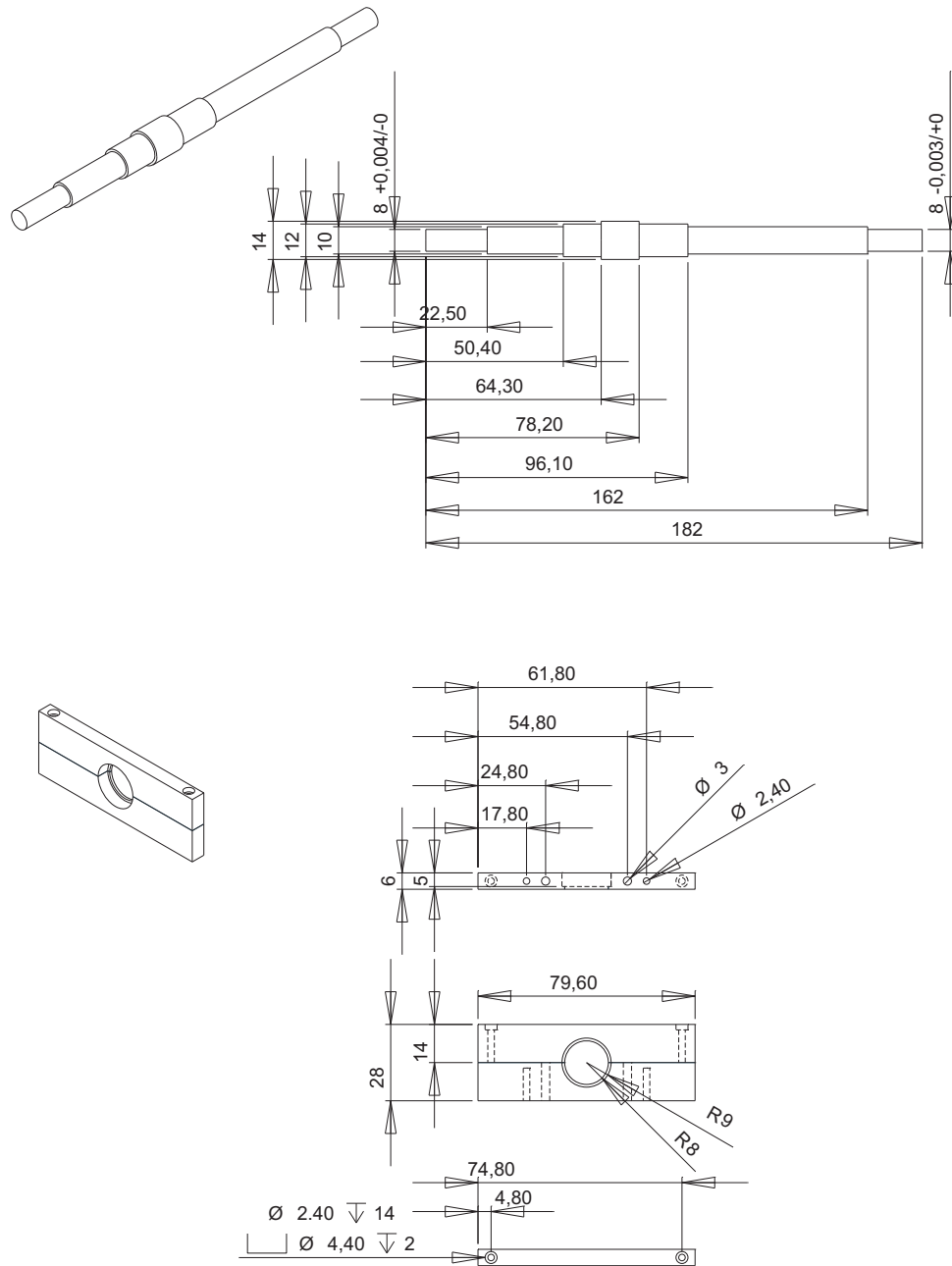


FIGURE B.3: The step-shaped shaft does not have to be balanced due to its isotropic geometry. In addition to that the accurate distances between the disks is predefined.

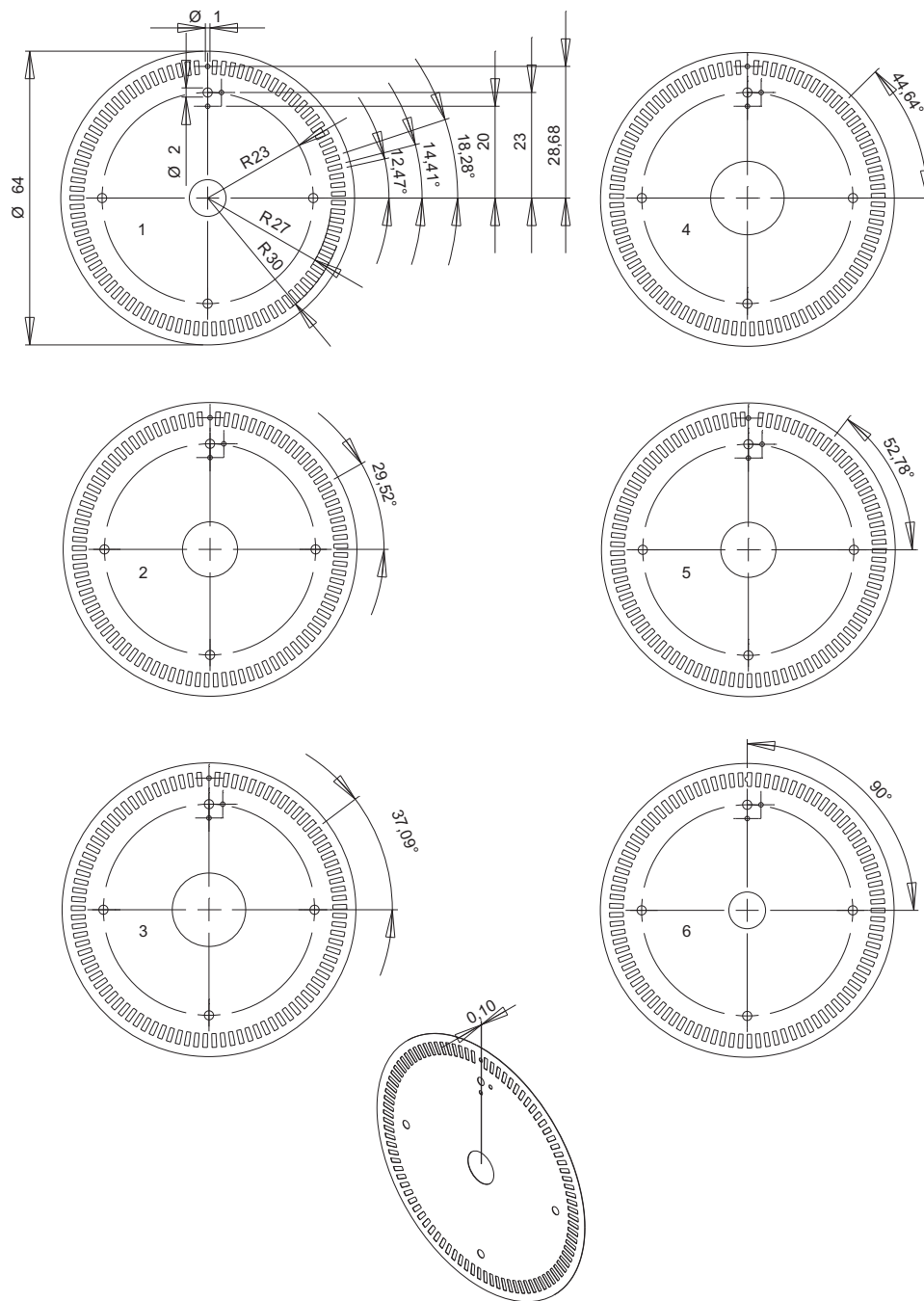
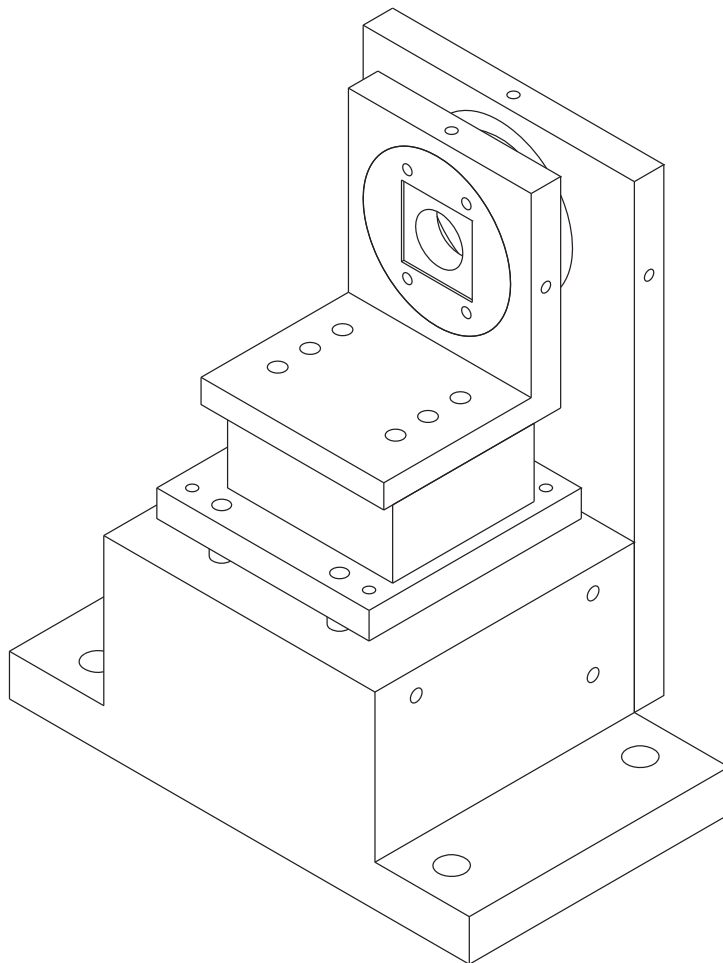


FIGURE B.4: The slotted disks. For the sake of better illustration disks are depicted, that yield a resolution of  $\sigma = 0.05$ . If better resolution is needed the slot-width has to be adjusted accordingly. However, the angles of the disks in respect to each other remain indifferent.

# Appendix C

## Interferometer



---

FIGURE C.1: The grating holders have to be made of stainless steel, in order to minimize length variations due to thermal fluctuations. The angles must be easily adjustable, but have to be fixed firmly if they are in the right position.

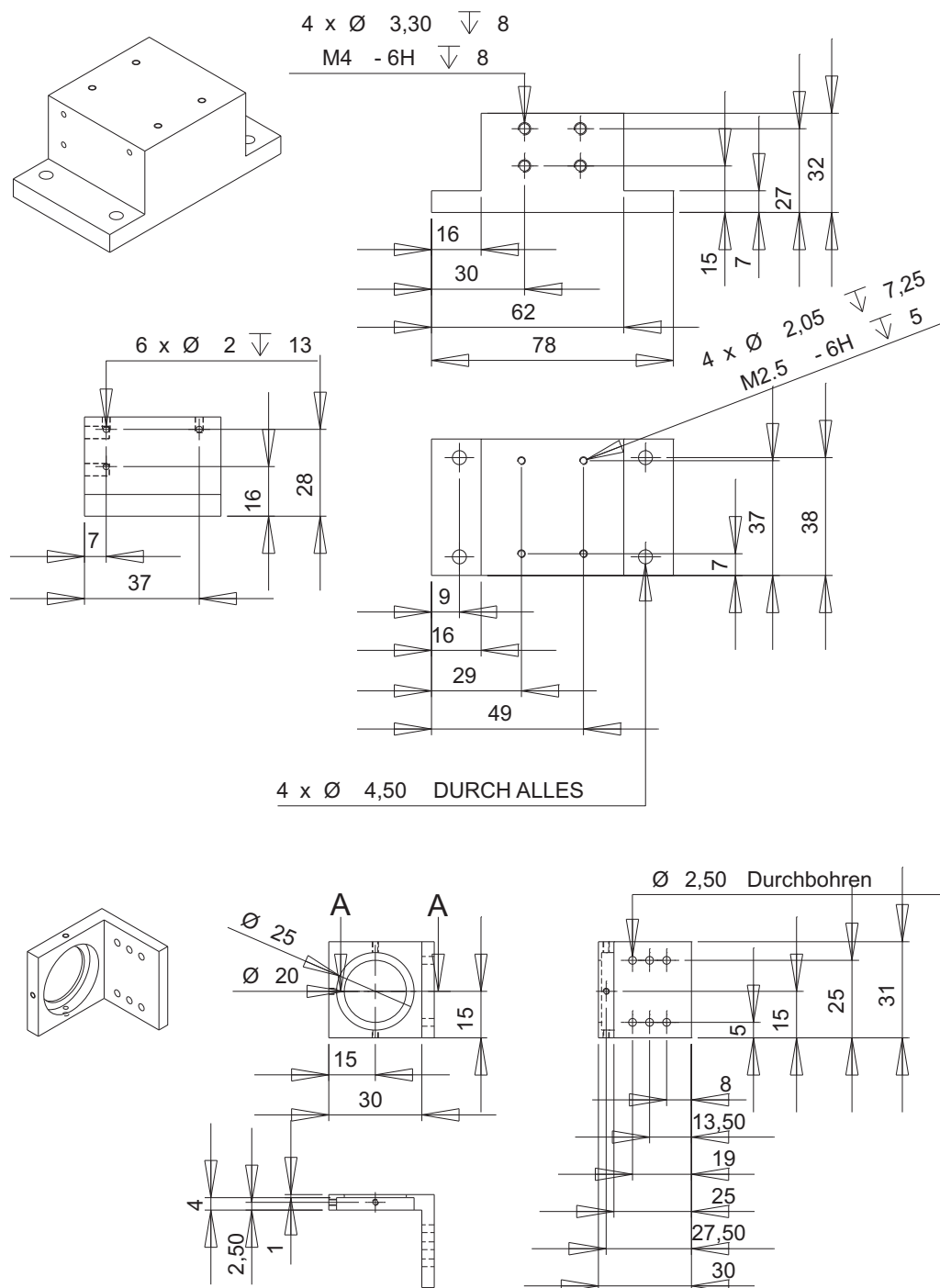


FIGURE C.2: A solid stainless steel block serves as the fundament of the holder (top part). The first insert holder is mounted onto a translation stage and is designed bipartitely.

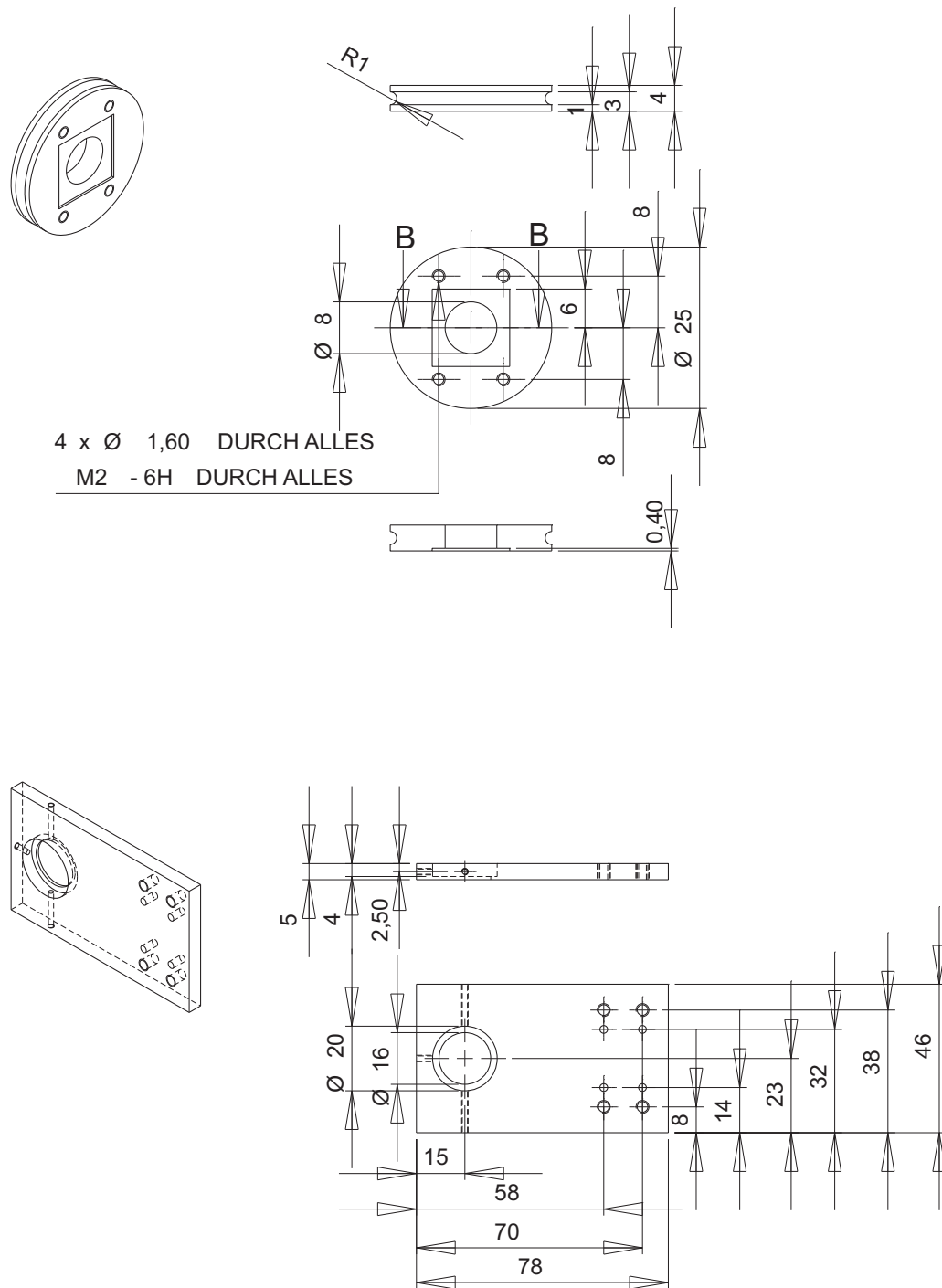


FIGURE C.3: The grating fixed into the frame of its support by stainless steel springs. This provides fixation but allows expansion due to thermal expansion during the bake-out procedure. The groove provides stable and precise rotation of the grating in respect to the insert holder. The holder of the second insert allows independent alignment of pitch, yaw and roll, since it is directly attached to the stainless steel block.

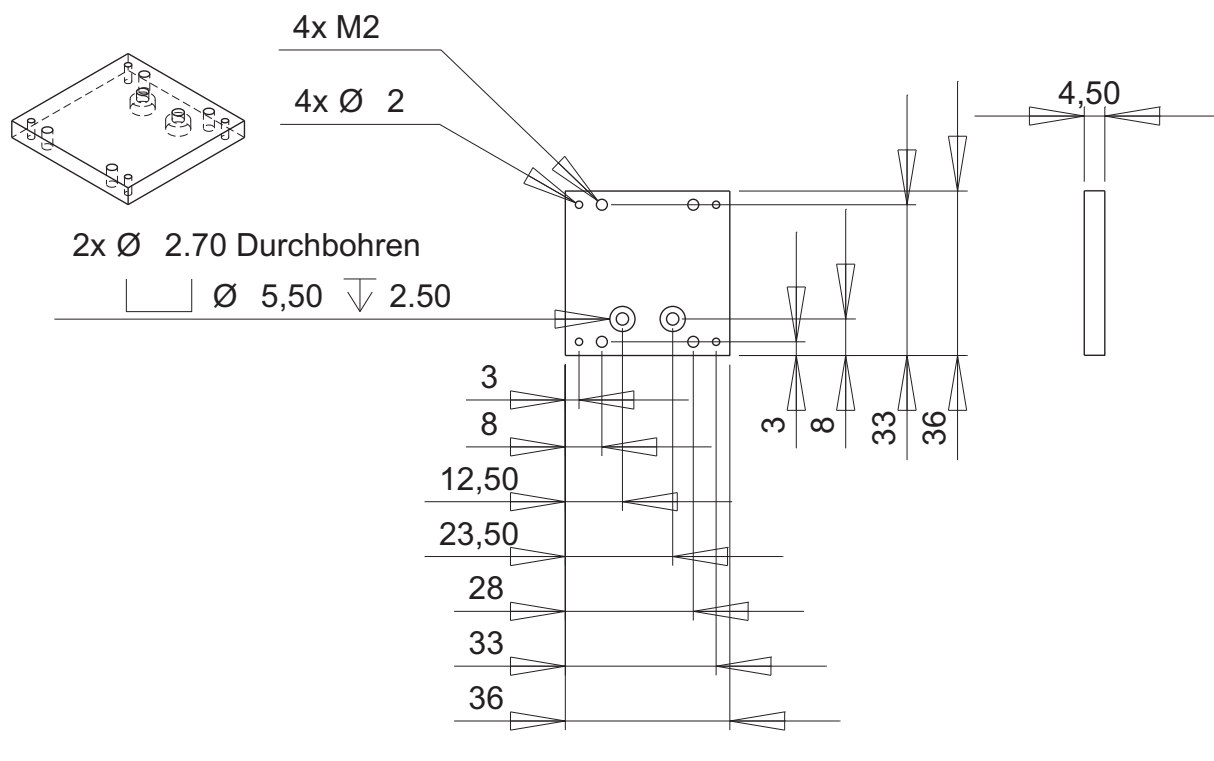


FIGURE C.4: The linear positioner which carries the diffracton grating, is mounted onto this adapter plate. Screws allow precise alignment of the grating pitch and yaw.

# *Acknowledgements*

Team work and the exchange with many excellent colleagues makes experimental physics to such a vivid and dynamic field. Without collaboration and a scientific debate there would not be any progress.

Hence, I sincerely thank Markus Arndt for giving me the opportunity to work in such a professional and amicable atmosphere. Without his profound knowledge and guiding experience, the realization of this work would have never been possible.

In times of desperation we could always count on the professional advice of Hendrik Ulbricht. Thus, special thanks owes him. His straight forward way of problem solving and experimental expertise, helped us to find a way out of numerous tricky situations.

But without Thomas Juffmann and Philipp Geyer it would not have been possible to spent uncountable hours in the basement, scanning for interference contrast. We complemented each other in every situation and thus have grown to a consummate team.

I would like to express my general gratitude to all my colleagues and friends within the group of Markus Arndt and Anton Zeilinger. To be part of such a dynamic and harmonious scientific community has been an unique experience. Thank you for the great time.

I would like to thank my friends, particularly Arnhilt, for their intellectual stimulation. Finally, I want to thank my family for their encouragement and especially my parents and grandparents for their generous support.

# Bibliography

- [1] Herbert Pietschmann. *Phänomenologie der Naturwissenschaften*. Ibero, 2007.
- [2] Albert Einstein. On a heuristic viewpoint concerning the production and transformation of light. *Annalen der Physik*, 17:132–148, 1905.
- [3] Helge Kragh. Max planck: the reluctant revolutionary. *Physics World*, 12, 2000.
- [4] Louis de Broglie. Ondes et quanta. *Comptes Rendus des Sciences de l'Academie des Sciences*, 117:507–510, 1923.
- [5] Paul Germain. Louis de broglie ou la passion de la vraie physique. *La Vie des Sciences*, 4:580, 1987.
- [6] Erwin Schrödinger. Quantisierung als eigenwertproblem. *Physical Review*, 28:1049–1070, 1926.
- [7] Erwin Schrödinger. Quantisierung als eigenwertproblem i. *Annalen der Physik*, 79:361–376, 1926.
- [8] Erwin Schrödinger. Quantisierung als eigenwertproblem ii. *Annalen der Physik*, 79:489–527, 1926.
- [9] Erwin Schrödinger. Quantisierung als eigenwertproblem iii. *Annalen der Physik*, 80:734–756, 1926.
- [10] Erwin Schrödinger. Quantisierung als eigenwertproblem iv. *Annalen der Physik*, 81:109–139, 1927.
- [11] C.J. Davisson and L.H. Germer. The scattering of electrons by a single crystal of nickel. *Nature*, 119:558 – 560, 1927.

- 
- [12] Thomas Young. Experiments and calculations relative to physical optics. *Philosophical Transactions*, 94:I2–I3, 1804.
- [13] G.I. Taylor. Interference fringes with feeble light. *Proc. Cam. phil.Soc*, 15:114, 1909.
- [14] Claus Jönsson. Elektroneninterferenzen an mehreren künstlich hergestellten feinspalten. *Zeitschrift für Physik*, 161:454, 1961.
- [15] A. Tonomura, J. Endo, T. Matsuda, T. Kawasaki, and H. Ezawa. Demonstration of single-electron buildup of an interference pattern. *Am. J. Phys.*, 57:117–120, 1989.
- [16] A. Zeilinger, R. Gähler, C. G. Shull, W. Treimer, and W. Mampe. Single- and double-slit diffraction of neutrons. *Rev. Mod. Phys.*, 60:1067–1073, 1988.
- [17] Anton Zeilinger. Experiment and the foundations of quantum physics. *Rev.Mod.Phys.*, 71:288–297, 1999.
- [18] O. Carnal and J. Mlynek. Young’s double-slit experiment with atoms: A simple atom interferometer. *Phys. Rev. Lett.*, 66:2689–2692, 1991.
- [19] W. Schllkopf. Nondestructive mass selection of small van der waals clusters. *Science*, 266:1345, 1994.
- [20] M. Arndt, O. Nairz, J. Voss-Andreae, C. Keller, G. Van der Zouw, and A. Zeilinger. Wave-particle duality of c60 molecules. *Nature*, 401:680–682, 1999.
- [21] R. Feynman, R. B. Leighton, and M. L. Sands. *The Feynman Lecture on Physics*. Addison-Wesley, 1963.
- [22] K. Hornberger, J. E. Sipe, and M. Arndt. Theory of decoherence in a matter wave Talbot-Lau interferometer. *Phys. Rev. A*, 70(5):53608, 2004.
- [23] S. Nimmrichter and K. Hornberger. Theory of talbot-lau interference beyond the eikonal approximation. *Phys. Rev. A*, 78:023612, 2008. Eprint arXiv:0804.3006.
- [24] I. Estermann and O. Stern. Beugung von Molekularstrahlen. *Z. Phys.*, 61:95–125, 1930.

- [25] H. von Halban and P. Preiswerk. Experimental evidence of neutron diffraction. *C. R. Hebd. Séances Acad.*, 203:73, 1936.
- [26] B. Brezger, L. Hackermüller, S. Uttenthaler, J. Petschinka, M. Arndt, and A. Zeilinger. Matter-wave interferometer for large molecules. *Phys. Rev. Lett.*, 88:100404, 2002.
- [27] H. F. Talbot. Facts relating to optical science. *Philos. Mag.*, 9:401, 1836.
- [28] J. W. S. Rayleigh. On copying diffraction gratings and some phenomneon connected therewith. *Philos. Mag.* 11, 1881.
- [29] Michael S. Chapman, Christopher R. Ekstrom, Troy D. Hammond, Jörg Schmiedmayer, Bridget E. Tannian, Stefan Wehinger, and David E. Pritchard. Near-field imaging of atom diffraction gratings: The atomic Talbot effect. *Phys. Rev. A*, 51:R14, 1995.
- [30] E. Lau. Beugungserscheinungen an doppelrastern. *Ann. Phys.*, 6:417, 1948.
- [31] J. F. Clauser and S. Li. Talbot-von lau atom interferometry with cold slow potassium. *Phys. Rev. A*, 49:R2213, 1994.
- [32] E. Wigner. On the quantum correction for thermodynamic equilibrium. *Phys. Rev.*, 40:749–759, 1932.
- [33] M. Born and P. Jordan. Zur quantenmechanik. *Zeitschrift fr Physik*, 34:858–888, 1925.
- [34] H. A. Kramers W. Heisenberg. On the dispersal of radiation by atoms. *Zeitschrift fr Physik*, 31:681–708, 1925.
- [35] W. P. Schleich. *Quantum Optics in Phase Space*. Wiley-VCH Verlag, Weinheim, 2001.
- [36] B. Brezger, M. Arndt, and A. Zeilinger. Concepts for near-field interferometers with large molecules. *J. Opt. B: Quantum Semiclass. Opt.*, 5:S82–S89, 2003.
- [37] S. Nimmrichter. Matter wave talbot-lau interferometry beyond the eikonal approximation. Master’s thesis, Technische Universität München, Munich, 2007.

- [38] H. B. G. Casimir and D. Polder. The influence of retardation on the London-van der Waals forces. *Phys. Rev.*, 73:360, 1948.
- [39] Stefan Gerlich, Lucia Hackermüller, Klaus Hornberger, Alexander Stibor, Hendrik Ulbricht, Michael Gring, Fabienne Goldfarb, Tim Savas, Marcel Mri, Marcel Mayor, and Markus Arndt. A kapitza-dirac-talbot-lau interferometer for highly polarizable molecules. *Nature Physics*, 3:711 – 715, 2007.
- [40] L. Hackermüller, K. Hornberger, B. Brezger, A. Zeilinger, and M. Arndt. Decoherence in a Talbot Lau interferometer: The influence of molecular scattering. *Appl. Phys. B*, 77:781–787, 2003.
- [41] Karl Jousten, editor. *Handbook of Vacuum Technology*. Wiley-VCH, 2008.
- [42] Thomas Juffmann. Molecular interferometry and nanostructuring. Master’s thesis, University of Vienna, 2008.
- [43] W. Krtzschmer et al. A new form of carbon. *Nature*, 347:354–358, 1990.
- [44] H.W. Kroto, J.R. Heath, S.C. OBrian, R.F. Curl, and R.E. Smalley. C60: Buckminsterfullerene. *Nature*, 318:162–166, 1985.
- [45] M. S. Baba T. S. L. Narasimhan R. Balasubramanina N. Sivaraman C. K. Mathews. Studies on the thermodynamics of the c-60-c70 binary system. *Journal of Physical Chemistry*, 98:1333–1340, 1994.
- [46] P.G. Wahlbeck. The failure of isotropy of a gas in an effusion cell and the transition region. *Journal of Chem. Phys.*, 55, No. 4:1709–1715, 1971.
- [47] V. Piacente, G. Gigli, P. Scardala, A. Giustini, and D. Ferro. Vapor pressure of c-60 buckminsterfullerene. *J. Phys. Chem.*, 99:14052 – 14057, 1995.
- [48] et al. K. D. Carlson. Molecular and hydrodynamical effusion of mercury vapor from knudsen cells. *J. Chem. Phys.*, 38:2725, 1963.
- [49] G. Scoles. *Atomic and molecular beam methods*. Oxford University Press, New York, 1988.

- [50] J. G. Dash and H. S. Sommers. A high transmission slow neutron velocity selector. *Review of Scientific Instruments*, 24:91–96, 1953.
- [51] Olaf Nairz, Markus Arndt, and Anton Zeilinger. Quantum interference experiments with large molecules. *Am. J. Phys.*, 71:319, 2003.
- [52] Hans U. Hostettler and Richard B. Bernstein. Improved slotted disk type velocity selector for molecular beams. *The Review of Scientific Instruments*, 31:872–877, 1960.
- [53] T. A. Savas, S. N. Shah, M. L. Schattenburg, J. M. Carter, and H. I. Smith. Achromatic interferometric lithography for 100-nm-period gratings and grids. *J. Vac. Sci. Technol.*, B 13:2732–2735, 1995.
- [54] A. Stibor, K. Hornberger, L. Hackermüller, A. Zeilinger, and M. Arndt. Talbot-lau interferometry with fullerenes: Sensitivity to inertial forces and vibrational dephasing. *Laser Physics*, 15:10–17, 2005.
- [55] K. Hornberger, S. Gerlich, H. Ulbricht, and Markus Arndt. Theory and experimental verification of kapitza-dirac-talbot-lau-interferometry. *New Journal of Physics*, 11, 2009.
- [56] E.W. Schlag, J. Grotemeyer, and R.D. Levine. Do large molecules ionize? *Chem. Phys. Lett.*, 190:521–527, 1992.
- [57] G Binnig, H. Rohrer, Ch. Gerber, and E. Weibel. 7x 7 reconstruction on si(111) resolved in real space. *Phys. Rev. Lett.*, 50:120–126, 1983.
- [58] G Binnig and H Rohrer. Scanning Tunneling Microscopy. *Helvetica Physica Acta*, 55(6):726–735, 1982. ISSN 0018-0238.
- [59] K. Takayanagi, Y. Tanishiro, S. Takahashi, and M. Takahashi. Structure analysis of si(111) 7x7 reconstructed surface by transmission electron diffraction. *Surf. Science*, 164:367, 1985.
- [60] Y.Z. Li, M. Chander, J.C. Patrin, J.H. Weaver, L.P.F. Chibante, and R.E. Smalley. Adsorption of individual c-60 molecules on si(111). *Phy. Rev. B*, 45:13837–13840, 1992.

- [61] Dong Chen and Dror Sarid. Temperature effects of adsorption of c-60 molecules on si (111) – (7x7) surfaces. *Phys. Rev. B*, 49(11):7612–7619, Mar 1994. doi: 10.1103/PhysRevB.49.7612.
- [62] D. Chen and D. Sarid. Growth of c-60 films on silicon surfaces. *Surf. Sci.*, 74:318, 1994.
- [63] Y.Z. Li, M. Chander, J.C. Patrin, J.H. Weaver, L.P.F. Chibante, and R.E. Smalley. Ordered overlayers of c60 on gaas(110) studied with scanning tunneling microscopy. *Science*, 252:547, 1991.
- [64] J. E. Lilienfeld. The x-rays of the cathode with auto electronic discharge. *Physikalische Zeitschrift*, 23:506–511, 1922.
- [65] L. Nordheim R. H. Fowler. Electron emission in intense electric fields. *Proc. of the royal society of london*, 119:173–181, 1928.
- [66] S. Oguchi R. Kaneko. Ion implanted diamond tip for a scanning tunneling microscope. *Jpn. J. Appl. Phys.*, 28:1854–1855, 1990.
- [67] M. Greiner and P. Kruse. Recrystallization of tungsten wire for fabrication of sharp and stable nanoprobe and field-emitter tips. *Review of Scientific Instrument*, 78, 2007.
- [68] D. K. Biegelsen, F.A. Ponce, and J. C. Tramontana. Ion milled tips for scanning tunneling microscopy. *Appl. Phys. Lett.*, 50:696, 1987.
- [69] A. S. Lucier. Master’s thesis, McGill University, 2004.
- [70] A. Schirmeisen, G. Cross, A. Stalder, P. Grütter, and U. Drig. Metallic adhesion forces and tunneling between atomically defined tip and sample. *Appl. Surf. Sci.*, 157:274, 2000.
- [71] P. Hoffrogge, H. Kopf, and R. Reichelt. Nanostructuring of tips for scanning probe microscopy by ion sputtering: Control of the apex ratio and the tip radius. *J. Appl. Phys.*, 90:5322, 2001.

- [72] H. W. Fink. Mono atomic tips for scanning tunneling microscopy. *IBM J. Res. Dev.*, 30:460, 1986.
- [73] G. D. Rieck. Growth and preferred orientations of crystals in tungsten wires. *Acta Metallurgica*, 6:360, 1958.
- [74] Roland Wiesendanger. *Scanning Probe Microscopy and Spectroscopy*. Cambridge University Press, 1994.
- [75] J. E. Demuth R. J. Hamers, R. M. Tromp. Surface electronic structure of si(111)-7x7 resolved in real space. *Phys.Rev. Lett.*, 56:18, 1986.
- [76] M. A. McCord and R. F. W. Pease. Scanning tunneling microscope as a micromechanical tool. *Appl. Phys. Lett.*, 50:569, 1987.
- [77] E. J. van Loenen, D. Dijkkamp, A. J. Hoeven, J. M. Lenssinck, and J. Dieleman. Direct writing in si with a scanning tunneling microscope. *Appl. Phys. Lett.*, 55:1312, 1989.
- [78] E. J. van Loenen, D. Dijkkamp, A. J. Hoeven, J. M. Lenssinck, and J. Dieleman. Nanometer scale structuring of silicon by direct indentation. *J. Vac. Sci. Techn. A*, 8:574, 1990.
- [79] T. A. Jung, A. Moser, H. J. Hug, D. Brodbeck, R. Hofer, H. R. Hidber, and U. D. Schwarz. The atomic force microscope used as a powerful tool for machining surfaces. *Ultramicroscopy*, 42-44:1446, 1992.
- [80] D. M. Eigler and E. K. Schweizer. Positioning single atoms with a scanning tunneling microscope. *Nature*, 344:254, 1990.
- [81] K. Inananga S. Maruno and T. Isu. Nanoscale manipulation of c<sub>60</sub> with a scanning tunneling microscope. *Microelectronic Engineering*, 39-42, 1995.
- [82] T. Kingetsu K. Nishikawa, M. Yamamoto. Step distribution in the si(111) surface and its effect on microstructure of mbe-grown single- and multi-layered films. *Appl. Surf. Sci.*, 130-132:1998, 1998.

- 
- [83] T. Sakurai, X. D. Wang, Q. K. Xue, Y. Hasegawa, T. Hashiura, and H. Shinohara. Scanning tunneling microscopy study of fullerenes. *Progress in Surface Science*, 51: 263–408, 1996.
- [84] B. Li, H. Wang, J. Yang, and J.G. Hou. High-resolution scanning tunneling microscopy for molecules. *Ultramicroscopy*, 98:317–334, 2004.
- [85] J. G. Hou, Yang Jinlong, Wang Haiqian, Li Qunxiang, Zeng Changgan, Lin Hai, Bing Wang, D. M. Chen, and Zhu Qingshi. Identifying molecular orientation of individual c60 on a si 111- 7 x 7 surface. *Phys. Rev. Lett.*, 83:3001, 1999.
- [86] J. I. Pascual, J. Gomez-Herrero, C. Rogero, and A. M. Baro. Seeing molecular orbitals. *Chemical physics letters*, 321:78–82, 2000.
- [87] D. Klyachko D.M. Chen. Cluster shapes in stm images of isolate clusters and cluster materials. *Surface Science*, 446:98–102, 2000.

# *Curriculum Vitae*

## **Personal Data**

Name	Stefan Truppe
Birth	8 March 1985 in Bregenz
Nationality	Austria

## **Education**

2007	Research activities in the QNP group of Markus Anrdt, working on Laser Desorption of macromolecules
2006	Studies at the University of Oulu, Finland, as ERASMUS participant
2003-2009	Studies of Physics at the University of Vienna
1995-2003	Grammar school in Bregenz, Austria